

NUMERICAL SOLUTION OF THE COMPRESSIBLE LAMINAR, TRANSITIONAL,
AND TURBULENT BOUNDARY LAYER EQUATIONS WITH
COMPARISONS TO EXPERIMENTAL DATA

By

Julius Elmore Harris

B. of Aerospace Engineering

M.S. in Aerospace Engineering

Thesis submitted to the Graduate Faculty of the
Virginia Polytechnic Institute
in candidacy for the degree of

DOCTOR OF PHILOSOPHY

in

Aerospace Engineering

May 1970

N7030323	
(ACCESSION NUMBER)	(THRU)
192	1
(PAGES)	(CODE)
JMX-62963 12	
(NASA CR OR TXN OR AD NUMBER)	

FACILITY FORM 602

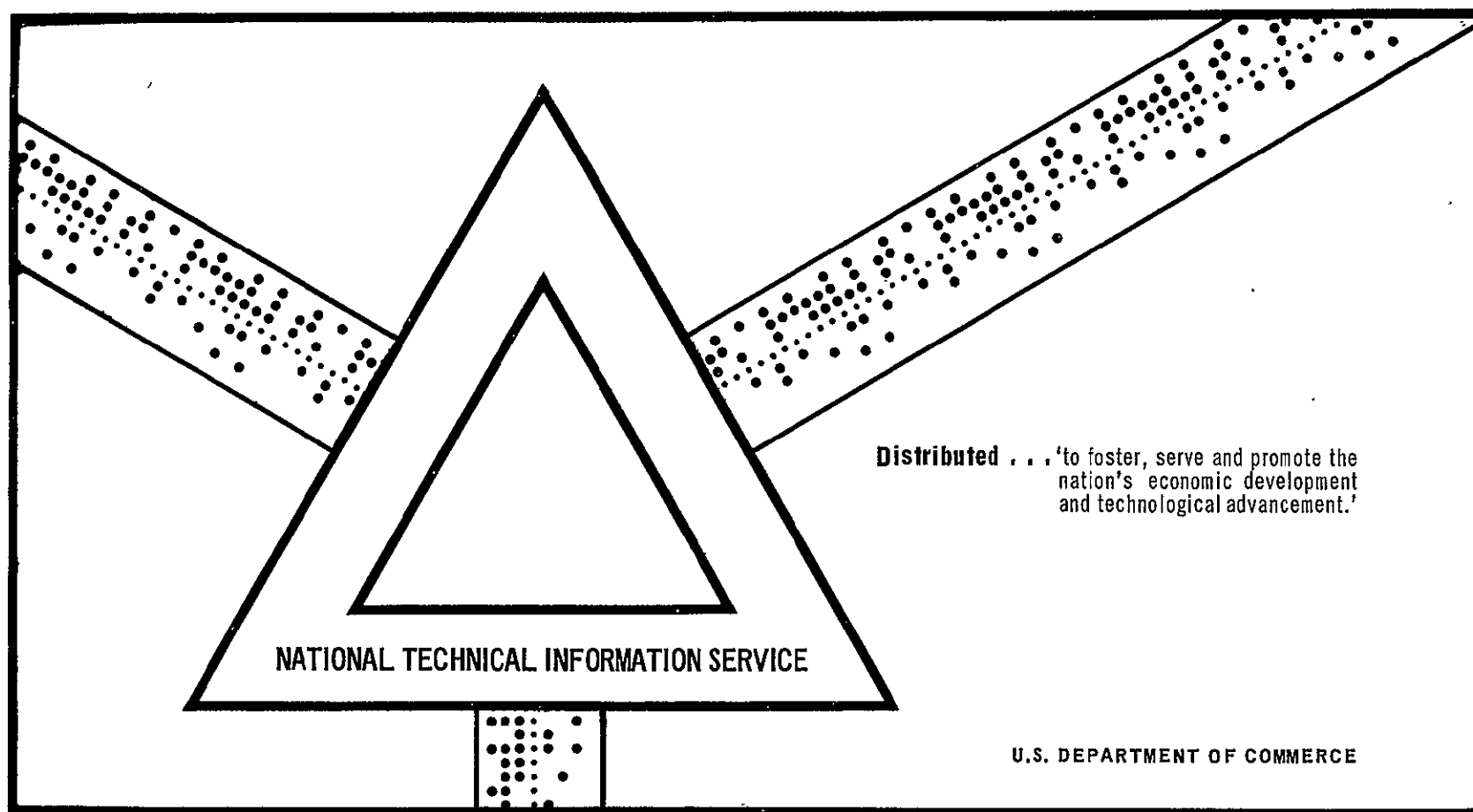
Reproduced by
NATIONAL TECHNICAL
INFORMATION SERVICE
Springfield, Va. 22151

NUMERICAL SOLUTION OF THE COMPRESSIBLE LAMINAR, TRANSITIONAL
AND TURBULENT BOUNDARY LAYER EQUATIONS WITH COMPARISONS TO
EXPERIMENTAL DATA

Julius Elmore Harris

Virginia Polytechnic Institute
Blacksburg, Virginia

May 1970



NUMERICAL SOLUTION OF THE COMPRESSIBLE LAMINAR, TRANSITIONAL,
AND TURBULENT BOUNDARY LAYER EQUATIONS WITH
COMPARISONS TO EXPERIMENTAL DATA

by

Julius Elmore Harris

Thesis submitted to the Graduate Faculty of the
Virginia Polytechnic Institute
in partial fulfillment of the requirements for the degree of

DOCTOR OF PHILOSOPHY

in

Aerospace Engineering

APPROVED:

Fred R. DeJarnette

Dr. Fred R. DeJarnette

R. Thomas Davis

Dr. R. Thomas Davis

C. B. Ling

Dr. Chih B. Ling

Joseph A. Schetz

Dr. Joseph A. Schetz

Clark H. Lewis

Dr. Clark H. Lewis

May 1970

Blacksburg, Virginia

NUMERICAL SOLUTION OF THE COMPRESSIBLE LAMINAR, TRANSITIONAL,
AND TURBULENT BOUNDARY LAYER EQUATIONS WITH
COMPARISONS TO EXPERIMENTAL DATA

By

Julius Elmore Harris

ABSTRACT

A system of equations describing the laminar, transitional, and turbulent compressible boundary layers for either planar or axisymmetric flows together with a numerical method by which the system can be accurately solved is presented. Stability theory and its relation to transition is discussed, and methods are presented with which reasonable estimates may be made of the location of transition and the extent of the transitional flow region. These methods are used in the numerical procedure to connect the three separate boundary layer regimes into one continuous region described by one system of governing equations. The transitional boundary layer structure is developed from a consideration of the statistical production of turbulent spots. The fully developed turbulent region is treated by replacing the Reynolds stress terms with an eddy viscosity model. A specifiable turbulent Prandtl number is used to relate the turbulent flux of heat to the eddy viscosity.

The numerical method used to solve the system of equations is a three-point implicit finite-difference scheme for variable grid-point spacing in both spatial coordinates. The method is self starting; that is, it requires no experimental data input, and is highly efficient with

regards to flexibility, computer processing time, and accuracy. The method is inherently stable; no constraint is placed on the system by a grid-point spacing stability parameter. To the author's knowledge this represents the first time this particular numerical procedure has been applied to transitional and fully turbulent boundary layer flows as well as the first time the transitional flow structure has been included in such a procedure.

Numerous test cases are presented and the results are compared with experimental data for supersonic and hypersonic flows. These test cases include flows with both favorable and adverse pressure gradient histories, mass flux at the wall, and transverse curvature. The results clearly indicate that the system of equations and the numerical procedure by which they are solved can be used to accurately predict the characteristics of laminar, transitional, and turbulent compressible boundary-layer flows.

NUMERICAL SOLUTION OF THE COMPRESSIBLE LAMINAR, TRANSITIONAL,
AND TURBULENT BOUNDARY LAYER EQUATIONS WITH
COMPARISONS TO EXPERIMENTAL DATA

By

Julius Elmore Harris

B. of Aerospace Engineering

M.S. in Aerospace Engineering

Thesis submitted to the Graduate Faculty of the
Virginia Polytechnic Institute
in candidacy for the degree of

DOCTOR OF PHILOSOPHY

in

Aerospace Engineering

May 1970

Blacksburg, Virginia

II. TABLE OF CONTENTS

CHAPTER	PAGE
I. TITLE	i
II. TABLE OF CONTENTS	ii
III. ACKNOWLEDGMENTS	v
IV. LIST OF FIGURES	vi
V. LIST OF SYMBOLS	x
VI. INTRODUCTION	1
VII. MATHEMATICAL DESCRIPTION OF THE EQUATIONS FOR THE LAMINAR, TRANSITIONAL, AND TURBULENT COMPRESSIBLE BOUNDARY LAYER	6
7.1 The System of Partial Differential Equations	6
7.1.1 Geometry and Notation	6
7.1.2 Differential Equations	7
7.1.3 Boundary Conditions	14
7.2 The System of Non-Dimensional Equations	15
7.2.1 Non-Dimensional Variables	15
7.2.2 Non-Dimensional Governing Equations	16
7.2.3 The Stretched Coordinate System	17
7.3 The System of Transformed Equations	19
7.4 Eddy Viscosity and Eddy Conductivity Models	23
7.4.1 Physical Plane	23
7.4.2 Transformed Plane	34
7.5 The Transition Region	35

CHAPTER	PAGE
7.5.1 Stability and Transition	36
7.5.2 Transition Location	40
7.5.2.1 Stability Index	42
7.5.2.2 Empirical Correlations	46
7.5.2.3 Experimental Transition	47
7.5.3 Transitional Flow Structure	49
7.5.4 Transition Extent	52
7.6 Boundary Layer Parameters	55
7.6.1 Displacement Thickness	55
7.6.2 Momentum Thickness	56
7.6.3 Shear Stress	57
7.6.4 Skin Friction Coefficient	58
7.6.5 Heat Transfer	59
7.6.6 Heat Transfer Coefficient	59
7.6.7 Stanton Number	61
7.6.8 Friction Velocity	61
7.6.9 Law of Wall Coordinates	61
7.6.10 Defect Law Coordinates	62
7.7 Pitot Pressure Profiles	62
7.8 Exterior Flow	64
7.9 Variable Entropy	67
VIII. NUMERICAL SOLUTION OF THE GOVERNING EQUATIONS	70
8.1 The Implicit Solution Technique	72
8.1.1 Finite-Difference Mesh Model	72
8.1.2 Finite-Difference Relations	77

CHAPTER	PAGE
8.1.3 Solution of Difference Equations	84
8.1.4 Solution of Continuity Equation	85
8.1.5 Initial Profiles	86
8.1.6 Evaluation of Wall Derivatives	87
8.1.7 Eddy Viscosity Distribution	89
8.1.8 Convergence and Stability	92
8.1.9 Viscous Sublayer	93
8.2 Digital Computer Program	95
IX. EXAMPLE SOLUTIONS FOR THE SYSTEM OF EQUATIONS	99
9.1 High Reynolds Number Turbulent Flow	99
9.2 Tripped Turbulent Boundary Layers	107
9.3 Laminar Flow With Mass Injection	112
9.4 Blunt Body Flow	119
9.5 Highly Nonsimilar Flow With Transverse Curvature	120
9.6 Adverse Pressure Gradient Turbulent Flow	129
9.7 Flow Over Sharp Tipped Cones	133
9.8 Flow Over Planar Surfaces	139
X. DISCUSSION AND CONCLUSIONS	150
XI. REFERENCES	154
XII. VITA	164
XIII. APPENDIX	165

III. ACKNOWLEDGMENTS

The author would like to express his appreciation to the following people at the Langley Research Center, NASA:

1. Mr. Ivan E. Beckwith for his continued assistance through all phases of this thesis.

2. Mr. Joseph M. Price for assistance during the development of the digital computer program.

3. Miss Virginia B. Salley for preparing the final thesis figures.

The author would like to express his sincere appreciation to the following people at the Virginia Polytechnic Institute:

1. Dr. Fred R. DeJarnette, of the Aerospace Engineering Department, for serving as his committee chairman and for his active interest during the course of this thesis.

2. Dr. R. T. Davis, of the Engineering Mechanics Department, whose classroom lectures on viscous flow, assistance, and continuing encouragement has played the major part in the initial formulation and eventual solution of the problem presented in this thesis.

IV. LIST OF FIGURES

FIGURE		PAGE
1.	Coordinate system and notation	8
2.	Boundary conditions in the physical plane	14
3.	Boundary conditions in the stretched plane	18
4.	Two-layer turbulent boundary-layer model	23
5.	Matching procedure for two-layer model	32
6.	Vorticity Reynolds number	44
7.	Transition extent definition	54
8.	Cases where variable grid-point spacing is required . .	74
9.	Finite difference grid model	76
10.	High Reynolds number turbulent flow	103
	(a) Comparisons to skin friction coefficient data . . .	103
	(b) Comparison to velocity profile data	103
	(c) Transition region velocity profiles	104
	(d) Transition region temperature profiles	104
	(e) Transition region total pressure profiles	105
	(f) Transition region Mach number profiles	105
	(g) Intermittency distribution in transition region . .	106
	(h) Boundary-layer thickness in transition region . . .	106
11.	Comparisons with experimental data for tripped	
	turbulent boundary layers	109
	(a) Velocity profile and skin friction coefficient	
	for $M_\infty = 1.982$	109

FIGURE	PAGE
(b) Mach number profile for $M_{\infty} = 1.982$	109
(c) Velocity profile and skin friction coefficient for $M_{\infty} = 3.701$	110
(d) Mach number profile for $M_{\infty} = 3.701$	110
(e) Mach number profile and skin friction coefficient for $M_{\infty} = 4.554$	111
(f) Mach number profile for $M_{\infty} = 4.554$	111
12. Hypersonic laminar boundary layer flow with mass injection	113
(a) Comparisons to heat transfer data	113
(b) Velocity profiles	114
(c) Mach number profiles	115
(d) Vorticity Reynolds number distribution for zero mass injection	116
(e) Vorticity Reynolds number distribution for variable mass injection	118
13. Hypersonic blunt body flow	120
14. Comparisons with data for highly nonsimilar supersonic flow with transverse curvature effects	121
(a) Geometry of configuration	121
(b) Experimental edge Mach number distribution	123
(c) Momentum thickness for $M_{\infty} = 1.398$	125
(d) Momentum thickness for $M_{\infty} = 1.7$	126
(e) Skin friction coefficient for $M_{\infty} = 1.398$	127
(f) Skin friction coefficient for $M_{\infty} = 1.7$	128

FIGURE	PAGE
15. Comparisons to experimental data for adverse pressure gradient supersonic turbulent flow	130
(a) Experimental Mach number distribution	130
(b) Comparisons to experimental momentum thickness and form factor distributions	132
16. Comparisons with experimental Stanton number distributions for hypersonic flow over sharp-tipped cones	135
(a) $M_\infty = 7$, $R_e^* = 3.00 \times 10^6$	135
(b) $M_\infty = 7$, $R_e^* = 3.94 \times 10^6$	135
(c) $M_\infty = 7$, $R_e^* = 5.30 \times 10^6$	136
(d) $M_\infty = 7$, $R_e^* = 6.69 \times 10^6$	136
(e) $M_\infty = 7$, $R_e^* = 7.48 \times 10^6$	137
(f) $M_\infty = 7$, $R_e^* = 9.18 \times 10^6$	137
(g) $M_\infty = 8$, $R_e^* = 12.50 \times 10^6$	138
(h) $M_\infty = 8$, $R_e^* = 17.20 \times 10^6$	138
17. Comparisons with velocity profile data and momentum thickness for laminar, transitional, and turbulent flow over a hollow cylinder at $M_\infty = 2.41$	141
(a) $R_e^* = 0.672 \times 10^6$	141
(b) $R_e^* = 2.88 \times 10^6$	141
(c) $R_e^* = 5.76 \times 10^6$	142
(d) $R_e^* = 8.64 \times 10^6$	142
(e) $R_e^* = 11.50 \times 10^6$	143
(f) Momentum thickness	143

FIGURE	PAGE
18. Comparison with experimental data for laminar and transitional flat plate flow at $M_0 = 7.8$	144
19. Stability index as function of unit Reynolds number . . .	147

V. LIST OF SYMBOLS

a	power law constant, equation (8.41)
$A1_n, B1_n, C1_n, D1_n,$ $E1_n, F1_n, G1_n$	coefficients in the difference equation (8.29) and defined by equations (A-3) to (A-9)
$A2_n, B2_n, C2_n, D2_n,$ $E2_n, F2_n, G2_n$	coefficients in the difference equation (8.30) and defined by equations (A-10) to (A-16)
C_{fe}	skin friction coefficient at wall, $\tau_w^*/(\frac{1}{2} \rho_e^* u_e^{*2})$
C_{f_∞}	skin friction coefficient at wall, $\tau_w^*/(\frac{1}{2} \rho_\infty^* u_\infty^{*2})$
\bar{C}_{fe}	total skin friction coefficient, equation (7.98)
Ch_e	Stanton number defined in equation (7.112)
C_p	specific heat at constant pressure
C_{pmax}	maximum pressure coefficient defined in equation (8.40)
C_{ml}, C'_{ml}	defined in equations (A-45) and (A-46)
$\bar{E}_{ml}, \hat{E}_{ml}$	defined in equations (A-36) and (A-37)
\hat{E}_Y	defined in equation (A-39)
F	velocity ratio, u/u_e
F_{ml}	defined in equation (A-29)
F_{m2}	defined in equation (A-32)
F_Y	defined in equation (A-40)
G	a typical quantity in the boundary layer
h	heat transfer coefficient, equation (7.110)
H	a typical quantity in the boundary layer

$H_1, H_2, H_3, \dots, H_{11}, H_{12}$	coefficients defined by equations (A-17) to (A-28)
i	index used in grid-point notation, equation (8.1)
I	constant used in correlation equation (7.79)
j	flow index; $j = 0$ planar flow, $j = 1$ axisymmetric flow
J	constant used in correlation equation (7.79)
K	grid-point spacing parameter, equation (8.1)
K_1	constant in eddy viscosity model, equation (7.52)
K_2	constant in eddy viscosity model, equation (7.65)
K_λ	thermal conductivity
K_T	eddy conductivity, equation (7.9)
l	defined in equation (7.41)
\bar{l}	mixing length, equation (7.52)
L_{ml}, L_{ml}^*	defined in equations (A-34) and (A-35)
L	reference length, equation (7.20(b))
m	grid-point spacing index (fig. 9)
M	Mach number
n	index defined in figure 9
N	total number of grid points (fig. 9)
p	pressure
q	heat transfer rate, equation (7.103)
Q	convergence parameter, equation (7.138)
r	radial coordinate
r_b	base radius, equation (8.41)

r_f	recovery factor, equation (7.111)
r_o	body radius
r_s	shock wave coordinate
R_e^*	unit Reynolds number, u^*/ν^* , (feet) ⁻¹
R_{ref}	reference Reynolds number, equation (7.24)
Re_x	Reynolds number based on x^* , $\frac{u_e^*}{\nu_e^*} x^*$
$Re_{x_{t,i}}$	Reynolds number at transition, $\frac{u_e^*}{\nu_e^*} x_{t,i}^*$
$Re_{\delta^*,t}$	transition Reynolds number based on displacement thickness, $\frac{u_e^*}{\nu_e^*} \delta_t^*$
$Re_{\Delta x_t}$	Reynolds number based on transition extent, $\frac{u_e^*}{\nu_e^*} (x_{t,f}^* - x_{t,i}^*)$
Re_θ	Reynolds number based on momentum thickness, $(u_e^*/\nu_e^*)\theta$
S^*	Sutherland viscosity constant (198.6° R)
t	transverse curvature term, equation (7.34)
T	static temperature
T_{aw}	adiabatic wall temperature, equation (7.108)
T_{m1}, T_{m2}	defined in equations (A-30) and (A-33)
T_Y	defined in equation (A-41)
u	velocity component in x-direction
\tilde{u}	defect law coordinate, equation (7.118)
u^+	law of wall coordinate, equation (7.116b)
u_τ	friction velocity, equation (7.115)

v	velocity component in y -direction
\tilde{v}	velocity component defined by equation (7.7)
v^+	velocity component defined by equation (7.26)
V	transformed normal velocity component, equation (7.37)
V_{ml}	defined in equation (A-31)
x	boundary layer coordinate tangent to surface
$x_{t,i}$	beginning of transition (fig. 7)
$x_{t,f}$	end of transition (fig. 7)
X_1, X_2, X_3, X_4, X_5	functions of the grid-point spacing defined by equations (8.7) to (8.11)
y	boundary layer coordinate normal to surface
y^+	law of wall coordinate, equation (7.116a)
y_m	defined in figure 5
Y	boundary layer coordinate normal to surface in stretched plane (fig. 3)
$Y_1, Y_2, Y_3, Y_4, Y_5, Y_6$	functions of the grid-point spacing defined by equations (8.15) to (8.20)
z	body coordinate
z_s	shock wave coordinate
α	defined in equation (7.41)
$\bar{\alpha}$	constant defined in equation (7.84)
β	defined in equation (7.41)
$\bar{\beta}$	constant defined in equation (7.84)
γ	ratio of specific heats

$\bar{\gamma}$	transverse intermittency distribution, equation (7.68)
Γ	streamwise intermittency distribution, equation (7.81)
δ	boundary layer thickness
$\delta_{K_{inc}}$	incompressible displacement thickness
δ^*	nondimensional displacement thickness, δ^*/L^*
Δx_t	transition extent, $x_{t,f} - x_{t,i}$
Δx	grid-point spacing in physical plane
$\Delta \xi, \Delta \eta$	grid-point spacing in transformed plane (see fig. 9)
ϵ	eddy viscosity
$\bar{\epsilon}$	eddy viscosity function defined in equation (7.15)
$\bar{\epsilon}_{av}$	defined in equation (8.37)
$\hat{\epsilon}$	eddy viscosity function defined in equation (7.16)
η	transformed normal boundary layer coordinate
$\bar{\theta}$	nondimensional momentum thickness, θ/L^*
Θ	static temperature ratio, equation (7.36)
λ	defined in equation (7.83)
μ	molecular viscosity
ν	kinematic viscosity, μ/ρ
$\bar{\nu}$	average kinematic viscosity, equation (7.55)
ξ	transformed streamwise boundary layer coordinate
$\bar{\xi}$	defined in equation (7.82)
Π, Π_1, Π_2	functions defined in equations (7.72) to (7.74)

ρ	density
σ	Prandtl number, $C_p \mu / K_l$
σ_t	static turbulent Prandtl number, equation (7.10)
τ	shear stress
τ_l	laminar shear stress
τ_t	turbulent shear stress
τ_T	total shear stress, equation (7.93)
ϕ	angle between local tangent to surface and centerline of body (see fig. 1)
χ	stability index, equation (7.78)
χ_{\max}	maximum local value of χ (fig. 6)
$(\chi_{\max})_{cr}$	value of stability index at transition
ψ	streamline (see fig. 1)
ω	stretching parameter defined in equation (7.27)
$\Omega_1, \Omega_2, \Omega_3, \Omega_4, \Omega_5$	functional relations in equations (7.48), (7.50), (7.86), and (9.1)
Subscripts	
e	edge value
i	inner region of turbulent layer
m	mesh point in ξ -direction; see fig. 9, or measured pitot value, equation (7.124)
o	outer region of turbulent layer
n	mesh point in η -direction; see figure 9
ref	reference value; see equations (7.125) to (7.128).

s shock condition

s.l. sublayer

t total condition

w wall value

∞ free stream

Superscripts

* dimensional quantity

' fluctuating component

— time average value

Other Notation

A coordinate used as a subscript means partial differential with respect to the coordinate. See equation (8.4).

TVC transverse curvature

T-S Tollmien-Schlichting

VI. INTRODUCTION

The boundary layer concept first introduced by Prandtl (ref. 1) in 1904 divides the flow field over an arbitrary surface into two distinct regions; an inviscid outer region in which solutions to the Euler equations describe the flow field characteristics, and a viscous inner region where the classical boundary-layer equations are valid. The boundary-layer region may be further divided into three categories; namely, laminar, transitional, and turbulent.

The laminar boundary layer has received considerable attention over the past 60 years, especially over the past decade with the increased availability of high-speed digital computers. Early solutions of the boundary layer equations were obtained for incompressible, zero pressure gradient, adiabatic flows. These solutions were generally obtained by series expansion techniques and were elegant in formulation, but time-consuming to obtain; however, they did yield valuable information for extrapolation to more complex flow systems. The addition of pressure gradients into the problem required the use of numerical techniques which were impractical without high-speed digital computer systems. This difficulty led to the development of momentum integral approaches in which the actual boundary layer equations were not satisfied at each point across the viscous region, but instead were satisfied only in the average. Reviews of these early methods are given in references 2, 3, and 4.

As flight speeds increased, it became necessary to include the effects of compressibility. The inclusion of compressibility coupled the momentum and energy equations and resulted in a formidable system of five equations, three of which (the conservation of mass, momentum, and energy) were nonlinear partial differential equations. The requirement of simultaneous solution of this system prevented any complete numerical solutions from being obtained until the advent of early digital computer systems. There then appeared a number of similar and so-called local similarity solutions. A review of these methods and solutions is presented in reference 5. Finally, in the early part of the past decade the complete nonsimilar laminar equations for the compressible, nonadiabatic boundary layer were solved to a high degree of accuracy by finite difference techniques (see Blottner, ref. 6).

One of the earliest observations made by students of fluid mechanics was that, in general, a turbulent or random-like state of motion was the most natural state of fluid flow. O. Reynolds (ref. 7) in his now classical study of pipe flow observed that at some value of the parameter Ud/ν , where U , d , and ν represent the mean velocity of the flow, the diameter of the pipe, and the kinematic viscosity, respectively, the laminar flow degenerated to a turbulent state in which the molecular viscosity became of secondary importance in relation to the kinematics of the flow. Early investigations of turbulent flow categorically divided nonlaminar flow into two regions; transitional and turbulent.

Transition, and the ability to accurately predict its location on an arbitrary surface has been the object of intensive analytical

and experimental research for many years. A complete understanding of the transition process as well as the ability to predict its location for general flow configurations has not yet been achieved. However, the effects of basic flow parameters on transition have been studied in detail. The flow within the transition region, which is basically nonlinear in character is neither fully laminar nor fully turbulent but a combination of both. The detailed mean flow within the transition region itself has not been studied as extensively as the location of transition and the characteristics of the eventual fully developed turbulent boundary layer. Consequently, little if any effort has been specifically directed towards the problem of developing a suitable system of equations that would describe the mean characteristics of transitional flow. There have been a few experiments in which the mean profiles were measured as well as some where the intermittent character of the flow was studied, but more detailed work is still required. There have, of course, been many experimental tests at high speeds in which the heat transfer at the wall has been measured, but this describes little if anything of the flow structure away from the wall. Săvulescu (ref. 8) has recently presented one of the first thorough reviews of transition phenomena. Morkovin (ref. 9) recently completed the most current and extensive review of modern stability theory and experimental hypersonic transition. The characteristics of transitional boundary layers for low speed incompressible flow as well as compressible flow (ref. 10) has received some attention. These results at least allow workable models of the mean flow structure in the transition region to

be formulated and applied tentatively to compressible flow systems. It appears that at the present time it is not possible to obtain completely general solutions for transitional flow. However, it is possible to develop models for the mean flow from existing data on the intermittency distributions which represents in a broad sense the statistical distribution of turbulence intensities.

Compressible turbulent boundary-layer flows have received much attention over the past decade because of the vital need of being able to accurately predict heat transfer and skin friction for high performance aerospace vehicles. However, most of the work has been experimental with the main objective directed towards developing empirical or semiempirical correlation techniques. Little if any effort was devoted to obtaining numerical solutions of the equations for turbulent boundary layers until a few years ago. The principal difficulties were associated with the modeling of the turbulent transport terms as well as techniques for obtaining solutions on existing digital computer systems. Even today because of the limited understanding of these turbulent transport processes, completely general solutions of the mean turbulent boundary layer equations are not possible. However, by modeling the turbulent transport terms through eddy viscosity or mixing length concepts it is possible to solve the system of equations directly. Reviews of recent analytical advances are contained in references 11 and 12 for incompressible flow and references 13 and 14 for compressible flows.

The purpose for the present thesis is to present a system of equations describing the laminar, transitional, and turbulent compressible

boundary layers and a solution technique with which the system may be accurately solved for either planar or axisymmetric perfect gas flows. The solution technique has been found to yield accurate results for compressible laminar, transitional, and fully developed turbulent boundary layers with pressure gradients, heat transfer, and mass transfer at the wall. The solution technique utilizes 3-point implicit difference relations and the method first developed by Flugge-Lotz and Blottner (ref. 15) and later improved upon by Davis and Flugge-Lotz (ref. 16) to solve the difference equations. The equations are solved in the transformed plane. Transverse curvature terms are retained, and variable entropy effects may be included. The transition region is modeled by utilizing an intermittency distribution which describes the statistical distribution of turbulent spots and modifies the models of the turbulent transport processes. The turbulent region is treated by solving the mean turbulent boundary layer equations in which the Reynolds stress terms are replaced by an eddy viscosity model, and a specifiable turbulent Prandtl number function relates the turbulent flux of heat to the eddy viscosity. The eddy viscosity model is based upon existing experimental data.

VII. MATHEMATICAL DESCRIPTION OF THE EQUATIONS FOR THE LAMINAR,
TRANSITIONAL, AND TURBULENT COMPRESSIBLE
BOUNDARY LAYER

In this chapter the governing equations for the compressible boundary layer together with the required boundary conditions are presented. Special attention is devoted to the eddy viscosity and eddy conductivity models used to represent the apparent turbulent shear and heat flux terms appearing in the mean turbulent boundary-layer equations. Boundary layer stability, transition, and transitional region flow structure are also discussed.

7.1 The System of Partial Differential Equations

7.1.1 Geometry and Notation

The orthogonal coordinate system chosen for the present analysis is presented in figure 1. The boundary layer coordinate system is denoted by x^* and y^* which are tangent to and normal to the surface, respectively. The origin of both the boundary layer coordinate system, (x^*, y^*) and the body coordinate system, (z^*, r_0^*) is located at the stagnation point for blunt body flows as shown in figure 1, or at the leading edge for sharp-tipped cones or planar surfaces. The velocity components u^* and v^* are oriented in the x^* and y^* direction, respectively. Transverse curvature terms are retained because of their importance in the development of boundary-layer flows over slender bodies of revolution where the boundary-layer thickness may become of the order of the body radius, r_0^* . A discussion of transverse curvature and its

effect on the resulting boundary layer characteristics is presented by Lewis (ref. 17). The radial coordinate, r^* represents the true radial distance from the centerline of the body to a given point (x^*, y^*) in the boundary layer. The angle ϕ is the angle between the z^* axis and local tangent evaluated at $(x^*, 0)$. The coordinates $(x_{t,i}^*, 0)$ and $(x_{t,f}^*, 0)$ represent the location at which transition is initiated and completed, respectively.

7.1.2 Differential Equations

The flow of a compressible, viscous, heat conducting fluid is mathematically described by the continuity, Navier-Stokes, and energy equations together with an equation of state, a heat conductivity law, and a viscosity law. For flows at large Reynolds numbers, Prandtl (ref. 1) has shown that the Navier-Stokes and energy equations can be simplified to a form now recognized as the classical boundary layer equations. These equations may be written as follows (see ref. 2):

Continuity

$$\frac{\partial}{\partial x^*} (r^{*j} \rho^* u^*) + \frac{\partial}{\partial y^*} (r^{*j} \rho^* v^*) = 0 \quad (7.1)$$

Momentum

$$\rho^* \left(u^* \frac{\partial u^*}{\partial x^*} + v^* \frac{\partial u^*}{\partial y^*} \right) = - \frac{dP^*}{dx^*} + \frac{1}{r^{*j}} \frac{\partial}{\partial y^*} \left[r^{*j} \left(\mu^* \frac{\partial u^*}{\partial y^*} \right) \right] \quad (7.2)$$

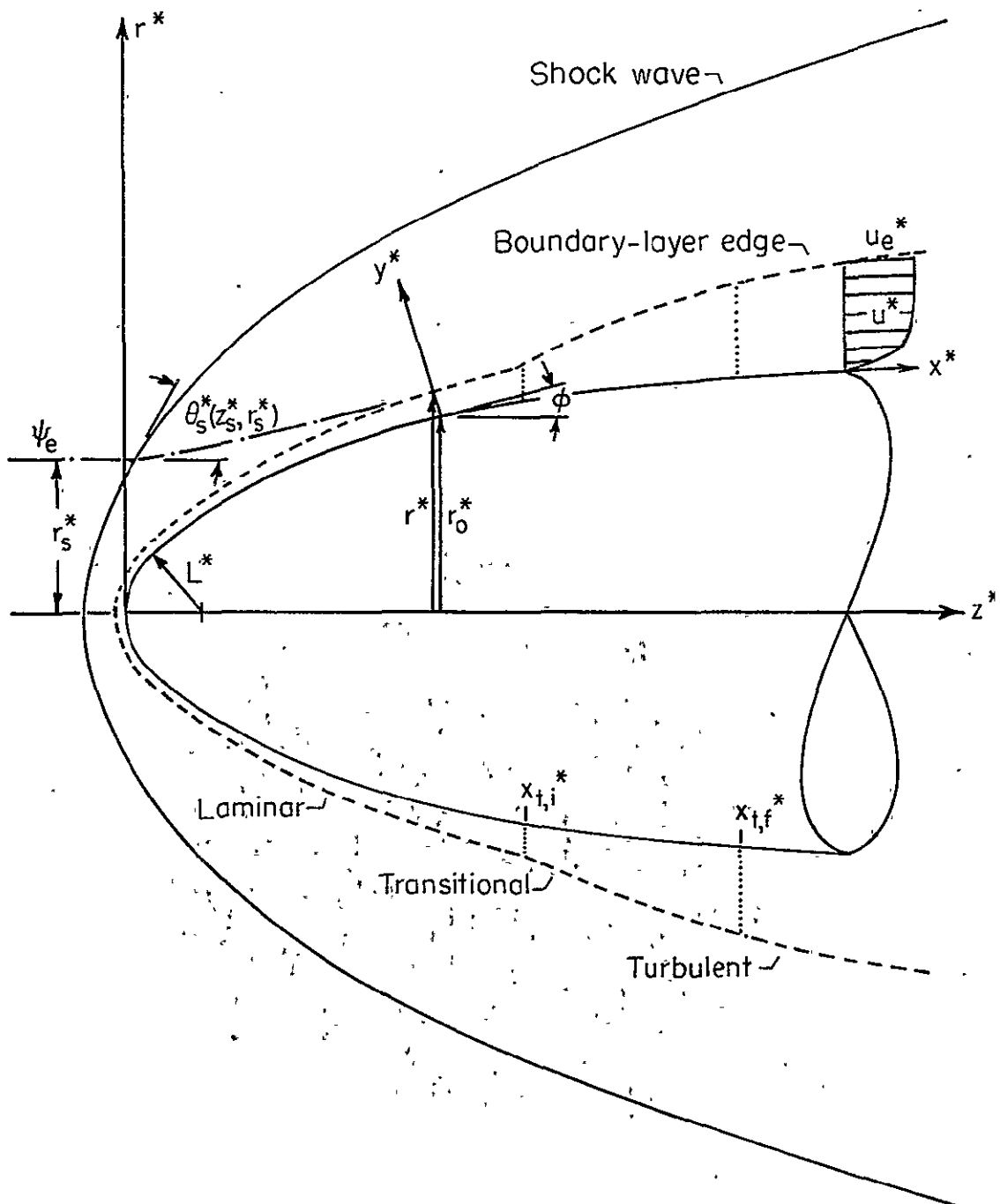


Figure 1.- Coordinate system and notation.

Energy

$$\rho^* \left[u^* \frac{\partial}{\partial x^*} (C_p^* T^*) + v^* \frac{\partial}{\partial y^*} (C_p^* T^*) \right] = u^* \frac{dp^*}{dx^*} + \frac{1}{r^{*j}} \frac{\partial}{\partial y^*} \left[\frac{r^{*j} K_l^*}{C_p^*} \frac{\partial}{\partial y^*} (C_p^* T^*) \right] + \mu^* \left(\frac{\partial u^*}{\partial y^*} \right)^2 \quad (7.3)$$

Osborn Reynolds (ref. 7) in 1883 was the first to observe and study the phenomena of transition from laminar to turbulent flow. In his theoretical studies of turbulence (ref. 18) he assumed that the instantaneous fluid velocity at a point could be separated into a mean and a fluctuating component. The result of his early work was a set of mean turbulent boundary layer equations. This system of equations can be written as follows (see ref. 19):

Continuity

$$\frac{\partial}{\partial x^*} (r^{*j} \rho^* u^*) + \frac{\partial}{\partial y^*} \left[r^{*j} \rho^* \left(v^* + \frac{\overline{\rho^{*j} v^{*j}}}{\rho^*} \right) \right] = 0 \quad (7.4)$$

Momentum

$$\rho^* \left[u^* \frac{\partial u^*}{\partial x^*} + \left(v^* + \frac{\overline{\rho^{*j} v^{*j}}}{\rho^*} \right) \frac{\partial u^*}{\partial y^*} \right] = - \frac{dp^*}{dx^*} + \frac{1}{r^{*j}} \frac{\partial}{\partial y^*} \left[r^{*j} \left(\mu^* \frac{\partial u^*}{\partial y^*} - \rho^* \overline{u^{*j} v^{*j}} \right) \right] \quad (7.5)$$

Energy

$$\begin{aligned}
\rho^* \left[u^* \frac{\partial}{\partial x^*} (C_p^* T^*) + \left(v^* + \frac{\overline{\rho^* v^{*'} }}{\rho^*} \right) \frac{\partial}{\partial y^*} (C_p^* T^*) \right] \\
= u^* \frac{dp^*}{dx^*} + \frac{1}{r^{*j}} \frac{\partial}{\partial y^*} \left[r^{*j} \frac{K_T^*}{C_p^*} \frac{\partial}{\partial y^*} (C_p^* T^*) \right] + \mu^* \left(\frac{\partial u^*}{\partial y^*} \right)^2 \\
+ \frac{1}{r^{*j}} \frac{\partial}{\partial y^*} \left[r^{*j} \left(- C_p^* \overline{\rho^* v^{*'} T^{*'}} \right) \right] - \overline{\rho^* u^{*'} v^{*'}} \frac{\partial u^*}{\partial y^*}
\end{aligned}
\tag{7.6}$$

The mean turbulent equations are identical to those for the laminar boundary layer (eqs. (7.1) to (7.3)) with the exception of the correlations of turbulent fluctuating quantities which are the apparent mass, shear, and heat flux terms caused by the action of turbulence.

The main problem of calculating turbulent flows from this set of equations is concerned with how to relate these turbulent correlations to the mean flow and thereby obtain a closed system of equations. In the present analysis, the apparent mass flux term, $\overline{\rho^* v^{*'}}$, the apparent shear stress term, $\rho^* \overline{u^{*'} v^{*'}}$ (Reynolds stress term) and the apparent heat flux term, $C_p^* \rho^* \overline{v^{*'} T^{*'}}$ are modeled or represented by a new velocity component, \tilde{v}^* , an eddy viscosity ϵ^* , and an eddy conductivity K_T^* , respectively.

A new velocity component normal to the surface is defined as follows:

$$\tilde{v}^* = v^* + \frac{\overline{\rho^* v^{*' }}}{\rho^*}
\tag{7.7}$$

The eddy viscosity is defined as

$$\epsilon^* = - \rho^* \frac{\overline{u^* v^*}}{\partial u^* / \partial y^*} \quad (7.8)$$

and the eddy conductivity as

$$K_T^* = - C_p^* \rho^* \frac{\overline{v^* T^*}}{\partial T^* / \partial y^*} \quad (7.9)$$

The static turbulent Prandtl number is defined as follows:

$$\sigma_t = \frac{\overline{u^* v^*} (\partial T^* / \partial y^*)}{\overline{v^* T^*} (\partial u^* / \partial y^*)} \quad (7.10)$$

Equation (7.10) can then be expressed in terms of equations (7.8) and (7.9) as

$$\sigma_t = \frac{C_p^* \epsilon^*}{K_T^*} \quad (7.11)$$

The eddy viscosity model used in the present analysis is discussed in Section 7.4.

In terms of equations (7.7) through (7.11) the governing differential equations may be written as follows:

Continuity

$$\frac{\partial}{\partial x^*} (r^{*j} \rho^* u^*) + \frac{\partial}{\partial y^*} (r^{*j} \rho^* \tilde{v}^*) = 0 \quad (7.12)$$

Momentum

$$\rho^* \left(u^* \frac{\partial u^*}{\partial x^*} + \tilde{v}^* \frac{\partial u^*}{\partial y^*} \right) = - \frac{dp^*}{dx^*} + \frac{1}{r^{*j}} \frac{\partial}{\partial y^*} \left(r^{*j} \mu^* \bar{\epsilon} \frac{\partial u^*}{\partial y^*} \right) \quad (7.13)$$

Energy

$$\begin{aligned} \rho^* \left[u^* \frac{\partial}{\partial x^*} (C_p^* T^*) + \tilde{v}^* \frac{\partial}{\partial y^*} (C_p^* T^*) \right] &= u^* \frac{dp^*}{dx^*} + \mu^* \bar{\epsilon} \left(\frac{\partial u^*}{\partial y^*} \right)^2 \\ &+ \frac{1}{r^{*j}} \frac{\partial}{\partial y^*} \left[\frac{r^{*j} \mu^*}{\sigma} \hat{\epsilon} \frac{\partial}{\partial y^*} (C_p^* T^*) \right] \end{aligned} \quad (7.14)$$

The terms $\bar{\epsilon}$ and $\hat{\epsilon}$ appearing in equations (7.13) and (7.14) are defined as follows:

$$\bar{\epsilon} = \left(1 + \frac{\epsilon^*}{\mu^*} \Gamma \right) \quad (7.15)$$

and

$$\hat{\epsilon} = \left(1 + \frac{\epsilon^*}{\mu^*} \frac{\sigma}{\sigma_t} \Gamma \right) \quad (7.16)$$

respectively.

The function, Γ , appearing in equations (7.15) and (7.16) represents the streamwise intermittency distribution in the transitional region of the boundary layer. Γ assumes a value of zero in the laminar region of the boundary layer and a value of unity in the fully turbulent boundary layer. The variation of Γ within the transitional region of

the boundary layer depends upon the statistical growth and distribution of turbulent spots. The intermittency function is discussed in Section 7.5.3.

In order to complete the system of equations the perfect gas law and Sutherlands viscosity relation are introduced.

Gas Law

$$P^* = C_p^* \left(\frac{\gamma - 1}{\gamma} \right) \rho^* T^* \quad (7.17)$$

Viscosity Law

$$\frac{\mu^*}{\mu_{ref}^*} = \left(\frac{T^*}{T_{ref}^*} \right)^{3/2} \left(\frac{1 + S^*/T_{ref}^*}{T^*/T_{ref}^* + S^*/T_{ref}^*} \right) \quad (\text{air only}) \quad (7.18)$$

The system of governing equations then consists of three nonlinear partial differential equations and two algebraic relations. Two of these differential equations (eqs. (7.13) and (7.14)) are second order while the remaining differential equation (7.12) is first order.

Consequently, if suitable relations for ϵ^* , σ_t , and Γ can be specified there are five unknowns; namely, u^* , \tilde{v}^* , ρ^* , T^* , and μ^* and five equations.

The pressure gradient term appearing in equations (7.13) and (7.14) is replaced by the Bernoulli relation; namely

$$\frac{dp^*}{dx^*} = - \rho_e^* u_e^* \frac{du_e^*}{dx^*} \quad (7.19)$$

which is determined from an inviscid solution. If variable entropy is considered (see Section 7.9) dp^*/dx^* is retained in equations (7.13) and (7.14).

7.1.3 Boundary Conditions

In order to obtain a unique solution to the system of governing equations it is necessary to satisfy the particular boundary conditions of the problem under consideration. These conditions are shown schematically in figure 2.

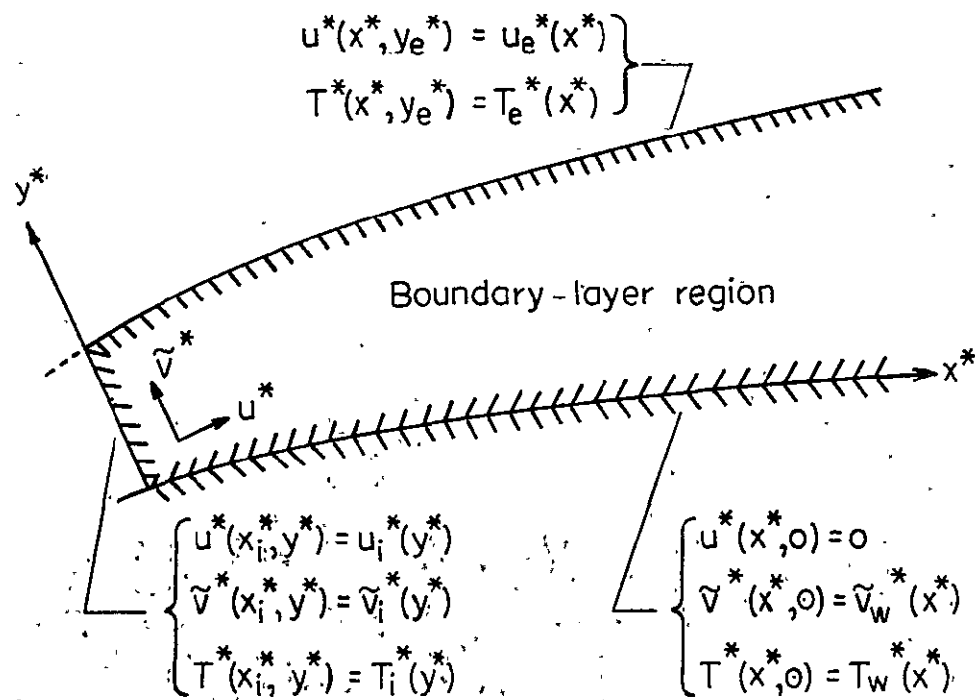


Figure 2.- Boundary conditions in the physical plane.

The velocity and temperature distribution at the edge of the boundary layer are determined from the shape of the body by using inviscid flow theory and are discussed in Section 7.8. The no-slip condition is

imposed at the wall; however, arbitrary distributions of \tilde{v}_w^* and T_w^* may be specified.

The parabolic nature of equations (7.13) and (7.14) requires that the initial velocity and temperature profiles be specified at x_1^* . These initial profiles are obtained in the present investigation from either an exact numerical solution of the similar boundary layer equations or from experimental data and are discussed in Section 8.1.5.

7.2 The System of Non-Dimensional Equations

7.2.1 Non-Dimensional Variables

The non-dimensional variables chosen for the present analysis are defined as follows:

Dependent Variables

$$\left. \begin{aligned} u &= u^*/u_{\text{ref}}^* \\ \tilde{v} &= \tilde{v}^*/u_{\text{ref}}^* \\ P &= P^*/(\rho_{\text{ref}}^* u_{\text{ref}}^{*2}) \\ \rho &= \rho^*/\rho_{\text{ref}}^* \\ T &= T^*/T_{\text{ref}}^* \\ \mu &= \mu^*/\mu_{\text{ref}}^* \end{aligned} \right\} \quad (7.20a)$$

Independent Variables

$$\left. \begin{aligned} x &= x^*/L^* \\ y &= y^*/L^* \\ r &= r^*/L^* \end{aligned} \right\} \quad (7.20b)$$

The reference values of density and velocity used in equations (7.20) are taken to be those of the free stream, the reference temperature is taken to be u_{ref}^{*2}/Cp^* , and the reference viscosity is the value of the molecular viscosity evaluated from the Sutherland law at the reference temperature. The reference length (characteristic length) L^* may be taken as the nose radius, for example, in the case of a spherically blunted body or as any unit length for planar flows. (See equations (7.125) to (7.128).)

7.2.2 Non-Dimensional Governing Equations

The non-dimensional equations are obtained by substituting equations (7.20) into equations (7.12), (7.13), and (7.14) and are as follows:

Continuity

$$\frac{\partial}{\partial x}(r^j \rho u) + \frac{\partial}{\partial y}(r^j \rho \tilde{v}) = 0 \quad (7.21)$$

Momentum

$$\rho \left(u \frac{\partial u}{\partial x} + \tilde{v} \frac{\partial u}{\partial y} \right) = - \frac{dp}{dx} + \frac{1}{R_{ref}} \left[\frac{1}{r^j} \frac{\partial}{\partial y} \left(r^j \mu \tilde{e} \frac{\partial u}{\partial y} \right) \right] \quad (7.22)$$

Energy

$$\rho \left(u \frac{\partial T}{\partial x} + \tilde{v} \frac{\partial T}{\partial y} \right) = u \frac{dp}{dx} + \frac{1}{R_{ref}} \left[\mu \tilde{e} \left(\frac{\partial u}{\partial y} \right)^2 + \frac{1}{r^j} \frac{\partial}{\partial y} \left(r^j \frac{\mu \hat{e}}{\sigma} \frac{\partial T}{\partial y} \right) \right] \quad (7.23)$$

The parameter R_{ref} appearing in equations (7.21), (7.22), and (7.23) is a reference Reynolds number defined as

$$R_{\text{ref}} = \frac{\rho_{\text{ref}}^* u_{\text{ref}}^* L^*}{\mu_{\text{ref}}^*} \quad (7.24)$$

7.2.3 The Stretched Coordinate System

In order to remove the reference Reynolds number from the governing non-dimensional equations, as well as stretch the coordinate normal to the wall a new independent variable, Y , is defined; that is

$$Y = y/\omega \quad (7.25)$$

A new velocity component is also defined by the relation

$$v^+ = \frac{\tilde{v}}{\omega} \quad (7.26)$$

where the parameter ω is defined as follows:

$$\omega = (R_{\text{ref}})^{-1/2} \quad (7.27)$$

The non-dimensional governing equations then become in terms of the stretched variables

Continuity

$$\frac{\partial}{\partial x}(r^j \rho u) + \frac{\partial}{\partial Y}(r^j \rho v^+) = 0 \quad (7.28)$$

Momentum

$$\rho \left(u \frac{\partial u}{\partial x} + v^+ \frac{\partial u}{\partial Y} \right) = - \frac{dp}{dx} + \frac{1}{r^j} \frac{\partial}{\partial Y} \left(r^j \mu \bar{\epsilon} \frac{\partial u}{\partial Y} \right) \quad (7.29)$$

Energy

$$\rho \left(u \frac{\partial T}{\partial x} + v^+ \frac{\partial T}{\partial Y} \right) = u \frac{dp}{dx} + \frac{1}{r^j} \frac{\partial}{\partial Y} \left(r^j \frac{\hat{\mu} \bar{\epsilon}}{\sigma} \frac{\partial T}{\partial Y} \right) + \mu \bar{\epsilon} \left(\frac{\partial u}{\partial Y} \right)^2 \quad (7.30)$$

The equation of state (eq. (7.17)) and the viscosity law (eq. (7.18)) may be expressed as follows:

Equation of State

$$P = \left(\frac{\gamma - 1}{\gamma} \right) \rho T \quad (7.31)$$

Viscosity Law

$$\mu = T^{3/2} \left(\frac{1 + S}{T + S} \right) \text{ (air only)} \quad (7.32)$$

where $S = S^*/T_{\text{ref}}^*$.

The boundary conditions for the system of equations in the stretched, non-dimensional plane are presented in figure 3.

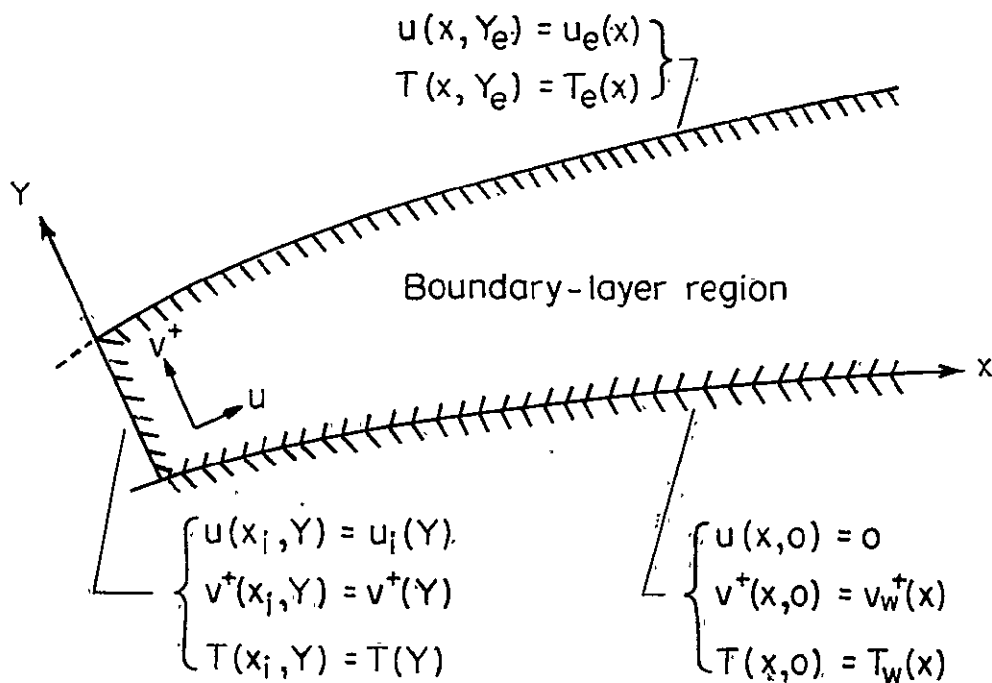


Figure 3.- Boundary conditions in the stretched plane.

7.3 The System of Transformed Equations

The system of governing equations is singular at $x = 0$. The Probstein-Elliott (ref. 20) and Levy-Lees (ref. 21) transformation can be utilized to remove this singularity as well as control the growth of the boundary layer as the solution proceeds downstream. In reference 16, Davis and Flügge-Lotz obtained solutions to the laminar boundary layer equations in the real plane for axisymmetric flows. However, the solutions were obtained for only a few nose radii downstream of the stagnation point and the boundary layer growth problem was not serious. If solutions are required many nose radii downstream, say on the order of 1,000, then the boundary layer growth can cause problems if the solution is obtained in the physical plane unless provisions are made for checking and adding additional grid-point when required.

The transformation utilized can be written as follows:

$$\xi(x) = \int_0^x \rho_e u_e \mu_e r_o^{2j} dx \quad (7.33a)$$

$$\eta(x, Y) = \frac{\rho_e u_e r_o^j}{\sqrt{2\xi}} \int_0^Y t^j \frac{\rho}{\rho_e} dY \quad (7.33b)$$

where the parameter t appearing in equation (7.33b) is the transverse curvature term and is defined as

$$t = 1 + \frac{\omega Y}{r_o} \cos \phi \quad (7.34)$$

The relation between derivatives in the old (x, Y) and new (ξ, η) coordinate systems are as follows:

$$\left. \begin{aligned} \left(\frac{\partial}{\partial x} \right)_Y &= \rho_e u_e \mu_e r_o^{2j} \left(\frac{\partial}{\partial \xi} \right)_\eta + \left(\frac{\partial \eta}{\partial x} \right) \left(\frac{\partial}{\partial \eta} \right)_\xi \\ \left(\frac{\partial}{\partial Y} \right)_x &= \frac{\rho_e u_e r_o^{jt} j}{\sqrt{2\xi}} \left(\frac{\partial}{\partial \eta} \right)_\xi \end{aligned} \right\} \quad (7.35)$$

Two new parameters, F and Θ are introduced and are defined as

$$\left. \begin{aligned} F &= u/u_e \\ \Theta &= T/T_e \end{aligned} \right\} \quad (7.36)$$

as well as a transformed normal velocity

$$V = \frac{2\xi}{\rho_e u_e \mu_e r_o^{2j}} \left[F \left(\frac{\partial \eta}{\partial x} \right) + \frac{\rho v^+ r_o^{jt} j}{\sqrt{2\xi}} \right] \quad (7.37)$$

The governing equations in the transformed plane can be expressed as follows:

Continuity

$$\frac{\partial V}{\partial \eta} + 2\xi \frac{\partial F}{\partial \xi} + F = 0 \quad (7.38)$$

Momentum

$$2\xi F \frac{\partial F}{\partial \xi} + V \frac{\partial F}{\partial \eta} - \frac{\partial}{\partial \eta} \left(t^{2j} \epsilon \frac{\partial F}{\partial \eta} \right) + \beta(F^2 - \Theta) = 0 \quad (7.39)$$

Energy

$$2\xi F \frac{\partial \Theta}{\partial \xi} + v \frac{\partial \Theta}{\partial \eta} - \frac{\partial}{\partial \eta} \left(t^{2j} \frac{\lambda}{\sigma} \frac{\partial \Theta}{\partial \eta} \right) - \alpha \lambda t^{2j} \left(\frac{\partial F}{\partial \eta} \right)^2 = 0 \quad (7.40)$$

where

$$\left. \begin{aligned} \lambda &= (\rho u) / (\rho u)_e \\ \alpha &= u_e^2 / T_e \\ \beta &= \frac{2\xi}{u_e} \left(\frac{du_e}{d\xi} \right) \end{aligned} \right\} \quad (7.41)$$

The parameter λ can be written by using the viscosity relation (eq. (7.32)) and the equation of state (eq. (7.31)) as

$$\lambda = \sqrt{\Theta} \left(\frac{1 + \bar{S}}{\Theta + \bar{S}} \right) \text{ (air only)} \quad (7.42)$$

where $\bar{S} = S / T_e$.

The transverse curvature term can be expressed in terms of the transformed variables as

$$t = \pm \left(1 + \frac{2\omega \sqrt{2\xi} \cos \phi}{\rho_e u_e} \int_0^\eta \frac{\rho_e}{\rho} d\eta \right)^{1/2} \quad (7.43)$$

where the \pm sign in equation (7.43) is required in order to obtain solutions for axisymmetric boundary layer flows over a body or inside a duct (nozzle), respectively.

The physical coordinate normal to the wall in the stretched real plane is obtained from the inverse transformation; namely

$$Y = \frac{r_0}{\omega \cos \phi} \left[-1 \pm \left(\frac{1 + 2 \sqrt{2\xi} \omega \cos \phi}{\rho_e u_e r_0^2} \int_0^\eta \Theta d\eta \right)^{1/2} \right] \quad (7.44)$$

The selection of the correct sign in equation (7.44) is made on the basis of + for axisymmetric flow over bodies of revolution and - for flow inside of axisymmetric ducts (nozzles).

The y-coordinate in the physical plane is obtained from equations (7.25), (7.27), and (7.44); that is, $y = \omega Y$.

The boundary conditions in the transformed plane are as follows:

Wall Boundary

$$\left. \begin{aligned} F(\xi, 0) &= 0 \\ V(\xi, 0) &= V_w(\xi) \\ \Theta(\xi, 0) &= \Theta_w(\xi) \end{aligned} \right\} \quad (7.45a)$$

Edge Conditions

$$\left. \begin{aligned} F(\xi, \eta_e) &= 1 \\ \Theta(\xi, \eta_e) &= 1 \end{aligned} \right\} \quad (7.45b)$$

The boundary condition at the wall for the transformed V component can be related to the physical plane as

$$V_w = \frac{\sqrt{2\xi}}{\omega u_e r_0^2} \left(\frac{\rho_w \tilde{v}_w}{\rho_e u_e} \right) \quad (7.46)$$

where the no-slip constraint has been imposed on equation (7.37). It should be noted that the apparent mass flux term appearing in equations (7.4) and (7.5) is zero at the wall. Therefore equation (7.46) can be expressed in terms of the physical mass flux at the wall as

$$V_w = \frac{\sqrt{2\xi}}{\omega_{erj}^j} \left(\frac{\rho_w^* v_w^*}{\rho_e^* u_e^*} \right) \quad (7.47)$$

7.4 Eddy Viscosity and Eddy Conductivity Models

7.4.1 Physical Plane

The turbulent boundary layer can be treated as a composite layer consisting of an inner and outer region as shown schematically in figure 4. (See Bradshaw, reference 22.)

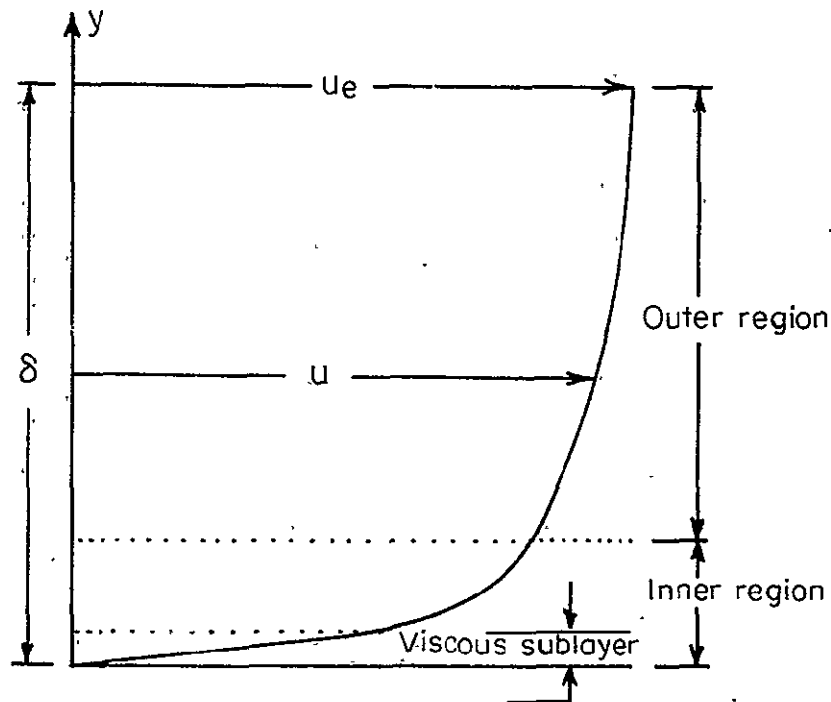


Figure 4.- Two-layer turbulent boundary-layer model.

The thickness of the inner region ranges between 0.18 to 0.28. The character of the flow depends primarily on the shear stress at the wall, τ_w and the molecular viscosity, μ . The mean velocity distribution in this region responds quickly to changes in the wall conditions since the turbulent eddy structure is small. The mean velocity distribution is characteristically described by the "law of the wall" relation

$$\frac{u}{u_\tau} = \Omega_1 \left(\frac{y^* u_\tau^*}{\nu^*} \right) \quad (7.48)$$

The law of the wall relation was first derived by Prandtl (ref. 23). If the wall is smooth the inner region will contain a sublayer, usually referred to in the literature as either the laminar sublayer or the viscous sublayer, adjacent to the wall.

The viscous sublayer is very thin in relation to the total boundary-layer thickness. The thickness of the sublayer usually ranges between 0.0018 to 0.018. The layer is highly viscous in character; consequently, the mean velocity is a linear function of y . For the viscous sublayer, equation (7.48) can be written as

$$\frac{u}{u_\tau} = \frac{y^* u_\tau^*}{\nu^*} \quad (7.49)$$

The relative thinness of the viscous sublayer, and its importance in determining the correct shear stress and heat flux at the wall requires that very small grid-point spacing in the y -direction be utilized in the wall region for the numerical procedure used in the present

analysis. This particularly important point is discussed in Section 8.1.

The outer region of the turbulent boundary layer is very thick in relation to the wall region. It ranges in thickness from 0.8 δ to 0.9 δ . The flow in this region is basically independent of the molecular viscosity, dependent upon the wall shear stress, and strongly affected by boundary layer edge conditions such as pressure gradients in the streamwise direction, dP/dx . The mean velocity distribution for the outer region is usually described by the velocity-defect law:

$$\frac{u_e - u}{u_\tau} = \Omega_2\left(\frac{y}{\delta}\right) \quad (7.50)$$

The basic argument leading to the form of the velocity-defect law is that the reduction in velocity, $u_e - u$ at a distance y from the wall is the result of a tangential stress at the wall, independent of how the stress arises but dependent on the distance to which the effect has diffused from the wall. The flow in the outer region shows similarity to wake flow, and the eddy structure is large scale in relation to the inner region. Consequently, the response of the mean velocity distribution to changes in boundary conditions is quite slow. The eddy viscosity model, then, must characterize these basic flow structures if it is to yield accurate results. For additional discussion on the inner and outer regions see references 2 and 24.

Inner Region Model

The eddy viscosity model used in the present analysis for the inner region is based on the mixing-length hypothesis as developed by Prandtl (ref. 25) in 1925. The eddy viscosity for this region referenced to the molecular viscosity may be expressed as follows:

$$\left(\frac{\epsilon}{\mu}\right)_i = \frac{\rho \bar{l}^{*2}}{\mu^*} \left| \frac{\partial u^*}{\partial y^*} \right| \quad (7.51)$$

where \bar{l}^* , the mixing length, may be written as

$$\bar{l}^* = K_1 y^* \quad (7.52)$$

The value of K_1 has been obtained experimentally and has a value of approximately 0.4, the value which will be used in the present analysis. However, Van Driest (ref. 26) concluded from an analysis based upon experimental data and the second problem of Stokes (ref. 27) (sometimes referred to as the Rayleigh problem, ref. 28) that the correct form for the mixing length in the viscous sublayer should be as follows:

$$\bar{l}^* = K_1 y^* \left[1 - \exp\left(-\frac{y^*}{A^*}\right) \right] \quad (7.53)$$

where the exponential term is due to the damping effect of the wall on the turbulent fluctuations. The parameter A^* is usually referred to as the damping constant. The exponential term approaches zero at the outer edge of the viscous sublayer so that the law of the wall region equation, as expressed in equation (7.52) is valid. The damping

constant A^* is a strong function of the wall boundary conditions and is defined as

$$A^* = 26\nu^* \left(\frac{\tau_w^*}{\rho^*} \right)^{-1/2} \quad (7.54)$$

Equation (7.54) was originally obtained for incompressible, zero pressure gradient, solid wall flow; that is, $\rho^* = \text{constant}$, $dp^*/dx^* = 0$ and $\tilde{v}_w^* = 0$. The relation has, however, been applied to compressible flows where ρ^* and ν^* are evaluated locally across the sublayer, where ρ^* is evaluated locally and an average value of ν^* is utilized, and where ν^* and ρ^* are both evaluated at the wall conditions. In the present analysis the mixing length will be defined as follows

$$\bar{l}^* = K_1 y^* \left\{ 1 - \exp \left[- \left(\frac{\nu_w^*}{\bar{\nu}^*} \right)^{1/2} \frac{y^*}{A^*} \right] \right\} \quad (7.55)$$

where $\bar{\nu}^*$ is the average value of the kinematic viscosity taken over the viscous sublayer. The density and viscosity appearing in equation (7.54) will be evaluated locally. The eddy viscosity for the inner region referenced to the molecular viscosity can then be written as

$$\left(\frac{\epsilon}{\mu} \right)_i = \frac{\rho^* K_1^2 y^{*2}}{\mu^*} \left[1 - \exp \left(- \sqrt{\frac{\nu_w^*}{\bar{\nu}^*}} \frac{y^*}{A^*} \right) \right]^2 \left| \frac{\partial u}{\partial y} \right|^* \quad (7.56)$$

where A^* is defined in equation (7.54).

Cebeci (ref. 29) has recently attempted to account for the effects of both pressure gradient and mass injection or removal at the wall on the damping constant. Cebeci begins with the two-dimensional x-momentum equation written as

$$u^* \frac{\partial u^*}{\partial x^*} + \tilde{v}^* \frac{\partial u^*}{\partial y^*} = - \frac{1}{\rho^*} \frac{dp^*}{dx^*} + \frac{1}{\rho^*} \frac{\partial}{\partial y^*} \left(\mu^* \frac{\partial u^*}{\partial y^*} - \rho^* \overline{u^* v^*} \right) \quad (7.57)$$

Cebeci then neglects the Reynolds stress term and assumes that in the wall region equation (7.57) can be written as ($\tilde{v}_w^* = 0$)

$$\frac{d\tau^*}{dy^*} = \frac{dp^*}{dx^*} \quad (7.58)$$

which becomes upon integration

$$\tau^* = \tau_w^* + \left(\frac{dp^*}{dx^*} \right) y^* \quad (7.59)$$

It should be noted that for $\tilde{v}_w^* = 0$ it is not necessary to neglect the Reynolds stress term; that is, τ^* in equation (7.59) could be replaced with τ_{Π}^* . However, if $\tilde{v}_w^* = 0$ the Reynolds stress term must be neglected in the approach used by Cebeci. The wall shear stress term τ_w^* appearing in equation (7.54) is then replaced by the local shear such that a new definition for the damping constant is obtained; that is

$$A^* = 26\nu^* \left(\frac{\tau_w^*}{\rho^*} + \frac{dp^*}{dx^*} \frac{y^*}{\rho^*} \right)^{-1/2} \quad (7.60)$$

This approach is similar to that followed by Patankar and Spalding (ref. 30) where they utilized the local value of τ^* in equation (7.54) instead of the wall value, τ_w^* .

The assumptions made by Cebeci in obtaining equation (7.60) are not necessarily valid. Furthermore, as previously mentioned, the flow in the outer region of the turbulent boundary layer is predominately affected by pressure gradients and not the flow in the law of the wall region. Consequently, the pressure gradient correction to the damping constant as obtained by Cebeci is of questionable value and will not be utilized in the present analysis.

The effect of mass flux at the wall has also been treated by Bushnell and Beckwith (ref. 31) and Cebeci (ref. 29). Cebeci, for non-zero \tilde{v}_w^* expresses equation (7.57) as

$$\frac{d\tau^*}{dy^*} - \frac{\tilde{v}_w^*}{\nu^*} \tau^* - \frac{dp^*}{dx^*} = 0 \quad (7.61)$$

which can be integrated to yield

$$\tau^* = \tau_w^* \exp\left(\frac{\tilde{v}_w^*}{\nu^*} y^*\right) + \frac{\nu^*}{\tilde{v}_w^*} \frac{dp^*}{dx^*} \left[\exp\left(\frac{\tilde{v}_w^*}{\nu^*} y^*\right) - 1 \right] \quad (7.62)$$

Equation (7.54) can then be written as (where τ_w^* has been replaced with τ^*)

$$A^* = 26\nu^* \left\{ \frac{\tau_w^*}{\rho^*} \exp\left(\frac{\tilde{v}_w^*}{\nu^*} y^*\right) + \frac{\nu^*}{\tilde{v}_w^*} \frac{1}{\rho^*} \left(\frac{dp^*}{dx^*} \right) \left[\exp\left(\frac{\tilde{v}_w^*}{\nu^*} y^*\right) - 1 \right] \right\}^{-1/2} \quad (7.63)$$

Bushnell and Beckwith (ref. 31) studied the effect of wall mass flux on the damping constant from experimental data for zero pressure-gradient flow. These results agree well with equation (7.63) for zero pressure-gradient flows; that is

$$A^* = 26\nu^* \left[\frac{\tau_w^*}{\rho^*} \exp\left(\frac{\tilde{v}_w^*}{\nu^*} y^*\right) \right]^{-1/2} \quad (7.64)$$

Two apparently conflicting ideas by the author of the present paper should now be discussed concerning the development of Cebeci (ref. 29). First, it has been stated that equation (7.60) is of questionable value for pressure gradient flows. Secondly, it has been stated by the author that equation (7.64) agrees well with experimental values of A^* for non-zero \tilde{v}_w^* . However, equations (7.60) and (7.64) were both obtained from equation (7.57) by utilizing the same set of assumptions. Consequently, the question arises as to how can equation (7.60) be of questionable value, and equation (7.64) be of value? The answer lies not so much in the derivation but more so in the response of the turbulent boundary layer to pressure gradients and changes in wall boundary conditions. It is well known that pressure gradients affect the mean profiles mainly in the outer region, but equation (7.60) is applied only in the inner region; in particular, only in the viscous sublayer. However, the mean profiles in the inner region are particularly sensitive to wall boundary conditions which is precisely where equation (7.64) is applied.

Outer Region Model

The eddy viscosity in the outer region is based upon the Clauser (ref. 32) model. The ratio of the eddy viscosity to the molecular viscosity can be expressed as follows:

$$\left(\frac{\epsilon}{\mu}\right)_o = K_2 \frac{\rho^* u_e^*}{\mu^*} \delta_{k_{inc}}^* \quad (7.65)$$

where $\delta_{k_{inc}}^*$ is the incompressible displacement thickness defined as

$$\delta_{k_{inc}}^* = \int_0^{y_e^*} (1 - F) dy^* \quad (7.66)$$

The use of $\delta_{k_{inc}}^*$ as the scaling parameter for the mixing length is discussed by Maise and McDonald (ref. 33). (See also, Morkovin, ref. 34.) The value of K_2 in equation (7.65) is taken to be 0.0168 as reported in reference 35. However, in order to account for the intermittent character of the outer layer flow equation (7.65) must be modified by an intermittency factor first obtained by Klebanoff (ref. 36); that is

$$\left(\frac{\epsilon}{\mu}\right)_o = K_2 \frac{\rho^* u_e^*}{\mu^*} \delta_{k_{inc}}^* \bar{\gamma} \quad (7.67)$$

where the transverse intermittency factor $\bar{\gamma}(y)$ is defined as

$$\bar{\gamma} = \frac{1 - \operatorname{erf}\left[5\left(\frac{y}{\delta} - 0.78\right)\right]}{2} \quad (7.68)$$

Matching Procedure

The criteria used to determine the boundary between the inner and outer regions is the continuity of eddy viscosity. A sketch of a typical eddy viscosity distribution is presented in figure 5.

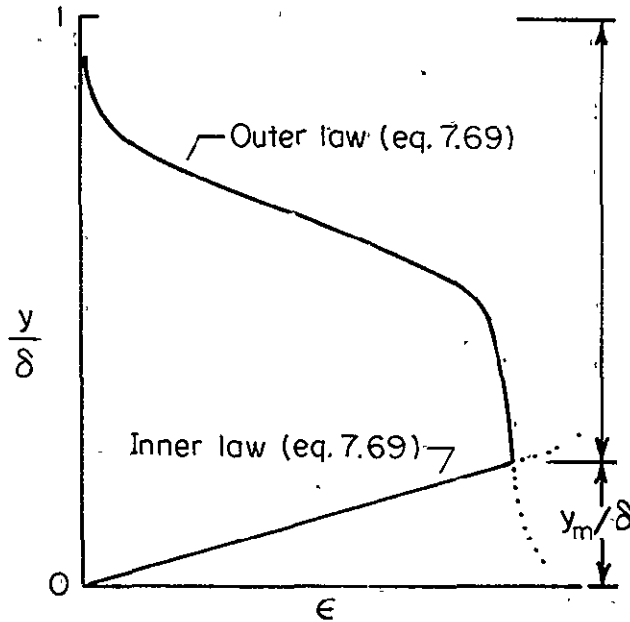


Figure 5.- Matching procedure for two-layer model.

The matching procedure may then be formally written as follows:

$$\left. \begin{aligned} \left(\frac{\epsilon}{\mu}\right)_i &= \frac{\rho^* K_1^2 y^{*2}}{\mu^*} \left\{ 1 - \exp \left[- \left(\frac{v_w^*}{v^*} \right)^{1/2} \frac{y^*}{A^*} \right] \right\}^2 \left| \frac{\partial u^*}{\partial y^*} \right| & 0 \leq y^* \leq y_m^* \\ \left(\frac{\epsilon}{\mu}\right)_o &= \frac{\rho^* K_2 u^*}{\mu^*} \delta_{kinc}^* \bar{\gamma} & y^* > y_m^* \end{aligned} \right\} \quad (7.69)$$

The location of the boundary separating the two regions, y_m^* is determined from the continuity of equations (7.69); that is, where

$$\left(\frac{\epsilon}{\mu}\right)_o = \left(\frac{\epsilon}{\mu}\right)_i \quad (7.70)$$

Eddy Conductivity

In Section 7.1.2 the eddy conductivity was formulated in terms of a static turbulent Prandtl number and the eddy viscosity (see eqs. (7.9), (7.10), and (7.11)). The two-layer model eddy viscosity relation previously discussed suggests that there should be two models for the static turbulent Prandtl number, σ_t . However, current experimental data for σ_t are inconclusive. The incompressible data which are available for the outer region of pipe flows (ref. 37) and boundary layers (ref. 38) indicate that σ_t has a value between 0.7 to 0.9. These data indicate that as the wall is approached σ_t reaches a maximum value near the wall and then drops off rapidly to a value between 0.5 and 0.7 at the wall. For the case of compressible flow there is very little data available. For a Mach number of 5 it appears that σ_t assumes a value very near unity in the outer region and decreases to values on the order of 0.7 to 0.9 at the wall (ref. 39). However, Rotta (ref. 40) found that σ_t may achieve values as high as 2 as the wall is approached. Bushnell and Beckwith (ref. 31) conclude that in the absence of better data for turbulent Prandtl numbers, the choice of the correct σ_t distribution with y/δ must depend upon agreement between the calculated and experimental profiles and wall fluxes. In the present analysis the turbulent Prandtl number will be assumed constant with a value of 0.9 unless specifically stated otherwise; however, any other value or functional relationship could just as easily be used.

7.4.2 Transformed Plane

Since the governing equations are solved in the transformed plane it is necessary to transform the eddy viscosity relations from the real plane to the transformed plane.

Inner Region

In the inner region the ratio of eddy viscosity to molecular viscosity is as follows

$$\left(\frac{\epsilon}{\mu}\right)_i = \frac{\rho_e^2 u_e^2 K_1^2 r_o^j}{\mu_e \omega \sqrt{2\xi}} + j \frac{Y^2 \Pi^2}{\omega \beta} \left| \frac{\partial F}{\partial \eta} \right| \quad (7.71)$$

where Y is defined by equation (7.44). The parameter Π appearing in equation (7.71) is the damping term and is defined as

$$\Pi = 1 - \exp(-\Pi_1 \Pi_2) \quad (7.72)$$

where

$$\Pi_1 = \sqrt{\frac{l_w}{\bar{l}}} \left(\frac{\Theta_w}{\Theta} \right) \quad (7.73)$$

and

$$\Pi_2 = \frac{Y \rho_e u_e}{26 \omega^2 \mu_e} \left\{ \frac{\Theta}{\omega} \left[\frac{\mu_e r_o^j l_w}{\sqrt{2\xi}} \left(\frac{\partial F}{\partial \eta} \right)_w \right] \right\}^{1/2} \quad (7.74)$$

Outer Region

In the outer region the ratio of eddy viscosity to molecular viscosity is as follows:

$$\left(\frac{\epsilon}{\mu}\right)_o = \frac{\rho_e u_e}{\mu_e} \frac{K_2}{\omega^2} \frac{\bar{\gamma} \delta_{k_{inc}}}{l\theta^2} \quad (7.75)$$

where

$$\bar{\gamma} = \frac{1 - \operatorname{erf} 5(Y/Y_e - 0.78)}{2} \quad (7.76)$$

and

$$\delta_{k_{inc}} = \frac{\omega \sqrt{2\xi}}{\rho_e u_e r_o^j} \int_0^{\eta_e} t^{-j} \Theta(1 - F) d\eta \quad (7.77)$$

7.5 The Transition Region

Equations (7.38), (7.39), (7.40), and (7.42) together with the boundary conditions (eqs. (7.45)), and the eddy viscosity relations defined by equations (7.71) and (7.75) complete the required system for either laminar or fully developed turbulent boundary layer flows.

However, the main objective of the present analysis is to present a technique that will efficiently solve the laminar, transitional, or turbulent boundary layer equations as the boundary layer develops along the surface. Consequently, the location of transition $x_{t,i}$, the extent of the transitional flow $x_{t,f} - x_{t,i}$, and the characteristics of the

mean flow structure in the transition region must be taken into consideration.

The author in developing this section on transition flow has had to purposely omit many excellent references because of the massive bulk of information available. A number of the cited references present extensive reviews on the subject and should be consulted for more information if required.

7.5.1 Stability and Transition

The stability of laminar shear flows and the eventual transition from the laminar state to the turbulent state of motion has probably received as much concentrated attention as any other problem area in fluid mechanics. The continuing interest in this area of fluid mechanics is due to the fundamental importance of being able to make a realistic prediction of where and if transition will occur on a given configuration in a given environment. The influence of many parameters which affect transition has been studied and documented; however, after nearly sixty years of research contradictions or paradoxes still remain unanswered even for incompressible flows. Pioneers in transition research were impressed by the three-dimensionality of turbulence and did not seriously consider the possible role of any two-dimensional amplification process such as predicted by the early stability work (see ref. 2). This attitude was understandable since the results from the Tollmien-Schlichting (hereafter referred to as T-S) school of thought predicted an orderly vorticity pattern which differed drastically from the observed random three-dimensional vorticity

components of transitional and turbulent boundary layer flows. The problem was further complicated by the high level of free-stream turbulence that existed in the early wind tunnels which apparently prevented the development of the T-S type amplification process. Furthermore, due to the limited amount of transition data and its apparent agreement with Taylor's (ref. 41) local separation criteria there was no widespread acceptance of the T-S process until about 1947. The first indication that the T-S amplification process existed was obtained by Schubauer and Skramstad (ref. 42) in their classical experimental study of flat plate flow in the low free-stream turbulence tunnel of the National Bureau of Standards.

The T-S instability arises from the viscous instability in the laminar shear layer. It is a two-dimensional wave motion that selectively amplifies disturbances over a band of unstable frequencies. C. C. Lin (refs. 43 and 44) was able to calculate with very good agreement the results of the Schubauer-Skramstad experiment. Klebanoff and Tidstrom (ref. 45) were able to trace the growth of the unstable waves into the nonlinear region of transition where the T-S approach becomes invalid. They observed that when the velocity perturbation due to the wave exceeded approximately 10 percent of the mean speed the nonlinear effects became important. Any further development of the mean flow instability was then three-dimensional. In this region of the transition process "peaks and valleys" form consisting of variations in mean cross flow. The "peaks and valleys" eventually break down and form turbulent "spots."

A turbulent spot is essentially an isolated region of turbulent flow surrounded by an otherwise laminar flow field. It has been established that the flow within the spot has the same basic characteristics as that of a fully developed turbulent flow. The existence of these isolated spots of turbulence was first reported by Emmons (ref. 46) in 1951 (see also ref. 47). Klebanoff, Schubauer, and co-workers (ref. 48) were the first to carefully study the shape of the spots and their characteristics. They confirmed that the flow within a given spot was turbulent in nature, that the spot propagated through the surrounding flow field, and that the spot grew in size as it was convected downstream. The transition process is completed by either, or both, the transverse growth of spots or cross-contamination and the creation or production of new spots at new transverse locations. When the entire flow region at some streamwise location $x_{t,f}$ is covered by a turbulent flow structure the boundary layer is then said to be fully turbulent.

The natural transition process by which a fully developed flow structure is obtained may be categorically divided into six separate stages. The first stage, of course, is the laminar region of the boundary layer. The second stage begins with the formation of two-dimensional unstable waves arising from an instability in the laminar layer. The third stage, which marks the beginning of the nonlinearity, is the formation of "peaks and valleys" or longitudinal streaks in the mean velocity profiles. The fourth stage occurs with the breakdown

of one or more of the low-speed streaks and the formation of "spots" of turbulence. The fifth stage consists of the growth of the spots through cross contamination and the process of new spot creation (production). The sixth and final stage in natural transition is then fully developed turbulent layer. (See Kline, S.J., reference 49.)

Stability theory cannot currently be used to predict either the nonlinear details of the transition process after the two-dimensional waves have been amplified or the location of transition, $x_{t,i}$. Stability theory can, however, establish which boundary layer profiles are unstable and the initial amplification rates. The theory can identify those frequencies which will be amplified at the greatest rate as well as the effect on stability of various flow parameters. One of the more important contributions of linear stability theory has been to reveal how these flow parameters should be varied in order to delay transition, i.e., wall cooling, suction, etc. The Blasius profile was studied by Tollmein (ref. 50) in 1929. The results of his work remained unconfirmed experimentally until the classical experiments of Schubauer and Skramstad in 1947 (ref. 42). Since the beginning of the past decade the solution techniques utilized in stability theory have been greatly modified by the availability of high-speed digital computer systems. Now, instead of having to work many hours in order to obtain a minimum of results of questionable accuracy, the digital computer can obtain an immense quantity of highly accurate numerical results from the governing system of equations. A review of methods used to predict the location of transition from stability theory is presented by Jaffe,

Okamura, and Smith in reference 51. However, a point which should be strongly stressed is that a thorough study of the connection between stability and transition still remains to be completed.

There currently exists a number of good review articles and books on stability theory. Review articles have been written by Stuart (ref. 4), Shen (ref. 52), Reed (ref. 53), and Drazin and Howard (ref. 54).. The article by Reed considers asymptotic theory in detail. Drazin and Howard in turn consider only the inviscid theory. The articles by Schlichting (ref. 2) should also not be overlooked. The most complete study of modern boundary-layer stability, in the opinion of the author, is presented by Mack (ref. 55).

7.5.2 Transition Location

Many parameters influence the location of transition. These parameters can best be thought of as forming a parameter phase space. Such a parameter phase space would include Reynolds number, Mach number, unit Reynolds number, surface roughness, nose bluntness, pressure gradients, boundary conditions at the wall, angle-of-attack, free-stream turbulence level, and radiated aerodynamic noise. Morkovin (ref. 9) recently completed a very extensive and thorough examination of the current state-of-the-art of transition in shear layers from laminar to turbulent flow. The most striking conclusion that one obtains from the review is that although a great bulk of experimental data on transition currently exists, much of the information on high-speed transition has not been documented in sufficient detail to allow the separation of the effects of multiple parameters on transition. A

discussion of the effects of each of the parameters that may influence transition in high-speed flow is beyond the scope of the present paper. Furthermore, it is seldom possible to study any one parameter experimentally while holding the remaining parameter phase space constant. The reader interested in a detailed discussion is directed to the paper by Morkovin (ref. 9) where over 300 related references are cited and discussed. The paper by Săvulescu (ref. 8) should also be consulted. Another, although less detailed discussion, is presented by Fischer (ref. 56). The effects of radiated aerodynamic noise on transition is discussed by Pate and Schueler (ref. 57). Hypersonic transition, to name but a few references, is discussed by Softley, Grabel, and Zemple (ref. 58); Richards (ref. 59), Potter and Whitfield (ref. 60), and Deem and Murphy (ref. 61). A very good discussion on the effects of extreme surface cooling on hypersonic flat-plate transition is presented by Cary (ref. 62). The effects of nose bluntness and surface roughness on boundary layer transition are discussed by Potter and Whitfield (ref. 63).

It would be prohibitively time consuming to obtain a detailed stability analysis for each of the test cases considered in the present paper (see Chapter IX). Furthermore, even if such an analysis were completed the transition location would not be obtained. Consequently, in the present analysis the location of transition will be determined by one of, or a combination of, the following three methods. These methods are (1) a stability index or vorticity Reynolds number first proposed by Rouse (ref. 64), (2) correlations based upon a collection

of experimental data over a broad range of test conditions, and (3) by using the measured experimental location of transition as a direct input into the analytical solution. One might immediately assume that the latter of the three methods would be the most accurate; however, caution must be exercised in interpreting and applying the results of experimental transition measurements since data on all parameters that may affect transition are seldom available. Also, the transition location may very well be a function of the method used to obtain the experimental data. There are a number of ways to experimentally measure the transition location which often yields different locations for the identical boundary layer. This fact has contributed to much of the current confusion and scatter that results when attempts are made to correlate a great number of experimental transition data obtained in a number of different investigations without considering how transition was determined.

7.5.2.1 Stability Index

Hunter Rouse (ref. 64) nearly 25 years ago obtained through a process of dimensional analysis combined with observed fluid motion that a stability index could be expressed as follows:

$$\chi = \frac{y^{*2}}{\nu^*} \frac{\partial u^*}{\partial y^*} \quad (7.78)$$

This index has the form of a vorticity Reynolds number which is obtained from the ratio of the local inertial stress $\rho^* y^{*2} (\partial u^* / \partial y^*)^2$, to the local viscous stress $\mu^* (\partial u^* / \partial y^*)$. Rouse assumed that in order

for transition to occur the stability index should reach some limiting value which was assumed invariant. He was able to further show that this invariant value, $(X_{\max})_{cr}$ should be on the order of 500 for incompressible flows.

The use of X_{\max} as a stability index is in principle similar to the basic reasoning which led O. Reynolds (ref. 7) in 1883 to postulate that the nondimensional parameter ud/ν could be used to define a critical value $(ud/\nu)_{cr}$ at which transition would occur in a circular pipe of diameter, d . Unfortunately, $(X_{\max})_{cr}$ is a function of the transition parameter phase space in much the same fashion as the critical Reynolds number, and cannot in reality be a true invariant of the flow as suggested by Rouse (see Section 9.8; fig. 19). The stability index does, however, possess a number of important characteristics which can be directly related to the stability of laminar flows; for example, the position of the critical layer can be obtained directly from equation (7.78).

A typical transverse distribution of X for a compressible laminar boundary layer is presented in figure 6. The stability index has a zero value at the wall and approaches zero as the outer edge of the layer is approached. The maximum value of X , X_{\max} , will occur at some transverse location, $(y/\delta)_{X_{\max}}$. The values of X_{\max} and $(y/\delta)_{X_{\max}}$ are of importance in the usage of the stability index as a guide to boundary layer stability and transition.

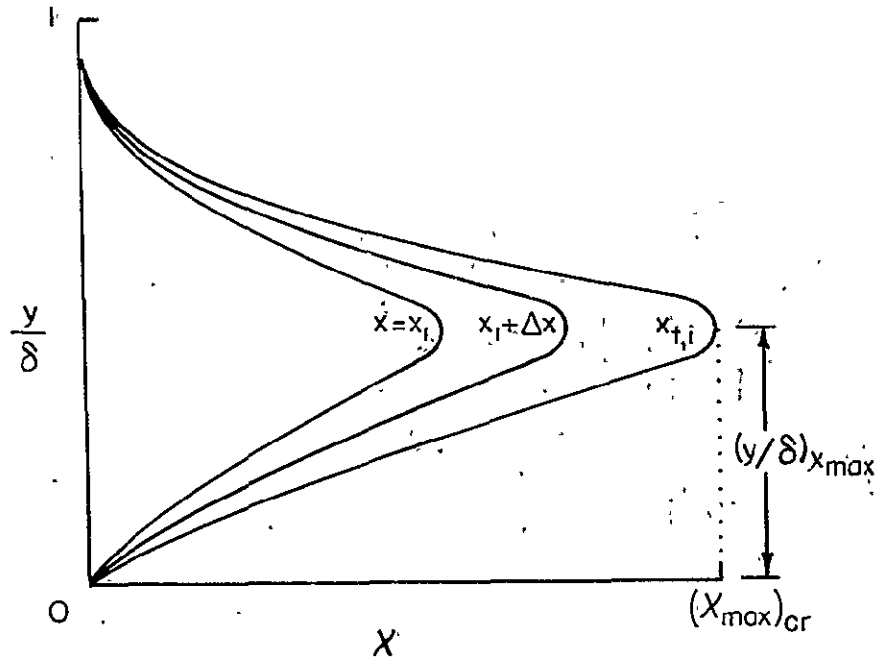


Figure 6.- Vorticity Reynolds number.

As the laminar boundary layer develops over a surface, x_{\max} increases monotonically until the critical value $(x_{\max})_{cr}$ is reached at which point transition is assumed to occur; that is, the location of $x_{t,i}$. For compressible flows $(x_{\max})_{cr}$ is not an invariant. In the present study $(x_{\max})_{cr}$ was found to vary from approximately 2100 to values on the order of 4000. The variation of $(x_{\max})_{cr}$ is a strong function of unit Reynolds number for data obtained in air wind tunnel facilities (see Section 9.8) as would be expected from the previously mentioned transition studies. However, while not invariant the stability index does exhibit the same dependence on various parameters as results from the more complicated stability theory. For example, at

a given streamwise location, x , the value of x_{\max} is found to decrease (which implies a more stable flow) with wall cooling, wall suction, and favorable pressure gradients, whereas it increases (which implies a more unstable flow) with wall heating, mass injection (transpiration), and adverse pressure gradients. To the author's knowledge the stability index has been used as a correlation parameter in only two boundary-layer transition studies. A modified form of the parameter was used to correlate the effect of free-stream turbulence on transition by Van Driest and Blumer (ref. 65). Correlation attempts, using Rouse's original invariant assumptions, were made in reference 66; however, the results were only fair.

One of the most important characteristics of the vorticity Reynolds number is that the value of $(y/\delta)_{x_{\max}}$ is in excellent agreement with the experimental location of the critical layer which represents the distance normal to the wall at which the first high frequency burst representing laminar flow breakdown will occur. Stainback (ref. 67) recently obtained the Rouse stability index for similar laminar boundary layer flows over a broad range of wall-to-total temperature ratios for Mach numbers up to 16. The numerical calculations were made for both air and helium boundary layers. The agreement between $(y/\delta)_{x_{\max}}$ and the experimental critical layer position was excellent over the entire range. (See Section 9.3.)

7.5.2.2 Empirical Correlations

In most instances the design engineer has to rely on empirical correlations of experimental transition data in order to fix the most probable transition location for a design configuration. However, caution should always be used when obtaining the most probable location of transition from such correlations, since any given correlation is based upon a specific collection of data which will not be completely general. Furthermore, the transition process may not be unique; for example, the blunt-body transition paradox (see refs. 9 and 68).

There currently exists a large number of empirical correlations for predicting the probable location of transition. Some of these correlations are of questionable value; however, some can be used with confidence providing it is realized that one is predicting a probable range of locations and not an exact fixed point. One of the more successful correlations was obtained by Beckwith (ref. 69) at the Langley Research Center. The correlation developed by Beckwith is based on experimental transition data obtained over a wide range of test conditions in air wind tunnels, ballistic ranges, and free flight. The correlation can be expressed as follows:

$$\log_{10} \left[\frac{Re_{\delta_t}^*}{Re^{*0.3}} \right] = I + JM_e(\theta_w)^{0.7 \exp(-0.05M_e^2)} \quad (7.79)$$

where Re_e^* denotes the unit Reynolds number per foot, u_e^*/ν_e^* . The constants I and J are functions the environment in which transition was measured and are given in the following table.

Facility	I	J
Air wind tunnel	0.95	0.167
Ballistic range	1.00	0.125
Free flight	1.32	0.130

Equation (7.79) can be expressed in terms of the transition Reynolds number, $Re_{x_{t,i}}$ as follows (see ref. 69):

$$Re_{x_{t,i}} = \frac{3}{2} \frac{Re^{*0.6}}{l_w} \frac{10 \left[2I + 2JM_e(\Theta_w)^{0.7 \exp(-0.05M_e^2)} \right]}{(0.094 M_e^2 + 1.22 \Theta_w)^2} \quad (7.80)$$

For an in-depth review of the problems associated with transition the reader is referred to the results of the Boundary Layer Transition Study Group meeting held in San Bernardino, California, in 1967 (refs. 69, 70, 71, and 72).

7.5.2.3 Experimental Transition

Much of the confusion that exists today concerning boundary layer transition may be attributed to one of, or a combination of, the following three factors. The first factor is that in many instances the investigator who made the experimental study may not have carefully measured or recorded the exact conditions under which the data were obtained. The second factor is that the experimentally observed transition location depends on the experimental technique used to obtain its location. The third, the most pessimistic factor, is that transition may not be a unique process under all conditions (ref. 9).

The importance of carefully measuring the environment under which the experiments are made cannot be overstressed. In the past, many of the factors which may influence transition such as free-stream turbulence and acoustic radiation from the tunnel side wall boundary layer were not measured. (See references 69 to 72.) The location of transition as obtained experimentally is a strong function of the method used to determine its location. There are currently a number of techniques used to obtain the transition location. Some of these methods are hot-wire traverses, pitot tube surveys near the wall, visual indication from schlieren photographs, and heat transfer measurements at the wall. Each of these methods basically measures a different flow process. Consequently, it would be misleading to believe that each technique would yield the same location for transition if simultaneously applied to the same boundary layer. Of course, the concept of a transition "point" is misleading in itself since transition does not occur at a "point" but instead over some finite size region.

For the test cases presented in the present analysis the experimental transition location will be determined from heat transfer measurements at the wall whenever possible. The main reason for this choice is that it is the method most often used in the literature. However, it should be noted that the actual nonlinear transition process begins somewhat upstream of the location where the heat transfer at the wall deviates from the laminar trend.

7.5.3 Transitional Flow Structure

Assuming that the transition location has been fixed for a given problem one must next consider the following two important factors; first, the length of the transition region, $x_{t,f} - x_{t,i}$ (sometimes referred to as transition extent), and secondly, the mean flow characteristics within the region. Once appropriate models are obtained for these two factors it is possible to smoothly connect all three flow regions such that one set of governing equations may be used.

The classical laminar boundary layer equations should yield reasonably accurate profiles and wall fluxes in the linear region of transition; that is, prior to the turbulent spot formation. The intermittent appearance of the turbulent spots and the process of cross-contamination is not well understood. The spots originate in a more or less random fashion and merge with one another as they grow and move downstream. Eventually, the entire layer is contaminated which marks the end of the transition process, $x_{t,f}$. The process by which cross-contamination occurs appears to have been studied in detail only by Schubauer and Klebanoff (ref. 73) since its discovery by Charters (ref. 74) in 1943. As the turbulent spots move over a fixed point in the transition region, the point experiences an alternation of fully laminar flow when no spot is present to fully turbulent flow when engulfed by a spot. These alternations can be described by an intermittency factor which represents the fraction of time that any point in the transition region is engulfed by fully turbulent flow.

The distribution of spots in time and space is Gaussian for low speed, natural transition. However, very little is known about the spot distribution in high speed compressible flow. Furthermore, there is no assurance that the spot formation and distribution in hypersonic flows will be analogous to the low speed model. However, in the absence of a more satisfactory theory, the author has chosen the approach of Dhwan and Narasimha (ref. 75) which was obtained mainly from low speed data. In reference 75 the source density function of Emmons (ref. 46) was used to obtain the probability distribution (intermittency) of the turbulent spots. Dhwan and Narasimha (ref. 75) obtained an intermittency distribution of the form

$$P(\bar{\xi}) = 1 - \exp(-0.412 \bar{\xi}^2) \quad (7.81)$$

where

$$\bar{\xi} = \frac{(x - x_{t,i})}{\lambda} \quad (7.82)$$

for $x_{t,i} \leq x \leq x_{t,f}$. The term $\bar{\xi}$ in equation (7.81) represents a normalized streamwise coordinate in the transition zone, and λ is a measure of the extent of the transition region; that is

$$\lambda = (x)_{\Gamma=3/4} - (x)_{\Gamma=1/4} \quad (7.83)$$

In the present analysis the transition extent, $x_{t,f} - x_{t,i}$ (see Section 7.5.4) is first calculated; next, the intermittency function is determined such that $\Gamma = 0.9999$ at $x = x_{t,f}$.

For low speed transition, Dhawan and Narasimha show that all transition regions may be correlated to form a universal intermittency distribution. Potter and Whitfield (ref. 63) have shown that similarity exists in the transition process for subsonic, supersonic and hypersonic flows. Although the effect of pressure gradients on the intermittency distribution has not been studied in detail, it is believed that the distribution will be affected primarily in the region of the initial spot generation.

The intermittency distribution across the layer at a given streamwise location in the transition region is a function of the shape of the turbulent spots. In reference 73 it is shown that the spots have a nearly constant cross sectional area close to the surface. The intermittency distributions in the transverse direction (y-direction) are similar to those observed by Corrsin and Kistler (ref. 76) for fully developed turbulent boundary layers (see ref. 77). Corrsin and Kistler found that the transverse intermittency varied from a maximum of unity near the wall to a near zero value at the outer edge of the layer. The transverse intermittency distribution is of secondary importance in relation to the streamwise distribution in determining the mean profiles and wall fluxes. In the present analysis the only intermittency distribution applied in the transverse direction (y-direction) is that of Klebanoff (ref. 36) in the outer layer as applied to the fully developed turbulent layer; that is, equation (7.68).

7.5.4 Transition Extent

The assumption of a universal intermittency distribution implies that the transition zone length (transition extent) can be expressed as a function of the transition Reynolds number, $u_e^* x_{t,i}^* / \nu_e^*$. In reference 75 it is shown, for the transition data considered, that the data are represented on the average by the equation

$$Re_{\Delta x_t} = \bar{\alpha} \bar{Re}_{x_{t,i}}^{\bar{\beta}} \quad (7.84)$$

where $\Delta x_t = x_{t,f}^* - x_{t,i}^*$. The coefficients $\bar{\alpha}$ and $\bar{\beta}$ are found to assume values of 5.0 and 0.8, respectively. The location of the completion of transition, $x_{t,f}^*$ can then be obtained directly from equation (7.84) as follows:

$$x_{t,f}^* = x_{t,i}^* + \alpha Re^{*-1} (Re_{x_{t,i}})^{\bar{\beta}} \quad (7.85)$$

where Re^* is the local unit Reynolds number, u_e^* / ν_e^* . Morkovin (ref. 9) found that only about 50 percent of the experimental data he considered could be fitted to the low speed universal curve of Dhawan and Narasimha; that is to equation (7.84). This was to be expected, since the data considered in reference 75 covered only a very limited Mach number range.

Potter and Whitfield (ref. 63) measured the extent of the transition zone over a rather broad Mach number range ($3 \leq M_\infty \leq 5$, $M_\infty = 8$). They observed that the transition region, when defined in terms of $Re_{\Delta x_t}$ is basically independent of the unit Reynolds number and leading edge geometry; that is

$$Re_{\Delta x_t} = \Omega_3(Re_{x_{t,i}}, M_\infty) \quad (7.86)$$

They noted (ref. 63) that the extent of the transition region increased with increasing transition Reynolds number over the Mach number range $0 \leq M_\infty \leq 8$ for adiabatic walls. The extent of the transition region was also observed to increase with increasing Mach numbers for a fixed transition Reynolds number.

In the present analysis, due to the lack of general correlations for the extent of transition this quantity will be obtained directly from the experimental data unless otherwise noted. In particular, if heat transfer data are available the transition zone will be assumed to lie between the initial deviation from the laminar heat transfer distribution and the final peak heating location. The transition region defined on the basis of the Stanton number distribution is presented in figure 7. The design engineer does not have the advantage of experimental data which were obtained under the actual flight conditions. Consequently, the most probable location of transition would be obtained from a correlation such as presented in equation (7.79) and (7.80). The extent of transition could then be obtained from equation (7.85) or an approximate relation such as follows:

$$\frac{Re_{x_{t,f}}}{Re_{x_{t,i}}} \cong 2 \quad (7.87)$$

Since the main objective of the design engineer is to obtain estimates of the heat protection requirements or viscous drag, for example, the errors involved in using equation (7.87) would be negligible for a full

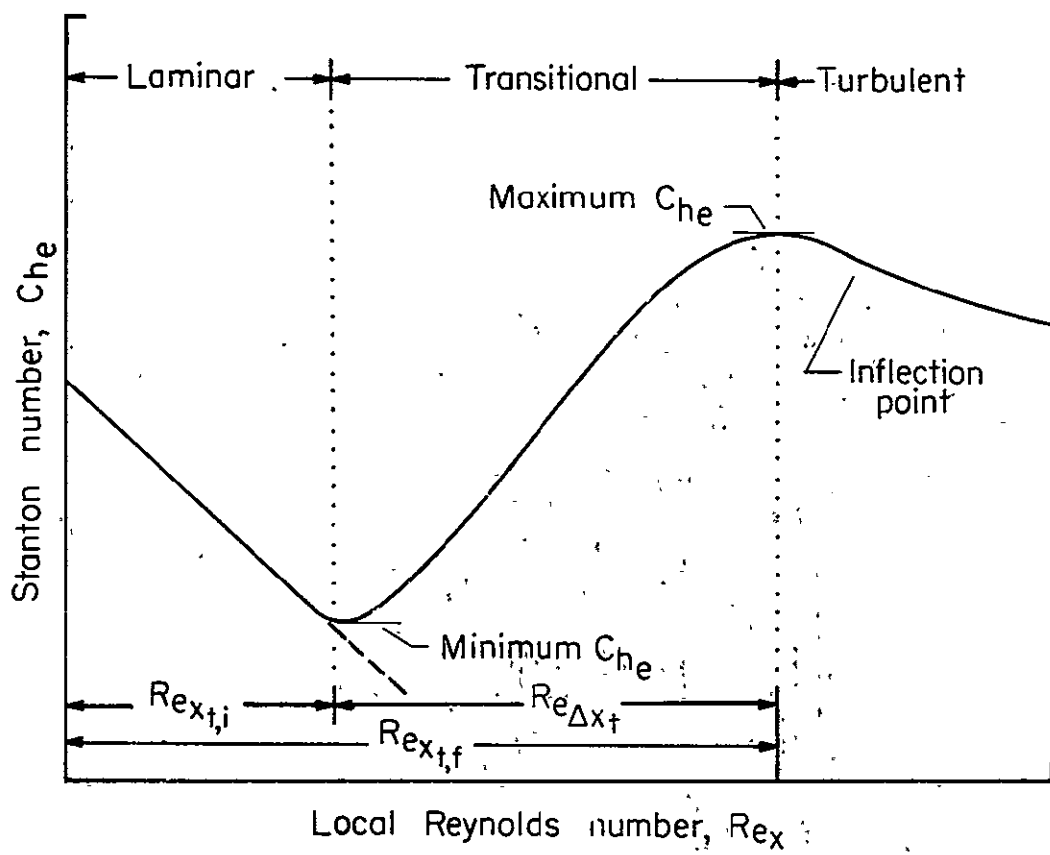


Figure 7.- Transition extent definition.

scale vehicle. However, inaccurate estimates of the transition location, $x_{t,i}$ could lead to significant errors.

7.6 Boundary Layer Parameters

Certain boundary layer parameters are of interest to the design engineer as well as to those interested in the general development of the boundary layer for arbitrary boundary conditions. A number of these parameters, which are used in chapter IX, are presented in this section for the physical plane as well as for the transformed plane where meaningful.

7.6.1 Displacement Thickness

The displacement thickness is a measure of the distance by which the external streamlines are shifted because of the development of the viscous boundary layer. If in the problem under consideration interaction is important, the displacement thickness may be used to determine a new effective body (ref. 15). The boundary layer displacement thickness for compressible flows is defined as

$$\bar{\delta}^* = \int_0^{y_e} t_j \left(1 - \frac{\rho u}{\rho_e u_e} \right) dy \quad (7.88)$$

where $\bar{\delta}^*$ is defined as the nondimensional displacement thickness, δ^*/L^* . In the transformed plane the nondimensional displacement thickness becomes

$$\bar{\delta}^* = \frac{\omega \sqrt{2\xi}}{\rho_e u_e r_0^j} \int_0^{\eta_e} (\Theta - F) d\eta \quad (7.89)$$

It should be noted that the definition of $\overline{\delta^*}$ for axisymmetric flows with transverse curvature is not the same as the definition of the nondimensional displacement thickness for two-dimensional flows, $\overline{\delta^*}_{2D}$. The displacement thickness with transverse curvature is related to its two-dimensional counterpart by the following relation (ref. 78)

$$\frac{\overline{\delta^*}}{r_o} = -1 + \sqrt{1 + \frac{2\overline{\delta^*}_{2D}}{r_o}} \quad (7.90)$$

The incompressible displacement thickness used in the outer region model for the eddy viscosity is presented in equation (7.66) and (7.77) for the real and transformed planes, respectively.

7.6.2 Momentum Thickness

The momentum thickness is used in a number of solution techniques as well as in current transition correlations. The nondimensional momentum thickness for the physical plane is defined as follows:

$$\overline{\theta} = \int_0^{y_e} t^j \frac{\rho u}{\rho_e u_e} \left(1 - \frac{u}{u_e}\right) dy \quad (7.91)$$

The nondimensional momentum thickness in the transformed plane may then be expressed as follows:

$$\overline{\theta} = \frac{\omega \sqrt{2\xi}}{\rho_e u_e r_o^j} \int_0^{\eta_e} F(1 - F) d\eta \quad (7.92)$$

7.6.3 Shear Stress

The viscous drag of a body moving through a fluid is dependent upon the shear stress at the wall. For turbulent boundary layers the shear stress distribution across the layer is also an important parameter. The total nondimensional shear stress may be divided into two components, laminar and turbulent; that is

$$\tau_T = \tau_l + \tau_t \quad (7.93)$$

or, in terms of the current notation

$$\tau_T = \mu \bar{\epsilon} \frac{\partial u}{\partial y} \quad (7.94)$$

The nondimensional total shear stress, τ_T is defined as

$$\tau_T = \tau_T^* / \left(\frac{\mu_{ref}^* u_{ref}^*}{L^*} \right) \quad (7.95)$$

Equation (7.95) becomes in the transformed plane

$$\tau_T = \frac{\rho_e \mu_e u_{er0}^{2j} \bar{\epsilon}}{\omega \sqrt{2\xi}} \left(\frac{\partial F}{\partial \eta} \right) \quad (7.96)$$

where $\bar{\epsilon}$ is defined in equation (7.15).

As the wall is approached, τ_T approaches τ_l and equation (7.96) becomes at the wall

$$\tau_w = \frac{\rho_e \mu_e u_{er0}^{2j}}{\omega \sqrt{2\xi}} \left(\eta \frac{\partial F}{\partial \eta} \right)_w \quad (7.97)$$

7.6.4 Skin Friction Coefficient

The skin friction coefficient is usually of more interest to the design engineer than the actual magnitude of the shear stress. The friction coefficient is defined as

$$\bar{C}_{f_e} = \tau_T^* / \left(\frac{1}{2} \rho_e^* u_e^{*2} \right) \quad (7.98)$$

which becomes in the nondimensional physical plane

$$\bar{C}_{f_e} = \frac{2\omega^2 \tau_T}{\rho_e u_e^2} \quad (7.99)$$

or

$$\bar{C}_{f_e} = \frac{2\omega^2 \mu \bar{\epsilon}}{\rho_e u_e^2} \left(\frac{\partial u}{\partial y} \right) \quad (7.100)$$

In the transformed plane equation (7.100) becomes

$$\bar{C}_{f_e} = \frac{2\omega \mu_{er0}^j t^j \bar{\epsilon}}{\sqrt{2\xi}} \left(\frac{\partial F}{\partial \eta} \right) \quad (7.101)$$

or, when evaluated at the wall

$$C_{f_e} = \frac{2\omega \mu_{er0}^j}{\sqrt{2\xi}} \left(l \frac{\partial F}{\partial \eta} \right)_w \quad (7.102)$$

7.6.5 Heat Transfer

The heat transfer between the boundary layer and the wall is required for aerodynamic heating analysis. The heat transfer at the wall is related to the temperature gradient at the wall in the dimensional physical plane through the following equation:

$$q_w^* = - \left(K_l^* \frac{\partial T^*}{\partial y^*} \right)_w \quad (7.103)$$

or in nondimensional form as

$$q_w = - \left(\frac{\mu}{\sigma} \frac{\partial T}{\partial y} \right)_w \quad (7.104)$$

where

$$q_w = q_w^* / \left(\frac{\mu_{ref}^* u_{ref}^{*2}}{L^*} \right) \quad (7.105)$$

Equation (7.104) becomes in the transformed plane

$$q_w = - \frac{\rho_e \mu_e u_e T_e r_o^j}{\omega \sqrt{2\xi} \sigma} \left(\eta \frac{\partial \Theta}{\partial \eta} \right)_w \quad (7.106)$$

7.6.6 Heat Transfer Coefficient

The heat transfer coefficient is defined by the following relation:

$$h^* = q_w^* / (T_w^* - T_{aw}^*) \quad (7.107)$$

where T_{aw}^* denotes the dimensional adiabatic wall temperature. In the present analysis the adiabatic wall temperature is defined as

$$T_{aw}^* = r_F(T_t^* - T_e^*) + T_e^* \quad (7.108)$$

Equation (7.107) can be written in nondimensional form as follows:

$$h = \frac{q_w}{T_w - T_{aw}} \quad (7.109)$$

where the nondimensional heat transfer coefficient h is defined as

$$h = h^* \left/ \left(\frac{C_p^* \mu_{ref}^*}{L^*} \right) \right. \quad (7.110)$$

The recovery factor r_F used in equation (7.108) has the following form

$$r_F = \sqrt{\sigma} [1 + (\sigma^{-1/6} - 1)F] \quad (7.111)$$

This relation was developed by the author and is based on the concept that the flow within the turbulent spot has the same structure as that of the fully turbulent region of the boundary layer. It can be seen from equation (7.111) that the recovery factor assumes the accepted mean values for pure laminar or fully turbulent flows of $\sigma^{1/2}$ and $\sigma^{1/3}$, respectively. Within the transition region the recovery factor is a function of the turbulent spot distribution through the intermittency factor, F . (See equation (7.81).)

7.6.7 Stanton Number

A convenient nondimensional parameter often used in the literature to describe the heat transfer at the wall is the Stanton number which is defined as follows:

$$C_{h_e} = h^*/(c_p^* u_e^*) \quad (7.112)$$

7.6.8 Friction Velocity

The velocity scale most often used for turbulent flows is the friction velocity. This important parameter is defined as

$$u_\tau^* = \sqrt{\frac{\tau_w^*}{\rho^*}} \quad (7.113)$$

which becomes in the transformed plane

$$u_\tau = \sqrt{\frac{\omega u_e^2 u_{e0}^2}{\sqrt{2\xi}} \left(l \frac{\partial F}{\partial \eta} \right)_w \Theta} \quad (7.114)$$

where

$$u_\tau = u_\tau^*/u_{ref}^* \quad (7.115)$$

7.6.9 Law of Wall Coordinates

The law-of-the-wall coordinates used in turbulent flow (see eqs. (7.48) and (7.49)) are defined in the physical plane as

$$y^+ = y^* u_\tau^*/\nu^* \quad (7.116a)$$

and

$$u^+ = u^*/u_T^* \quad (7.116b)$$

Equations (7.116) may be written in the transformed variables as

$$y^+ = \frac{\rho_e u_T Y}{\omega \mu_e l \Theta^2} \quad (7.117a)$$

and

$$u^+ = F \left[\frac{\omega \mu_e r_o^j}{\sqrt{2\xi}} \left(l \frac{\partial F}{\partial \eta} \right)_w \Theta \right]^{-1/2} \quad (7.117b)$$

7.6.10 Defect Law Coordinates

The defect law coordinates used in turbulent flow (see eq. (7.50)) are y/δ and \tilde{u} . The coordinate \tilde{u} is defined as follows:

$$\tilde{u} = (u_e^* - u^*)/u_T^* \quad (7.118)$$

or

$$\tilde{u} = u_e(1 - F)/u_T \quad (7.119)$$

7.7 Pitot Pressure Profiles

The total pressure is one of the mean profile values that can be measured directly in experimental studies. Consequently, it is advantageous to calculate the total pressure distribution across the layer for comparison to experimental data when available. The total pressure distribution is often encountered in the experimental

literature in one of two forms; (1) the local isentropic total pressure distribution referenced to the isentropic value of the total pressure at the boundary-layer edge (the term isentropic as used here means that the flow is locally brought to rest isentropically), and (2) the actual pitot tube measurement of the total pressure referenced to the pitot tube value at the edge of the boundary layer. For subsonic flows the two methods are identical; however, for supersonic flows caution must be exercised in interpreting the experimental results.

If the static pressure is constant across the boundary layer, the local isentropic total pressure referenced to the isentropic value at the edge of the layer may be expressed as

$$\frac{P_t}{P_{t_e}} = \left[\frac{2 + (\gamma - 1)M^2}{2 + (\gamma - 1)M_e^2} \right]^{\gamma/\gamma-1} \quad (7.120)$$

The local Mach number, M , may be expressed in terms of the mean temperature and velocity profiles as follows:

$$M = \frac{u_e}{\sqrt{(\gamma - 1)T_e}} \quad (7.121)$$

which becomes at the outer edge

$$M_e = \frac{u_e}{\sqrt{(\gamma - 1)T_e}} \quad (7.122)$$

In the case of subsonic flows the experimental profiles can be directly compared to the distribution obtained from equation (7.120);

however, for supersonic flows it is necessary to divide the boundary layer into a subsonic and a supersonic region. The boundary separating these two regions occurs where the local Mach number is unity and is obtained from equation (7.121). In the subsonic region of the boundary layer the pitot tube measures the local isentropic total pressure; however, it is usually referenced to the measured pitot value at the edge of the boundary layer where the flow is supersonic. Then the correct expression for the subsonic region becomes

$$\frac{P_{t_m}}{P_{t_{m_e}}} = \left[\frac{2 + (\gamma - 1)M^2}{(\gamma + 1)M_e^2} \right]^{\gamma/\gamma-1} \left[\frac{2\gamma M_e^2 - (\gamma - 1)}{\gamma + 1} \right]^{1/\gamma-1} \quad (7.123)$$

In the supersonic region of the layer the ratio can be written as

$$\frac{P_{t_m}}{P_{t_{m_e}}} = \left(\frac{M}{M_e} \right)^{2\gamma/\gamma-1} \left[\frac{2\gamma M^2 - (\gamma - 1)}{2\gamma M_e^2 - (\gamma - 1)} \right]^{-1/\gamma-1} \quad (7.124)$$

In the present analysis the total pressure distributions will be obtained from equations (7.123) and (7.124) for the subsonic region and supersonic region of the boundary layer, respectively. The boundary between the two regions will be obtained from equation (7.121); that is, where the local Mach number is unity.

7.8 Exterior Flow

The following quantities will be specified in order to describe the exterior flow and fluid properties

$$P_{t,\infty}^*, T_{t,\infty}^*, M_\infty, P_e^*, \sigma, \sigma_t, \gamma, C_p^*, S^*$$

Reference Values

The reference values are evaluated for an isentropic, perfect gas as follows:

$$u_{\text{ref}}^* = M_{\infty} \sqrt{\frac{(\gamma - 1) C_p^* T_{t,\infty}^*}{1 + \left(\frac{\gamma - 1}{2}\right) M_{\infty}^2}} \quad (7.125)$$

$$\rho_{\text{ref}}^* = \frac{\gamma P_{t,\infty}^*}{(\gamma - 1) C_p^* T_{t,\infty}^*} \left(1 + \frac{\gamma - 1}{2} M_{\infty}^2\right)^{-1/\gamma-1} \quad (7.126)$$

$$T_{\text{ref}}^* = u_{\text{ref}}^{*2} / C_p^* \quad (7.127)$$

$$\mu_{\text{ref}}^* = \frac{2.270 (T_{\text{ref}}^*)^{3/2} \times 10^{-8}}{T_{\text{ref}}^* + S^*} \quad (\text{air only}) \quad (7.128)$$

The reference values are independent of body geometry and are used to form the dimensionless variables (see eqs. (7.20)).

Edge Values

The inviscid pressure distribution must be specified for a given flow geometry in order to obtain a solution of the governing differential equations (eqs. (7.38) to (7.40)). This distribution can be obtained from either experimental data or from an exact solution of the full inviscid Euler equations. In the case of supersonic flows where shock wave curvature may have a first order effect on the boundary layer structure, the effect of variable entropy should be taken into consideration (see Section 7.9). The total pressure behind

the shock wave, P_{t_s} can be obtained from the oblique shock relations (ref. 79) provided the shock wave angle, $\theta_s(r_s, z_s)$ is specified; that is

$$P_{t_s} = P_{t,\infty} \left\{ \frac{(\gamma + 1)M_\infty^2 \sin^2 \theta_s(r_s, z_s)}{(\gamma - 1)M_\infty^2 \sin^2 \theta_s(r_s, z_s) + 2} \right\}^{\frac{\gamma}{\gamma - 1}} \left\{ \frac{\gamma + 1}{2\gamma M_\infty^2 \sin^2 \theta_s(r_s, z_s) - (\gamma - 1)} \right\}^{\frac{1}{\gamma - 1}} \quad (7.129)$$

where P_{t_s} is the dimensionless total pressure behind the shock wave evaluated locally at the shock wave coordinate (r_s, z_s) . For cases where the effect of variable entropy is either neglected or negligible, P_{t_s} is evaluated at $r_s = 0$ (see fig. 1) and is invariant along the streamline $\psi_e(o, x)$. For cases where the flow is either subsonic everywhere or supersonic shock free flow, $P_{t_s} = P_{t,\infty}$.

The edge conditions can then be calculated from the specified static pressure distribution and the known value of P_{t_s} as follows

$$M_e = \left\{ \frac{2}{\gamma - 1} \left[\left(\frac{P_{t_s}}{P_e} \right)^{\frac{\gamma - 1}{\gamma}} - 1 \right] \right\}^{1/2} \quad (7.130)$$

$$T_e = T_{t,\infty} \left(1 + \frac{\gamma - 1}{2} M_e^2 \right)^{-1} \quad (7.131)$$

$$u_e = M_e \sqrt{(\gamma - 1)T_e} \quad (7.132)$$

$$\rho_e = \left(\frac{\gamma}{\gamma - 1} \right) \frac{P_e}{T_e} \quad (7.133)$$

and

$$\mu_e = (T_e)^{3/2} \left(\frac{1 + S}{T_e + S} \right) \text{ (air only)} \quad (7.134)$$

where $S = S^*/T_{ref}^*$.

7.9 Variable Entropy

One of the important factors that should be taken into consideration for slender blunted or sharp-tipped bodies in supersonic flow is the effect of the variable entropy introduced by shock wave curvature on the boundary layer characteristics. The basic problems associated with incorporating variable entropy into the boundary layer solution are (1) to obtain the entropy distribution along the boundary layer edge as a function of x , and (2) to develop an iterative solution technique with which this distribution can be efficiently included in the solution of the governing boundary layer equations (eqs. (7.38) to (7.40)). In the present analysis the shock wave coordinates and inviscid pressure distribution are obtained from an exact inviscid flow field solution. The boundary layer equations are then solved by the method presented in chapter VIII. At each x -solution station a mass balance is obtained between the total mass contained in the boundary layer at the particular x -station and the mass passing through a streamtube of radius r_s^* (see fig. 1). From this the entropy distribution as a function of x can be obtained. The resulting total pressure at each x -station is stored for future use in the digital computer. The actual equations and procedures

utilized in the process are discussed in the remaining portion of this section.

The shock wave coordinates and inviscid pressure distribution can be directly obtained from the solution developed by Iomax and Inouye (ref. 80) for either sharp-tipped or blunt axisymmetric or planar geometries. The mass balance equation which equates the mass of the fluid passing through a streamtube of radius r_s^* (see fig. 1) to the total mass entrained in the boundary layer at a given x-station can be expressed for either axisymmetric or planar flows as follows

$$\rho_{\text{ref}}^* u_{\text{ref}}^* r_s^{j+1} = (j+1) \int_0^{y_e^*} \rho^* u^* r_0^j dy^* \quad (7.135)$$

or in terms of the dimensionless variables as

$$r_s^{j+1} = (j+1) \rho_e u_e \int_0^{y_e} \frac{F}{\Theta} r_0^j dy \quad (7.136)$$

Equation (7.136) can then be expressed in the transformed plane as follows:

$$r_s = \left[(j+1) \omega \sqrt{2\xi} \int_0^{\eta_e} F d\eta \right]^{\frac{1}{j+1}} \quad (7.137)$$

Equation (7.137) is locally solved for r_s at each x-station along the body surface. The shock wave angle, (r_s, z_s) is then obtained from the known shock wave coordinates at the shock wave streamline intersection point, (r_s, z_s) . The total pressure behind

the shock wave on the streamline $\psi_e(r_s, z_s)$ is then evaluated from equation (7.129). These values are stored in the computer for each x-station. This process is continued until the solution at the final x-station (maximum x-value) is completed. The boundary layer solution is then known for the condition of constant entropy. This is called the first iteration and if variable entropy is to be neglected it represents the final solution. In order to include variable entropy effects the solution is then restarted at $\xi = 0$ ($x = 0$) and the solution recalculated using the previously stored values of P_{tS} to calculate the new local values of M_e , T_e , u_e , ρ_e , and μ_e (see eqs. (7.130) to (7.134)); this is defined as the second iteration. It should be noted that P_{tS} is independent of ξ for the first iteration cycle; however, for subsequent iteration cycles P_{tS} is a function of ξ . The new P_{tS} values for the $i + 1$ iteration are calculated during the i iteration. The P_e distribution as a function of x is an invariant for all iteration cycles.

The convergence criteria used at each x-station is as follows:

$$|u_{e,i+1} - u_{e,i}| \leq Q \quad (7.138)$$

where i is the iteration index and Q denotes the specified convergence requirement. For engineering calculations three iterations are generally sufficient for a one percent or smaller change in u_e at each x-station; that is, for $Q = 0.01$.

VIII. NUMERICAL SOLUTION OF THE GOVERNING EQUATIONS

The governing equations for the compressible laminar, transitional, and turbulent boundary layers form a fifth-order system. Three of the equations are nonlinear partial differential equations (see eqs. (7.38) to 7.40)) and the remaining two are algebraic relations (see eqs. (7.31) and (7.32)). The most important feature of this system is that it is parabolic and, as such, can be numerically integrated in a step-by-step procedure along the body surface. In order to cast the equations into a form in which the step-by-step procedure can be efficiently utilized, the derivatives with respect to ξ and η are replaced by finite difference quotients.

The method of linearization and solution used in the present analysis closely parallels that of Flügge-Lotz and Blottner (ref. 15) with modifications suggested by Davis and Flügge-Lotz (ref. 16) to improve the accuracy. These modifications involve the use of three-point implicit differences in the ξ -direction which produce truncation errors of order $(\Delta\xi_1 \Delta\xi_2)$ rather than (Δx) as in reference 15. The primary difference between the present development and that of reference 16 is that the solution is obtained in the transformed plane for arbitrary grid-point spacing in the ξ -direction and for a spacing in the η -direction such that the spacing between any two successive grid points is a constant. To the author's knowledge, this numerical solution technique has not been previously applied to either transitional or turbulent boundary-layer flows.

The three-point implicit difference quotients are first developed for the particular grid-point spacing utilized herein. These results are then substituted into the governing equations for the conservation of momentum and energy in order to obtain a system of difference equations. The most important characteristic of the system of difference equations, other than the fact that they are linear, is that the transformed normal component of velocity, V does not appear explicitly as an unknown at the solution station. Consequently, the $N-1$ linear difference equations can be simultaneously solved to yield the $N-1$ unknown values of F and Θ . Having obtained the $N-1$ values of F and Θ , the $N-1$ values of V can be obtained by a numerical integration of the continuity equation. Some details of the implicit method have been purposely omitted; for these the reader is referred to Flügge-Lotz and Blottner (ref. 15). The reader interested in a thorough discussion of the various schemes that could be utilized to obtain either pure difference equations, as in the present paper, or difference-differential equations such as used by Smith and Clutter (refs. 81 and 82) is referred to Davis and Flügge-Lotz (ref. 16). The advantages and disadvantages of implicit differences in relation to explicit differences are discussed by Flügge-Lotz and Blottner (ref. 15) and will not be discussed herein.

8.1 The Implicit Solution Technique

8.1.1 Finite Difference Mesh Model

It has been shown for laminar boundary layers that equally spaced grid points can be utilized in the normal coordinate direction (for example, see refs. 14 and 15). However, for transitional and turbulent boundary layers, the use of equally spaced grid points is not practical for the present solution method. As previously mentioned in Section 7.4.1, the viscous sublayer thickness is on the order of 0.0018 to 0.018. In order to obtain a convergent (valid) solution to the governing equations, it is necessary to have a number of grid points within the viscous sublayer. The viscous sublayer problem is discussed in detail in Section 9.1 where the errors resulting from improper grid-point spacing in the wall region are demonstrated with a numerical example. Since a number of grid points must be positioned within this relatively thin layer in relation to the total thickness, δ , one cannot afford to utilize equally spaced grid points from the viewpoint of computer storage requirements and processing time per test case. For example, if the total thickness of the η -strip was 100 for a particular problem of interest, then the requirement of equally spaced grid points would mean on the order of 1,000 points in relation to 200 for variable spacing. In order to avoid the necessity of using an inefficient number of grid points, a variable grid-point scheme must be utilized.

The grid-point spacing in the η -direction used in the present analysis assumes that the ratio of any two successive steps is a

constant, that is, the successive $\Delta\eta_1$, form a geometric progression. There are any number of schemes that could be employed to distribute the points across the η -strip; however, the present method has been found to be flexible and of utility.

The desirability of having variable grid-point spacing in the ξ -coordinate has previously been mentioned in Section 7.3. The importance becomes clearly apparent for problems in which either the rate of change of the edge conditions is large or discontinuous boundary conditions occur, or in the transition region where the mean profiles are changing rapidly. A good example of the former case would be a slender, blunted cone in supersonic flow. Variable grid-point spacing in the ξ -direction could be utilized by having very small steps in the stagnation region where the pressure gradient is severe (favorable) and in some downstream region where transitional flow exists. A good example of the case of discontinuous boundary conditions would be a sharp-tipped cone with a porous insert at some downstream station through which a gas is being injected into the boundary layer. Relatively large step sizes could be utilized upstream of the ramp injection; however, small steps must be used in the region of the ramp injection. Downstream of the porous region, as the flow relaxes, larger step sizes could be used. It is very important that small grid-point spacing be utilized in the transition region where the mean profiles are a strong function of the intermittency distribution. Typical examples of the above-mentioned cases are shown schematically in figure 8. Therefore, because of the requirements imposed by a

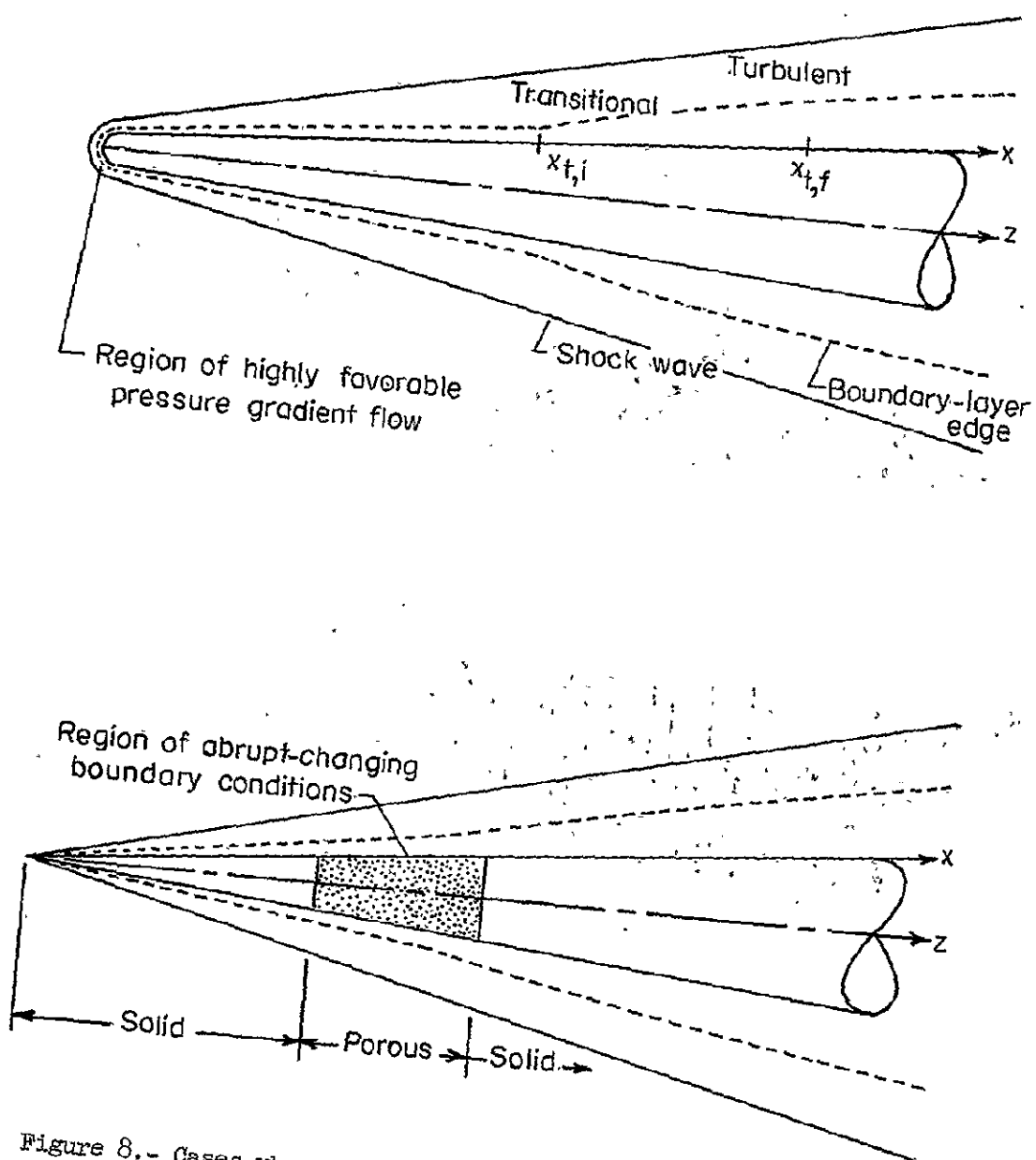


Figure 8.- Cases where variable grid-point spacing is required.

completely general problem where the possibility exists for abrupt or rapidly changing edge conditions and boundary values, as well as the particular problem associated with the transitional and turbulent boundary layers, variable grid-point spacing is utilized in the present technique in both the ξ and η directions. The grid-point spacing in the ξ -direction is completely arbitrary. The grid-point spacing in the η -direction is such that the $\Delta\eta_i$ ($i = 1, 2, \dots, N$) form a geometric progression.

In constructing the difference quotients, the sketch of the grid-point distribution presented in figure 9 is useful for reference. The dependent variables F and Θ are assumed known at each of the N grid points along the $m-1$ and m stations, but unknown at station $m+1$. The $\Delta\xi_1$ and $\Delta\xi_2$ values, not specified to be equal are obtained from the specified x -values (x_{m-1}, x_m, x_{m+1}) and equation (7.33a). The relationship between the $\Delta\eta_i$ for the chosen grid-point spacing is given by the following equation:

$$\Delta\eta_i = (K)^{i-1} \Delta\eta_1 \quad (8.1)$$

In equation (8.1), K is the ratio of any two successive steps, $\Delta\eta_1$ is the spacing between the second grid point and the wall (note that the first grid point is at the wall), and N denotes the total number of grid points across the chosen η -strip. The geometric progression spacing of the grid points defined by equation (3.1) is but one of any number of possible schemes. This particular approach has been found to be satisfactory by a number of investigators; for example, Bushnell and

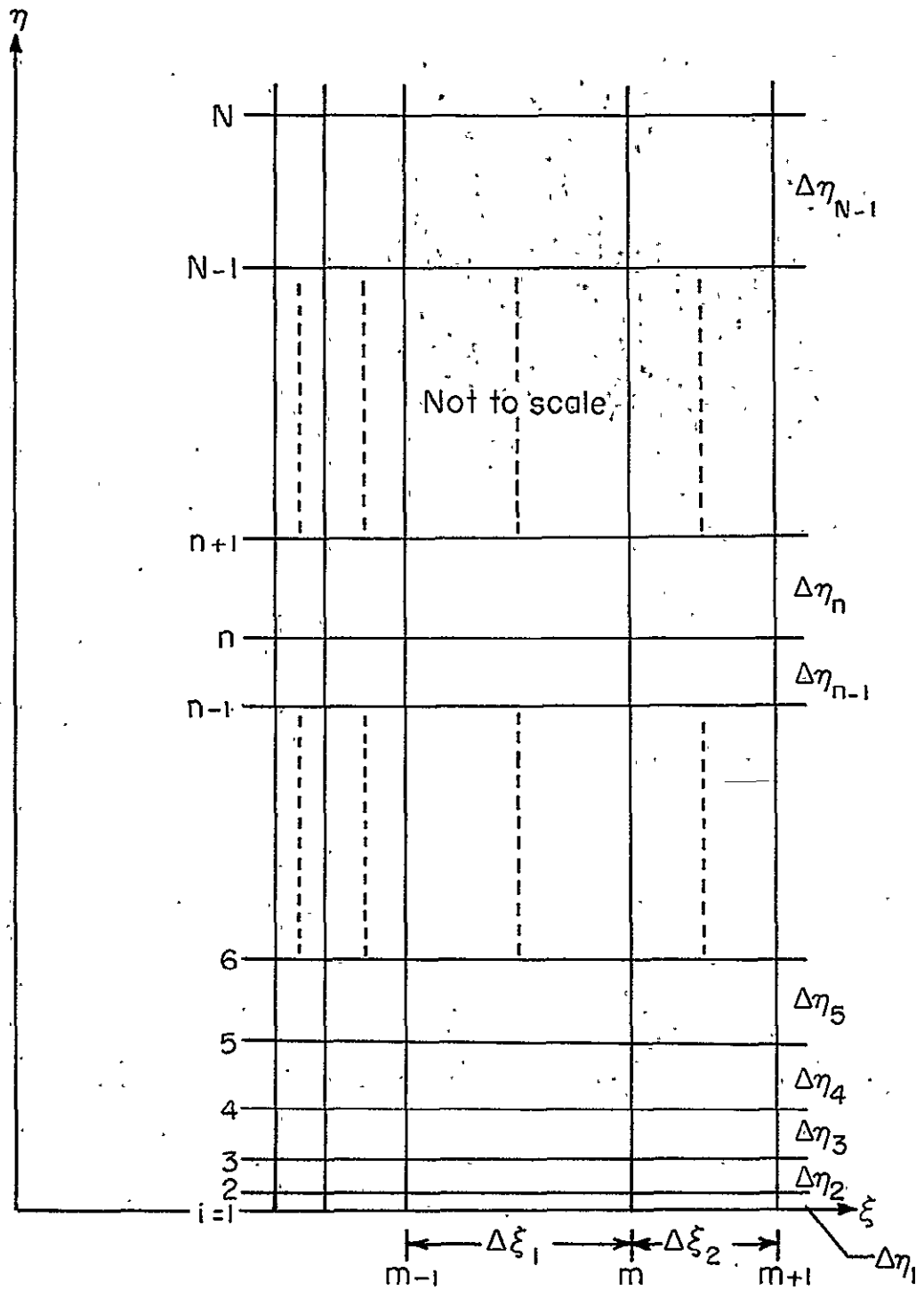


Figure 9.- Finite difference grid model.

Beckwith (ref. 31) and Cebeci (ref. 78). The total thickness of the η -strip can then be expressed as follows:

$$\eta_N = \Delta\eta_1 \left[\frac{1 - (K)^{N-1}}{1 - K} \right] \quad (K \neq 1) \quad (8.2)$$

Another particularly important and useful relation is

$$K = \frac{\eta_1 - \Delta\eta_1}{\eta_1 - \Delta\eta_1} \quad (8.3)$$

The spacing of the grid points is completely determined for a specified set of η_N , K , and N values. The selection of the optimum K and N values for a specified η_N depends upon the particular problem under consideration. The main objective in the selection is to obtain the minimum number of grid points with which a convergent solution may be obtained. That is, in order to minimize the computer processing time per test case, it is necessary to minimize the total number of grid points across the boundary layer and to maximize the spacing between the solution stations along the surface. The laminar layer presents no problem since a K value of unity is acceptable; however, for transitional and turbulent layers, the value of K will be a number slightly greater than unity, say 1.04.

8.1.2 Finite Difference Relations

Three-point implicit difference relations are used to reduce the transformed momentum and energy equations (eqs. (7.39) and (7.40)) to finite difference form. As previously mentioned in Section 8.1.1, it

is assumed that all data are known at the stations $m-1$ and m (see fig. 9). We then wish to obtain the unknown quantities at the grid points for the $m+1$ station. The notations G and H are utilized in the following development to represent any typical variable.

Taylor series expansions are first written about the unknown grid point $(m+1, n)$ in the ξ -direction as follows:

$$G_{m,n} = G_{m+1,n} - \Delta \xi_2 (G_{\xi})_{m+1,n} + \frac{\Delta \xi_2^2}{2} (G_{\xi\xi})_{m+1,n} - \frac{\Delta \xi_2^3}{6} (G_{\xi\xi\xi})_{m+1,n} + \dots \quad (8.4a)$$

and

$$\begin{aligned} G_{m-1,n} = G_{m+1,n} - (\Delta \xi_1 + \Delta \xi_2) (G_{\xi})_{m+1,n} + \frac{(\Delta \xi_1 + \Delta \xi_2)^2}{2} (G_{\xi\xi})_{m+1,n} \\ - \frac{(\Delta \xi_1 + \Delta \xi_2)^3}{6} (G_{\xi\xi\xi})_{m+1,n} + \dots \end{aligned} \quad (8.4b)$$

where subscript notation has been utilized to denote differentiation;

that is, $G_{\xi} \equiv \left(\frac{\partial G}{\partial \xi} \right)$, etc.

Equations (8.4a) and (8.4b) can be solved to yield

$$\begin{aligned} \left(\frac{\partial G}{\partial \xi} \right)_{m+1,n} = \frac{X_1 G_{m+1,n} - X_2 G_{m,n} + X_3 G_{m-1,n}}{2 \Delta \xi_2} \\ + \frac{\Delta \xi_2 (\Delta \xi_1 + \Delta \xi_2)}{6} G_{\xi\xi\xi} + \dots \end{aligned} \quad (8.5)$$

and

$$G_{m+1,n} = X_4 G_{m,n} - X_5 G_{m-1,n} + \frac{\Delta \xi_1 \Delta \xi_2}{2} \left(1 + \frac{\Delta \xi_2}{\Delta \xi_1} \right) G_{\xi\xi} + \dots \quad (8.6)$$

The X_1, X_2, \dots, X_5 coefficients appearing in equations (8.5) and (8.6) are defined as follows:

$$X_1 = 2 \frac{\Delta \xi_1 + 2 \Delta \xi_2}{\Delta \xi_1 + \Delta \xi_2} \quad (8.7)$$

$$X_2 = 2 \frac{\Delta \xi_1 + \Delta \xi_2}{\Delta \xi_1} \quad (8.8)$$

$$X_3 = 2 \frac{\Delta \xi_1 \Delta \xi_2}{\Delta \xi_1 (\Delta \xi_1 + \Delta \xi_2)} \quad (8.9)$$

$$X_4 = \frac{\Delta \xi_1 + \Delta \xi_2}{\Delta \xi_1} \quad (8.10)$$

and

$$X_5 = \frac{\Delta \xi_2}{\Delta \xi_1} \quad (8.11)$$

Taylor series expansions are next written about the unknown grid point $(m+1, n)$ in the η -direction as follows:

$$\begin{aligned} G_{m+1, n+1} = G_{m+1, n} + \Delta \eta_n (G_\eta)_{m+1, n} + \frac{\Delta \eta_n^2}{2} (G_{\eta\eta})_{m+1, n} \\ + \frac{\Delta \eta_n^3}{6} (G_{\eta\eta\eta})_{m+1, n} + \dots \end{aligned} \quad (8.12a)$$

and

$$\begin{aligned}
G_{m+1,n-1} = G_{m+1,n} - \Delta\eta_{n-1}(G_{\eta\eta})_{m+1,n} + \frac{\Delta\eta_{n-1}^2}{2}(G_{\eta\eta\eta})_{m+1,n} \\
- \frac{\Delta\eta_{n-1}^3}{6}(G_{\eta\eta\eta\eta})_{m+1,n} + \dots
\end{aligned} \quad (8.12b)$$

Equations (8.12a) and (8.12b) can be solved to yield

$$\begin{aligned}
\left(\frac{\partial^2 G}{\partial \eta^2}\right)_{m+1,n} = Y_1 G_{m+1,n+1} - Y_2 G_{m+1,n} + Y_3 G_{m+1,n-1} \\
+ \frac{(\Delta\eta_{n-1} - \Delta\eta_n)}{3} G_{\eta\eta\eta} + \dots
\end{aligned} \quad (8.13)$$

and

$$\begin{aligned}
\left(\frac{\partial G}{\partial \eta}\right)_{m+1,n} = Y_4 G_{m+1,n+1} - Y_5 G_{m+1,n} - Y_6 G_{m+1,n-1} \\
- \frac{\Delta\eta_n \Delta\eta_{n-1}}{6} G_{\eta\eta\eta} + \dots
\end{aligned} \quad (8.14)$$

The Y_1, Y_2, \dots, Y_6 coefficients appearing in equations (8.13) and (8.14) are defined as follows:

$$Y_1 = \frac{2}{\Delta\eta_n(\Delta\eta_n + \Delta\eta_{n-1})} \quad (8.15)$$

$$Y_2 = \frac{2}{\Delta\eta_n \Delta\eta_{n-1}} \quad (8.16)$$

$$Y_3 = \frac{2}{\Delta\eta_{n-1}(\Delta\eta_n + \Delta\eta_{n-1})} \quad (8.17)$$

$$Y_4 = \frac{\Delta\eta_{n-1}}{\Delta\eta_n (\Delta\eta_n + \Delta\eta_{n-1})} \quad (8.18)$$

$$Y_5 = \frac{\Delta\eta_{n-1} - \Delta\eta_n}{\Delta\eta_n \Delta\eta_{n-1}} \quad (8.19)$$

and

$$Y_6 = \frac{\Delta\eta_n}{\Delta\eta_{n-1} (\Delta\eta_n + \Delta\eta_{n-1})} \quad (8.20)$$

For the case of equally spaced grid points in the ξ and η coordinates, equations (8.7) to (8.11) and (8.15) to (8.20) reduce to the following relations:

$$\left. \begin{aligned} X_1 &= 3 \\ X_2 &= 4 \\ X_3 &= 1 \\ X_4 &= 2 \\ X_5 &= 1 \end{aligned} \right\} \quad (8.21a)$$

and

$$\left. \begin{aligned} Y_1 &= \frac{1}{\Delta\eta^2} \\ Y_2 &= 2Y_1 \\ Y_3 &= Y_1 \\ Y_4 &= \frac{1}{(2 \Delta\eta)} \end{aligned} \right\} \quad (8.21b)$$

$$\left. \begin{aligned} Y_5 &= 0 \\ Y_6 &= Y_4 \end{aligned} \right\}$$

where $\Delta\xi$ and $\Delta\eta$ represent the spacing between the grid points in the ξ and η coordinates, respectively.

Equations (8.5), (8.6), (8.13), and (8.14) can then be written for constant grid-point spacing as follows:

$$\left(\frac{\partial G}{\partial \xi}\right)_{m+1,n} = \frac{3G_{m+1,n} - 4G_{m,n} + G_{m-1,n}}{2\Delta\xi} + \frac{\Delta\xi^2}{3} G_{\xi\xi\xi} + \dots \quad (8.22)$$

$$G_{m+1,n} = 2G_{m,n} - G_{m-1,n} + \Delta\xi^2 G_{\xi\xi} + \dots \quad (8.23)$$

$$\left(\frac{\partial^2 G}{\partial \eta^2}\right)_{m+1,n} = \frac{G_{m+1,n+1} - 2G_{m+1,n} + G_{m+1,n-1}}{\Delta\eta^2} - \frac{\Delta\eta^2}{12} G_{\eta\eta\eta\eta} + \dots \quad (8.24)$$

and

$$\left(\frac{\partial G}{\partial \eta}\right)_{m+1,n} = \frac{G_{m+1,n+1} - G_{m+1,n-1}}{2\Delta\eta} - \frac{\Delta\eta^2}{6} G_{\eta\eta\eta} + \dots \quad (8.25)$$

Equations (8.22) to (8.25) are recognized as the standard relations for equally spaced grid points. (See, for example, ref. 16.)

Quantities of the form $G\left(\frac{\partial G}{\partial \xi}\right)$ that appear in the governing equations must be linearized in order to obtain a system of linear

difference equations. Quantities of this type are linearized by utilizing equations (8.5) and (8.6); that is,

$$\begin{aligned} \left(G \frac{\partial G}{\partial \xi} \right)_{m+1,n} &= (X_4 G_{m,n} - X_5 G_{m-1,n}) (X_1 G_{m+1,n} - X_2 G_{m,n} + X_3 G_{m-1,n}) \\ &+ O(\Delta \xi_1 \Delta \xi_2) \end{aligned} \quad (8.26)$$

The procedure used to linearize nonlinear products such as $\left(\frac{\partial G}{\partial \eta} \right) \left(\frac{\partial H}{\partial \eta} \right)$ is the same as that used by Flügge-Lotz and Blöttner (ref. 15) and is as follows:

$$\begin{aligned} \left[\left(\frac{\partial G}{\partial \eta} \right) \left(\frac{\partial H}{\partial \eta} \right) \right]_{m+1,n} &= \left(\frac{\partial G}{\partial \eta} \right)_{m,n} \left(\frac{\partial H}{\partial \eta} \right)_{m+1,n} - \left(\frac{\partial G}{\partial \eta} \right)_{m,n} \left(\frac{\partial H}{\partial \eta} \right)_{m,n} \\ &+ \left(\frac{\partial H}{\partial \eta} \right)_{m,n} \left(\frac{\partial G}{\partial \eta} \right)_{m+1,n} \end{aligned} \quad (8.27)$$

where the terms $\left(\frac{\partial G}{\partial \eta} \right)_{m,n}$ and $\left(\frac{\partial H}{\partial \eta} \right)_{m,n}$ are evaluated from equation (8.14), but at the known station, m . Equating G to H in equation (8.27), the linearized form for quantities of the type $\left(\frac{\partial G}{\partial \eta} \right)^2$ is obtained; that is,

$$\left(\frac{\partial G}{\partial \eta} \right)_{m+1,n}^2 = \left(\frac{\partial G}{\partial \eta} \right)_{m,n} \left[2 \left(\frac{\partial G}{\partial \eta} \right)_{m+1,n} - \left(\frac{\partial G}{\partial \eta} \right)_{m,n} \right] \quad (8.28)$$

where $\left(\frac{\partial G}{\partial \eta} \right)_{m+1,n}$ is obtained from equation (8.14).

The preceding relations for the difference quotients produce linear difference equations when substituted into the governing

differential equations for the conservation of momentum (7.39) and energy (7.40). These linear difference equations may be written as follows:

$$\begin{aligned} A1_n F_{m+1,n-1} + B1_n F_{m+1,n} + C1_n F_{m+1,n+1} + D1_n \Theta_{m+1,n-1} \\ + E1_n \Theta_{m+1,n} + F1_n \Theta_{m+1,n+1} = G1_n \end{aligned} \quad (8.29)$$

$$\begin{aligned} A2_n F_{m+1,n-1} + B2_n F_{m+1,n} + C2_n F_{m+1,n+1} + D2_n \Theta_{m+1,n-1} \\ + E2_n \Theta_{m+1,n} + F2_n \Theta_{m+1,n+1} = G2_n \end{aligned} \quad (8.30)$$

The coefficients $A1_n, B1_n, \dots, G1_n, A2_n, \dots, G2_n$ are functions of quantities evaluated at stations m and $m-1$ and are therefore known. These coefficients are presented in the appendix.

8.1.3 Solution of Difference Equations

The proper boundary conditions to be used with the difference equations for the specific problem under consideration are specified in equations (7.45). The system contains exactly $2(N-1)$ mutually dependent equations for $2(N-1)$ unknowns since the boundary conditions are specified at the wall ($i = 1$, see fig. 9). This system of equations can then be simultaneously solved for the $2(N-1)$ unknowns at the $m+1$ station. The system is of a very special type, since a large number of the coefficients in the system are zero. The simultaneous solution technique has been discussed in detail by Flügge-Lotz and Blottner

(ref. 15). A discussion of the technique as applied to the incompressible laminar boundary-layer equations is also presented by Schlichting (ref. 2, pp. 181-184). (See, also, Richtmyer, ref. 83.)

8.1.4 Solution of Continuity Equation

It is important to notice that the transformed normal component of velocity, V does not appear as an unknown at station $m+1$ in the difference equations (eqs. (8.29) and (8.30)). This arises because of the way quantities of the type $V \left(\frac{\partial F}{\partial \eta} \right)$ are linearized (see eq. (8.26)). Consequently, equation (7.38) can be numerically solved for the $N-1$ unknown values of V at station $m+1$ once the values of F and Θ are known at station $m+1$. Equation (7.38) can be integrated to yield the following relation for V at the grid point $(m+1, n)$:

$$V_{m+1, n} = V_{m+1, 1} - \int_0^{\eta_n} \left(2\xi \frac{\partial F}{\partial \xi} + F \right) d\eta \quad (8.31)$$

where $V_{m+1, 1}$ represents the boundary condition at the wall and is defined in equation (7.47) as a function of the mass transfer at the wall, $(\rho^* v^*)_w$. The integral appearing in equation (8.31) can then be numerically integrated across the η -strip to obtain the $N-1$ values of V . In the present analysis the trapezoidal rule of integration was utilized. However, any sufficiently accurate numerical procedure could be used (see, for example, refs. 84 or 85).

8.1.5 Initial Profiles

Initial profiles for starting the finite difference scheme are required at two stations since three-point differences are utilized (see fig. 2). The initial profiles at the stagnation point or line for blunt bodies, or at $x = 0$ for sharp-tipped bodies, are obtained by an exact numerical solution of the similar boundary-layer equations. The equations are solved by a fourth-order Adams-Bashforth-Moulton fixed-step size integration method with a fourth-order Runge-Kutta technique (ref. 85) used to start the integration. The $N-1$ values of F , Θ , and V which are now known at the $N-1$ equally spaced grid points are numerically redistributed to $N-1$ grid points whose spacing is determined from equations (8.1) to (8.3) if a variable spacing is required. The second initial profile located at station m is assumed to be identical to the one located at station $m-1$. Any errors that might be incurred because of this assumption are minimized by using an extremely small $\Delta\xi$, that is, an initial step size in the physical plane on the order of $\Delta x = 1 \times 10^{-5}$. The solution at the unknown station, $m+1$, is then obtained by the finite difference method. One advantage of variable step size in the ξ -coordinate is clearly demonstrated for blunt body flows. Davis and Flügge-Lotz (ref. 16) found that from the standpoint of accuracy and computer processing time step sizes on the order of 0.005 in the physical plane were required. However, in the present solution, extremely small, equally spaced step sizes can be utilized in the stagnation region and then increased to more realistic values once the errors due to the starting procedure

have approached zero. Davis and Flügge-Lotz (ref. 16) were primarily interested in obtaining solutions for only a few nose radii downstream; consequently, equally spaced but sufficiently small grid-point spacing in the x-coordinate could be utilized. However, for engineering calculations where solutions may be required as far downstream as 1,000 or more nose radii, one cannot afford to use equally spaced grid points.

It is also advantageous to have the capability of starting the solution from experimentally measured profiles, especially in the case of turbulent flow. This capability has also been incorporated into the digital computer program used in the present analysis. This capability is extremely useful for cases where one cannot easily locate the origin of the boundary layer, for example, nozzle walls.

8.1.6 Evaluation of Wall Derivatives

The shear stress and heat transfer at the wall (eqs. (7.97) and (7.106)) are directly proportional to the gradient of F and θ evaluated at the wall, respectively. Using G to represent a general quantity, where $G_{m+1,1}$ is not specified to be zero, the four-point difference scheme used to evaluate derivatives at the wall is as follows:

$$\left(\frac{\partial G}{\partial \eta}\right)_{m+1,1} = Y_7 G_{m+1,1} + Y_8 G_{m+1,2} + Y_9 G_{m+1,3} + Y_{10} G_{m+1,4} \quad (8.32)$$

where the coefficients Y_7, \dots, Y_{10} are defined by the following equations:

$$Y_7 = - \frac{(1 + K + K^2)^2 [K(1 + K) - 1] + (1 + K)}{(1 + K)(1 + K + K^2)K^3 \Delta\eta_1} \quad (8.33a)$$

$$Y_8 = \frac{(1 + K + K^2)}{K^2 \Delta\eta_1} \quad (8.33b)$$

$$Y_9 = - \frac{(1 + K + K^2)}{(1 + K)K^3 \Delta\eta_1} \quad (8.33c)$$

and

$$Y_{10} = \frac{1}{(1 + K + K^2)K^3 \Delta\eta_1} \quad (8.33d)$$

For the case of equally spaced grid points in the η -direction

($K = 1$), equations (8.33) become

$$\left. \begin{aligned} Y_7 &= - \frac{11}{(6 \Delta\eta)} \\ Y_8 &= \frac{18}{(6 \Delta\eta)} \\ Y_9 &= - \frac{9}{(6 \Delta\eta)} \\ Y_{10} &= \frac{2}{(6 \Delta\eta)} \end{aligned} \right\} \quad (8.34)$$

and equation (8.32) reduces to the familiar four-point relation; that is,

$$\left(\frac{\partial G}{\partial \eta} \right)_{m+1,1} = - \frac{1}{6 \Delta\eta} (11G_{m+1,1} - 18G_{m+1,2} + 9G_{m+1,3} - 2G_{m+1,4}) \quad (8.35)$$

8.1.7 Eddy Viscosity Distribution

The major advantage of the present solution technique in relation to Cebeci, Smith, and Mosinkis (ref. 78) and Beckwith and Bushnell (ref. 86), for example, is that the momentum and energy equations (eqs. (8.29) and (8.30)) are simultaneously solved without iteration, whereas in the above two references the momentum and energy equations are each individually solved and iterated for convergence. The eddy viscosity function distribution $\bar{\epsilon}$ and $\hat{\epsilon}$ (see eqs. (7.15) and (7.16)) and their derivatives with respect to η represent somewhat of a problem unless extreme care is used in the initial extrapolation of the known values of $\bar{\epsilon}_{m-1,n}$ and $\bar{\epsilon}_{m,n}$ to the unknown station, $m+1,n$.

During the development of the digital computer program, the numerical method would frequently become unstable in either the transitional or turbulent flow region (see Section 8.1.8 for discussion of convergence and stability). This problem would always occur in one of two ways. In some instances an apparently converged solution would be obtained, but the distribution of boundary-layer thickness would not be smooth. In other instances, where the transition was abrupt or where boundary conditions were abruptly changed, the solution would not converge. The problem was finally traced back to its origin, which was a nonsmooth or "rippled" eddy viscosity distribution across the layer. These "ripples" first occurred in the region where the inner and outer eddy viscosity models were matched. If the initial "ripples" were below a certain level, the solution would apparently converge, but slightly nonsmooth boundary-layer thickness distributions would occur.

If the initial "ripples" were above a certain level, the disturbance would grow very rapidly as a function of ξ and propagate throughout the layer as the solution proceeded downstream. When this occurred, no valid solution could be obtained downstream of the initial disturbance.

The initial extrapolation of the known values of $\bar{\epsilon}_{m,n}$ and $\bar{\epsilon}_{m-1,n}$ to the unknown grid point $(m+1,n)$ is obtained as follows (see eq. (8.6)):

$$\bar{\epsilon}_{m+1,n} = X_4 \bar{\epsilon}_{m,n} - X_5 \bar{\epsilon}_{m-1,n} \quad (8.36)$$

However, there is no assurance that the distribution of the extrapolated values at station $m+1$ will be smooth across the layer for all possible flow conditions. If "ripples" occur in the extrapolated $\bar{\epsilon}$ distribution and if these "ripples" are of sufficient magnitude to cause the sign of the derivative of $\bar{\epsilon}$ with respect to η to alternate, then the method becomes highly unstable.

The requirement of small grid-point spacing in the law of the wall region contributes to the instability problem in that the size of an "acceptable ripple" is a function of the grid-point spacing being utilized in the η -direction. For turbulent layers where the viscous sublayer is relatively thick, the grid-point spacing in the outer portion of the law of the wall region will be large in comparison to cases where the viscous sublayer is relatively thin. Consequently, the former case can tolerate a "larger ripple" in the region of the

match point than can the latter case without experiencing an alternation in the sign of the derivative of $\bar{\epsilon}$ with respect to η .

There are two possible ways to eliminate the problem caused by the "ripples" in the eddy viscosity distribution. The first approach is to develop an iteration scheme in which case the present solution technique has no advantage in relation to the technique used in reference 86; that is, the advantage of the unique simultaneous solution would be lost. The second approach is to numerically smooth the extrapolated eddy viscosity distribution prior to the matrix solution. Both approaches were tried by the author during the development phase of the digital computer program. The second approach was incorporated into the solution and will be discussed in the remaining portion of this section.

The problem posed by the "ripples" in the eddy viscosity distribution, if they exist, can be avoided by utilizing a three-point mean value for $\bar{\epsilon}$ at station $m+1, n$, that is,

$$(\bar{\epsilon}_{av})_{m+1, n} = \frac{\bar{\epsilon}_{m+1, n-1} + \bar{\epsilon}_{m+1, n} + \bar{\epsilon}_{m+1, n+1}}{3} \quad (8.37)$$

where $\bar{\epsilon}_{av}$ denotes the three-point mean of the eddy viscosity function. In the present analysis the eddy viscosity functions appearing on the right-hand side of equation (8.37) are first obtained at each grid point across the $m+1$ station from equation (8.36). Having obtained these values, the three-point mean is evaluated at each of the $N-1$ grid points from equation (8.37). The matrix solution is

then obtained for equations (8.29) and (8.30). Having obtained the $N-1$ values for F , Θ , and V at station $m+1$, the eddy viscosity distribution is recalculated at the $m+1$ station prior to moving to the next ξ grid-point station. This procedure has been found to be stable under all circumstances and to yield convergent solutions for transitional and fully turbulent boundary layers.

8.1.8 Convergence and Stability

The implicit difference scheme utilized in the present analysis is consistent; that is, it may be considered as a formal approximation to the governing partial differential equations. A finite difference scheme is consistent if the difference between the partial differential equation and the difference equation goes to zero as the grid-point spacing approaches zero. That is, a scheme is consistent if the truncation error goes to zero as the grid-point spacing approaches zero. The difference quotients used in the present analysis satisfy this requirement. However, the fact that a system is consistent does not necessarily imply that the solution of the difference equations as the grid-point spacing approaches zero converges to the actual solution of the partial differential equations. In order for convergence to be assured, the difference equation system must be convergent. Unfortunately, for the boundary-layer equations as used herein there is no completely satisfactory mathematical analysis with which the convergence or divergence of the present scheme can be demonstrated (ref. 15). The convergence of the system can best be studied numerically by varying the grid-point spacing. This approach is used in Chapter IX of

the present paper. Convergence problems can become very critical in the turbulent region of the boundary layer when the viscous sublayer is not properly treated. Of course, one should keep in mind that there are no exact solutions of the mean turbulent boundary-layer equations against which comparisons for convergence may be made.

The stability of the finite difference scheme, as opposed to the convergence, can be carefully studied mathematically. The three-point implicit scheme used in the present method is stable regardless of the grid-point spacing (ref. 15, pp. 44-49). The stability of the method is the major advantage of the implicit difference scheme in relation to the explicit approach where it is necessary to control the grid-point spacing through a stability parameter. (See, for example, refs. 87 to 91.)

8.1.9 Viscous Sublayer

The relative thinness of the viscous sublayer (Section 7.4.1) and its importance in determining the correct shear stress and heat flux at the wall requires that very small grid-point spacing in the η -direction be utilized in the wall region for the present numerical procedure. Although a careful study of either the minimum number of grid points that must be located in the viscous sublayer or the optimum spacing of the grid points across the entire boundary layer has not been completed, it has been found by the author that at least 5 to 10 grid points in the viscous sublayer at each x-solution station will yield a convergent solution. (This study is currently being completed

and will be reported in a subsequent NASA publication containing the digital computer program.)

Preliminary data obtained from experimental studies and a thorough literature survey by the Gas Dynamics Section at the Langley Research Center indicates that the viscous sublayer thickness, $y_{s.l.}^+$, ranges from approximately 8 to 14 over the Mach number range from 3 to 47 for adiabatic to cold wall conditions and for air or helium flow mediums. (These data are currently being processed for publication by W. D. Harvey and F. L. Clark at the Langley Research Center.) Consequently, a mean value of $y_{s.l.}^+ = 10$ and equation (7.116a) allows a reasonable estimate of $y_{s.l.}^*$ as follows:

$$y_{s.l.}^* \cong \frac{10 y_{s.l.}^+}{\sqrt{\frac{\tau_w^*}{\rho_w^*}}} \quad (8.38)$$

where the local values of v^* and ρ^* in equation (7.116a) have been replaced with the known wall values in equation (8.38). An accurate estimate of the value of τ_w^* for a particular case can be obtained from a number of current correlations, for example, Spalding and Chi (ref. 92). Therefore, an estimate of $y_{s.l.}^*$ can be obtained from equation (8.38); however, the numerical solution is obtained in the transformed plane. The sublayer thickness in the transformed plane can then be obtained directly from equations (7.33b) and the estimated $y_{s.l.}^*$ value. The final step is to estimate the boundary-layer thickness and the optimum total number of grid points across the boundary layer. Having reasonably accurate estimates of the viscous sublayer thickness,

the total boundary-layer thickness, and the optimum number of grid points, equations (8.1) to (8.3) can then be used to obtain the spacing parameter, K , in order to place from 5 to 10 grid points in the viscous sublayer. An example of the effect of grid-point spacing on the convergence of the numerical method is presented in Section 9.1.

8.2 Digital Computer Program

The repetitious nature of the implicit finite-difference scheme makes the method well suited for digital computers. The present solution technique was programed by the author for the CDC (Control Data Corporation) 6000 series computer operating on Scope 3. The coded program will not be presented herein since it is quite lengthy as well as currently being documented for publication by the National Aeronautics and Space Administration.

The main objectives in the development of the computer program used in the present study were accuracy, minimum computation process time, flexibility, and simplicity. The accuracy requirement is, of course, of paramount importance in any numerical procedure. The CDC 6000 series machines cost on the order of \$1 thousand per hour to operate. Consequently, the computer process time per test case must be held to a minimum by optimum programing procedures. Both of these requirements should be carefully considered in any digital computer program. However, flexibility and simplicity are often overlooked when the primary objective of the study is to obtain solutions for one particular class of flows in order to satisfy one specific requirement.

The importance of simplicity in input requirements is also often neglected when the needs of other personnel associated with the research center, university, or aerospace industry are not taken into consideration. These objectives were necessary in the present case since the program was developed by the author for general use at the National Aeronautics and Space Administration, Langley Research Center. Some of the more important points concerning the flexibility of the program will be discussed in the remaining portion of this section.

The input requirements that must be specified in order to obtain the external flow are discussed in Section 7.8. The input values for $P_{t,\infty}^*$, $T_{t,\infty}^*$, M_∞ , σ , σ_t , γ , C_p^* , and S^* are dependent upon only the free-stream test conditions and flow medium. However, P_e^* which must be specified as a function of the boundary-layer coordinate, x^* , is a function not only of the test conditions and flow medium, but also body geometry. The pressure distribution, P_e^* , as a function of the boundary-layer coordinate, x^* , is obtained from experimental data when possible or from the method presented in reference 80, when applicable. A very useful option for engineering studies of the boundary-layer characteristics has been provided by programming Modified Newtonian pressure relations (ref. 93) directly into the program for blunt-body flows; that is,

$$P_e = P_{t,\infty} \left(1 + \frac{\gamma - 1}{2} M_\infty^2 \right)^{-\gamma/\gamma-1} \left(1 + \frac{\gamma M_\infty^2}{2} C_{p_{\max}} \cos^2 \phi \right) \quad (8.39)$$

where the maximum pressure coefficient, $C_{p_{\max}}$ may be expressed as

$$C_{p_{\max}} = \frac{\gamma + 3}{\gamma + 1} \left[1 - \frac{2}{M_{\infty}^2 (\gamma + 3)} \right] \quad (8.40)$$

This option is particularly useful for cases where engineering design data are required for a particular class of configurations over a broad range of flight conditions. A good example would be the class of power-law bodies for which equation (8.39) will yield an accurate representation of the true pressure distribution at hypersonic speeds (ref. 94). This class of bodies may be described mathematically as follows:

$$\frac{r_o}{r_b} = \left(\frac{z}{L} \right)^a \quad (8.41)$$

where r_b designates the base radius for a body of length L . For this particular example, the power-law exponent, a , could be varied to study the viscous drag over a range of flight conditions with a minimum of input requirements. Another very useful application would be to study the heat transfer to the vehicle over a given flight trajectory. In this case the variable input required for the solution would be specific values of $P_{t,\infty}^*$, $T_{t,\infty}^*$, and M_{∞} at points along the trajectory. The most probable location of transition and the extent of the transition region would be obtained from empirical correlation relations (see Section 7.5).

It should be noted that the above-mentioned class of bodies (eq. (8.41)) presents somewhat of a problem in that the boundary-layer

coordinate, x , cannot be obtained in closed form as a function of the body coordinates, z and r_0 . This presents no problem in the present program, since the program contains an iteration subroutine which will obtain x as a function of the body coordinates for any geometry where r_0 can be expressed as a function of z .

IX. EXAMPLE SOLUTIONS FOR THE SYSTEM OF EQUATIONS

The finite difference solution technique developed in Chapter VIII together with the transition criteria, transitional flow structure, and transition extent discussed in Chapter VII is applied in the present chapter to a number of typical supersonic and hypersonic configurations of current interest. In all cases the gas is assumed to be perfect air with a constant ratio of specific heats, γ , equal to 1.4, a constant Prandtl number, σ , equal to 0.72, and a constant static turbulent Prandtl number, σ_t , equal to 0.9. The molecular viscosity, μ , is evaluated from Sutherland's viscosity law (eq. (7.32)). The external pressure distributions used are either experimental or were obtained by the author from an exact solution of the full inviscid Euler equations obtained at the Langley Research Center (ref. 80).

The selection of a typical set of test cases always presents a problem since there are so many possibilities from which to choose. However, the cases considered in the present chapter should serve as an indication of the merits of the solution technique as well as the validity of the system of equations.

9.1 High Reynolds Number Turbulent Flow

The accurate prediction of boundary-layer characteristics for high Reynolds number turbulent flow is important in the design of high-speed vehicles. In particular, it is important to be able to predict with accuracy the skin friction drag. An excellent comparison case of

high Reynolds number turbulent flow is the data of Moore and Harkness (ref. 95). The experimental skin friction data were measured with a floating element type balance. The test model was a 10-foot-long, 4-foot-wide sharp (0.002 to 0.004 inch thick) leading-edge flat plate. The test conditions were as follows:

$$M_{\infty} = 2.8$$

$$P_{t,\infty}^* = 2.088 \times 10^4 \text{ lb/ft}^2$$

$$T_{t,\infty}^* = 5.6 \times 10^2 \text{ } ^\circ\text{R}$$

$$\frac{T_w^*}{T_{t,\infty}^*} = 9.47 \times 10^{-1}$$

The experimental transition location was not reported in reference 95. Consequently, for the numerical calculations, the transition location was determined by the stability index (Section 7.5.2.1) and was assumed to occur at the x-station where χ_{\max} achieved a value of 2,500. The extent of the transition region was automatically calculated from equation (7.85). The intermittency distribution was calculated from equation (7.81). The solution was started at the leading edge of the sharp flat plate ($x = 0$) by obtaining an exact numerical solution of the similar boundary-layer equations (eqs. (A-47) to (A-49)) by the method discussed in Section 8.1.5. The grid-point spacing was varied in both the ξ and η directions in order to check for convergence. It should be noted that the selection of $(\chi_{\max})_{cr} = 2,500$ was based partially on experience and partially on the results presented

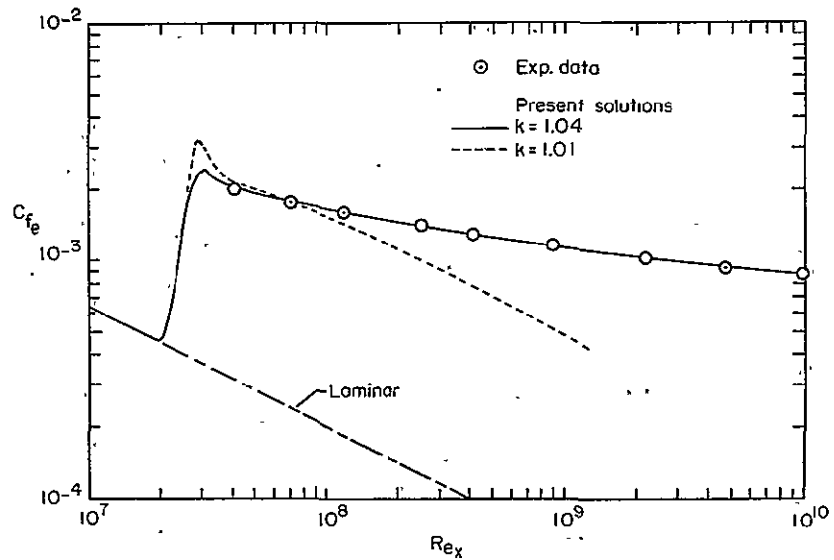
in Section 9.8 where the variation of $(x_{\max})_{cr}$ with R_e^* is discussed. The location of transition ranged from 0.84 to 1.4 inches from the leading edge for $(x_{\max})_{cr}$ between 2,500 and 3,500, respectively. This variation in transition location had negligible effect on the skin friction coefficients in the fully turbulent region of flow.

The numerical results for the skin friction coefficient distribution are compared to the experimental data in figure 10(a). The agreement is excellent over the entire Reynolds number range of the experimental data for $K = 1.04$; however, for $K = 1.01$, convergence was not attained. It should be noted at this point that the terms convergence and stability, as used in relation to the numerical method, are defined herein as in reference 15 and are discussed in Section 8.1.8. The divergence (failure to obtain a convergent solution) for $K = 1.01$ is attributed to an insufficient number of grid points in the wall region; in particular, in the thin viscous sublayer region. This particular problem is discussed in Section 8.1.9. The effect of the grid-point spacing parameter K on the numerical solution was studied for additional values of 1.02, 1.03, 1.05, and 1.06. The solution was found to diverge for $K < 1.02$ and converge for $K \geq 1.02$. The C_{f_e} results for $K \geq 1.02$ (other than $K = 1.04$) are not presented since the variation of C_{f_e} with K would not be discernible if plotted to the scale of figure 10(a). The convergence criteria used in this particular example was to decrease the grid-point spacing until any change which occurred in C_{f_e} at a given x -solution station was beyond the fourth significant digit. The laminar curve shown in figure 10(a)

was obtained by suppressing transition ($\Gamma = 0$). Grid-point spacing in the ξ -direction was varied from $\Delta x = 0.001$ to 0.04 , and convergence to the accuracy of the experimental data was obtained for all values. Because of the abruptness of transition, step sizes greater than $\Delta x = 0.04$ were not studied.

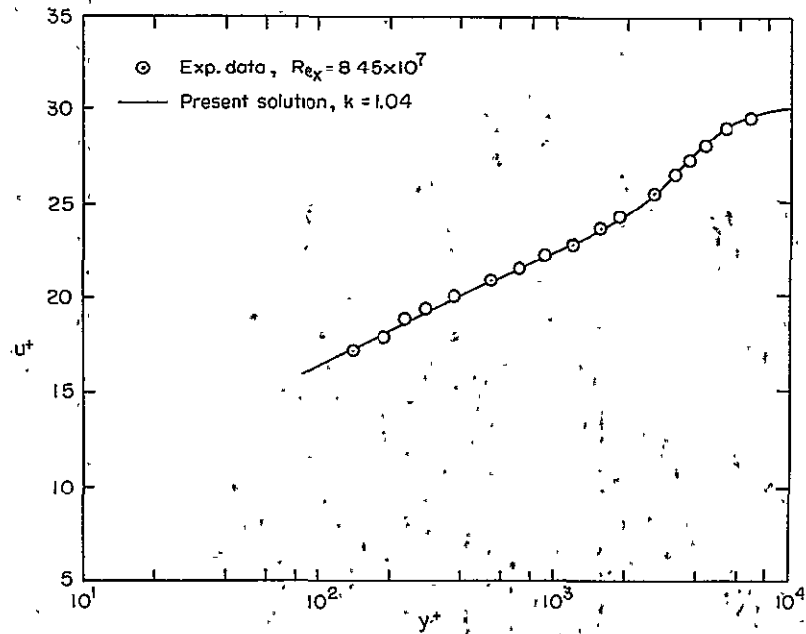
A comparison to an experimental velocity profile is presented in figure 10(b). The profile was obtained at an Re_x value of 8.45×10^7 . No experimental data were available for y^+ values less than 10^2 . The agreement between the numerical results and the experimental profile is seen to be very good.

Typical profiles of F , Θ , $P_{tm}/P_{tm,e}$, and M/M_e just prior to transition ($Re_x = 1.46 \times 10^6$), midway through the transition region ($Re_x = 1.96 \times 10^6$), and at the completion of transition ($Re_x = 3.44 \times 10^6$) are presented in figures 10(c) to 10(f), respectively. No experimental data were available in this region; however, the results are, in general, typical of any transition region (see Section 9.8). The intermittency distribution and boundary-layer thickness distribution in the transition region are presented in figures 10(g) and 10(h), respectively.



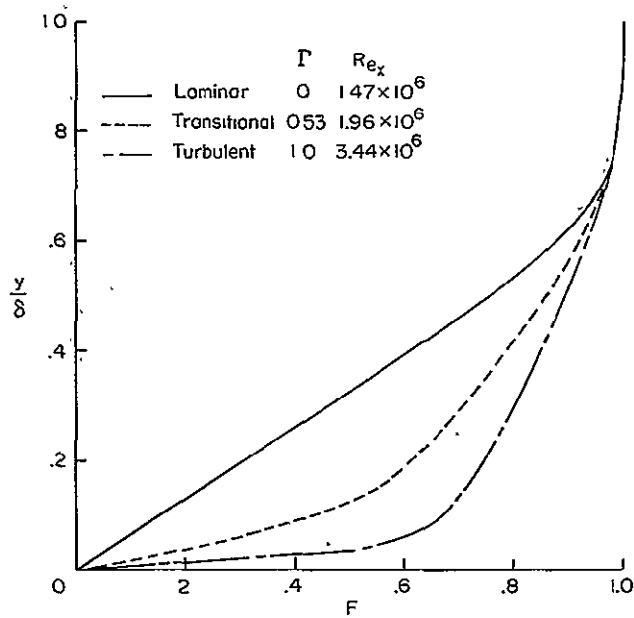
(a) Comparisons to skin friction coefficient data.

Figure 10.- High Reynolds number turbulent flow.



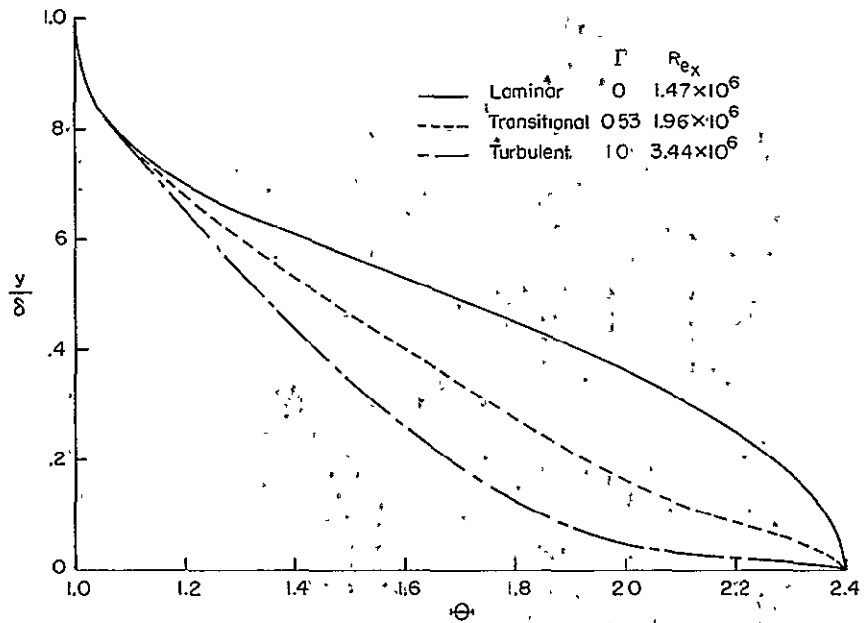
(b) Comparison to velocity profile data.

Figure 10.- Continued.



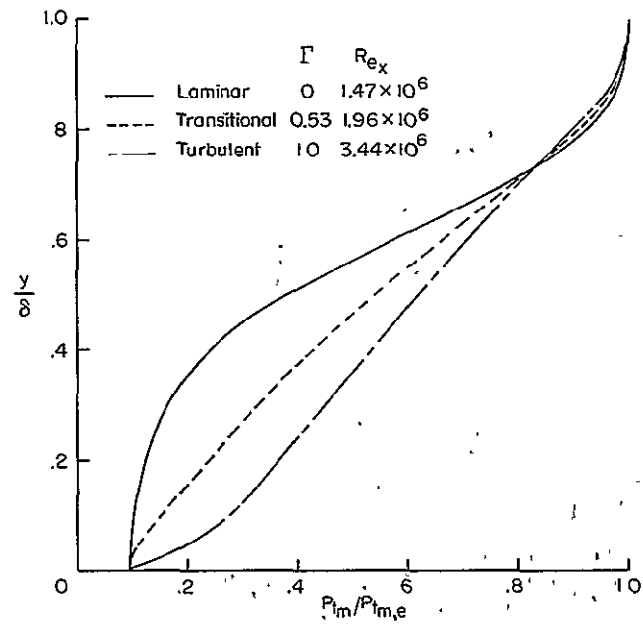
(c) Transition region velocity profiles.

Figure 10.- Continued.



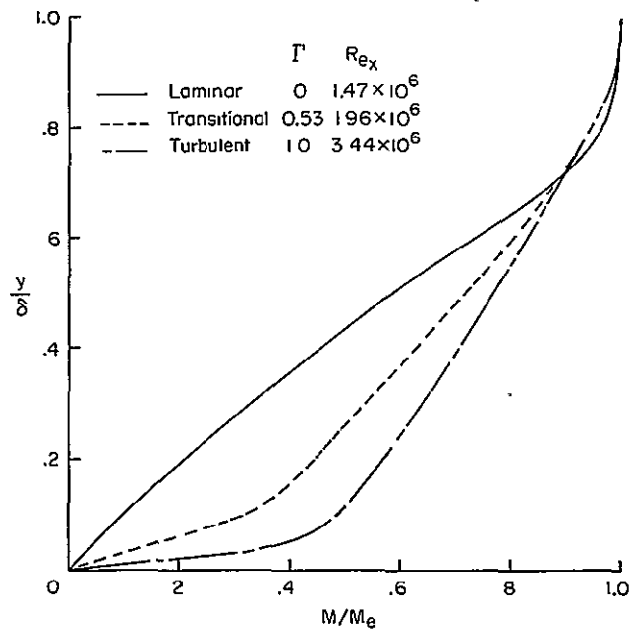
(d) Transition region temperature profiles.

Figure 10.- Continued.



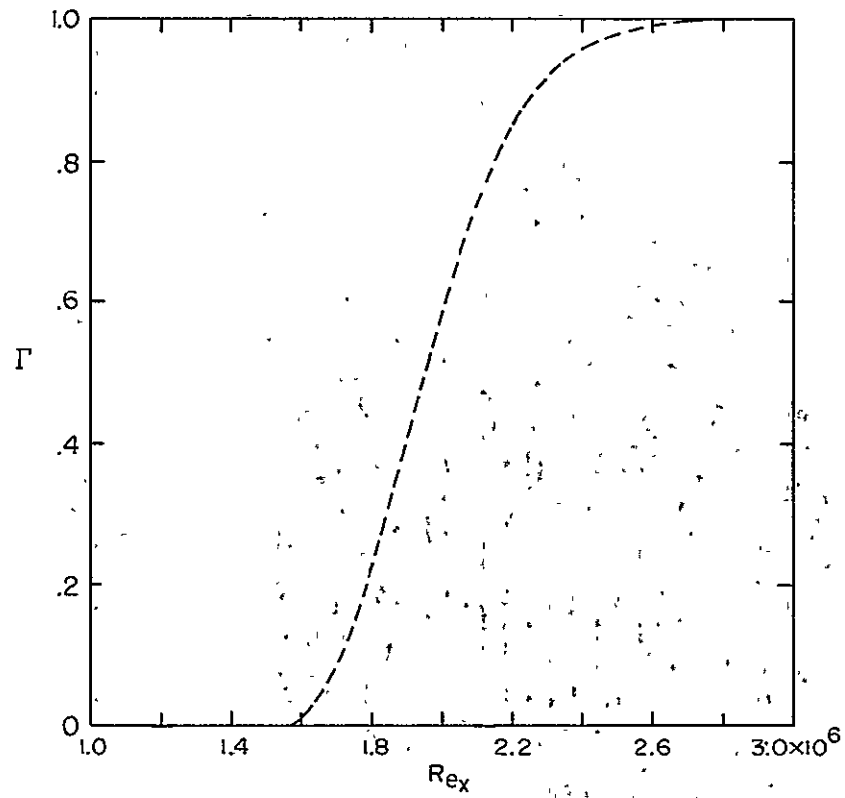
(e) Transition region total pressure profiles.

Figure 10.- Continued.



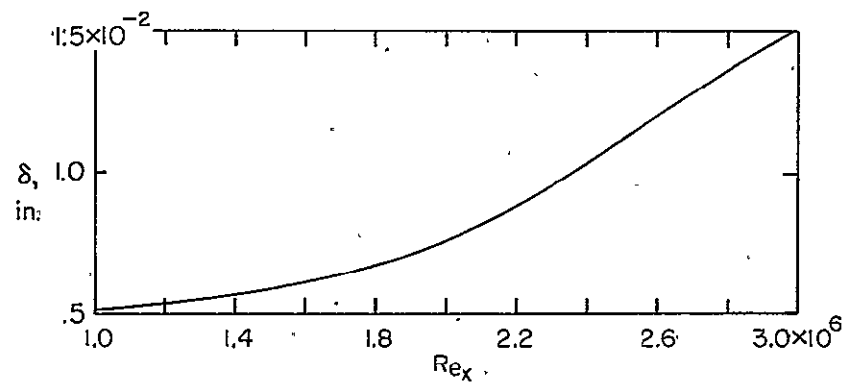
(f) Transition region Mach number profiles.

Figure 10.- Continued.



(g) Intermittency distribution in transition region.

Figure 10.- Continued.



(h) Boundary-layer thickness in transition region.

Figure 10.- Concluded.

9.2 Tripped Turbulent Boundary Layers

In many of the current supersonic wind-tunnel facilities it is often necessary to trip the laminar boundary layer artificially in order to obtain turbulent data. A good example of turbulent data obtained in tripped boundary layers is that of Coles (ref. 96). These data were obtained in the Jet Propulsion Laboratory's 20-inch supersonic wind tunnel. The test model was a sharp leading-edge flat plate. The free-stream Mach number was varied from 1.966 to 4.544. Test numbers 30, 20, and 22 (see page 33 of ref. 96) were selected as typical comparison cases. For these three cases the laminar boundary layer was tripped by a fence located at the leading edge of the flat plate (see fig. 40 of ref. 96). The skin friction was measured at three surface locations with a floating element balance. Boundary-layer profiles were measured at $x^* = 21.48$ inches.

The test conditions for the three comparison cases are listed in tabular form below.

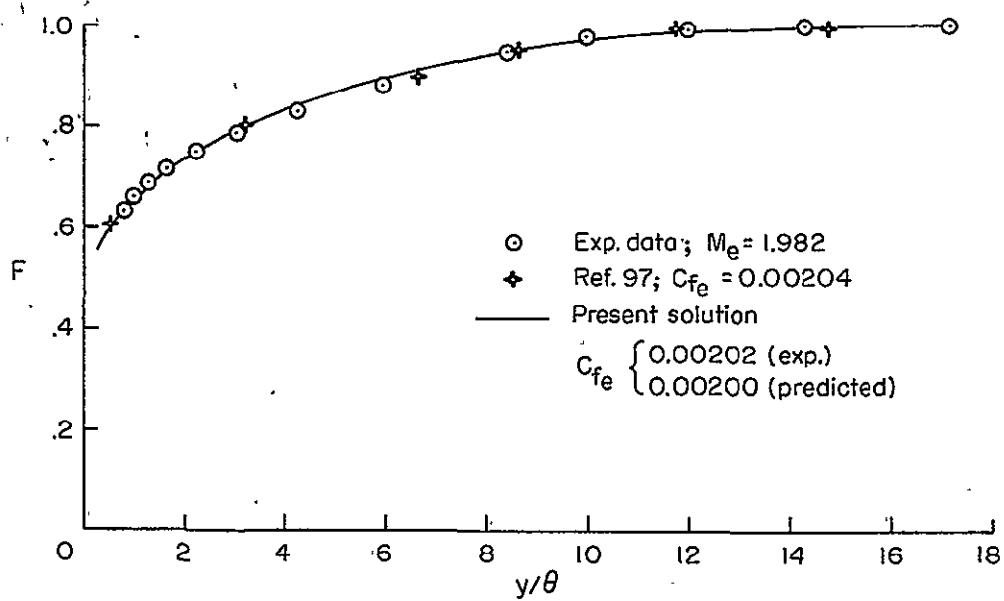
Coles test No.	M_e	$P_{t,\infty}^*$ lb/ft ²	$T_{t,\infty}^*$ °R	$T_w^*/T_{t,\infty}^*$
30	1.982	1977.4	545	0.8295
20	3.701	2868.5	561	.7152
22	4.554	8132.2	554	.6764

Transition was assumed to occur near the leading edge of the plate for the numerical calculations, $x_{t,1}^* = 0.005$ ft, and to be

completed ($\Gamma = 1.0$) at $x_{t,f}^* = 0.010$ ft. Twenty equally spaced x -solution stations were used in the region $0 \leq x^* \leq 0.010$ ft; the x -solution stations were then equally spaced 0.01 ft apart over the remainder of the plate. The total number of grid points in the η -direction and the grid-point spacing parameter K were assigned values of 301 and 1.04, respectively. The computer processing time per test case was approximately 3 minutes. The numerical results are compared to the experimental velocity and Mach number profile data in figures 11(a) to 11(f) for the three test cases. The agreement between the numerical results and the experimental data is very good for all three test cases. In particular, it should be noted that the experimental skin friction coefficients (see figs. 11(a), 11(c), and 11(e)) were predicted to within 1 percent, which is well within the accuracy range of 2 percent as quoted for the data in reference 96.

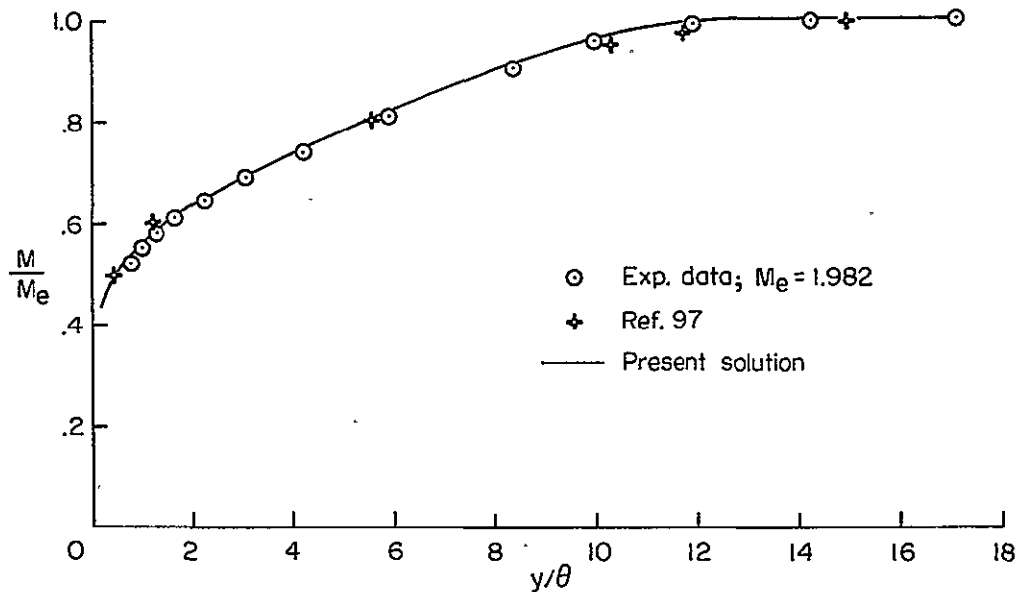
Numerical results obtained by Fletcher¹ (ref. 97; see, also, ref. 98) are also presented on figures 11(a) to 11(f). A three-layer mixing length concept was used in reference 97 to model the turbulent transport terms. The resulting equations were solved by an explicit finite difference technique using the DuFort-Frankel (ref. 99) difference scheme. The agreement between the numerical results of reference 97 and those of the present solution is very good for the three test cases. To the author's knowledge, the method used in reference 97 is the only explicit finite difference technique currently being used to solve the mean flow turbulent boundary-layer equations.

¹The author would like to thank Professor R. H. Fletcher, Department of Mechanical Engineering, and Engineering Research Institute, Iowa State University, Ames, Iowa, for permission to use these data.



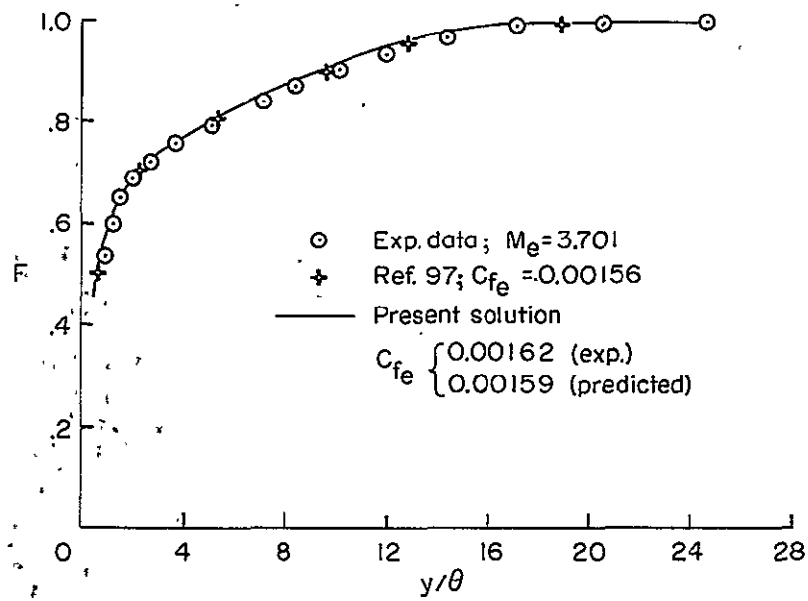
(a) Velocity profile and skin friction coefficient for $M_\infty = 1.982$.

Figure 11.- Comparisons with experimental data for tripped turbulent boundary layers.



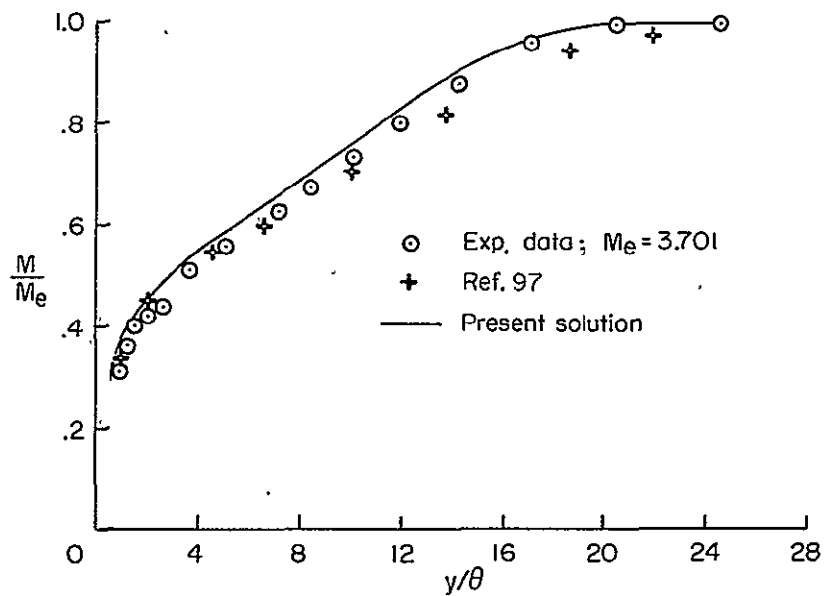
(b) Mach number profile for $M_\infty = 1.982$.

Figure 11.- Continued.



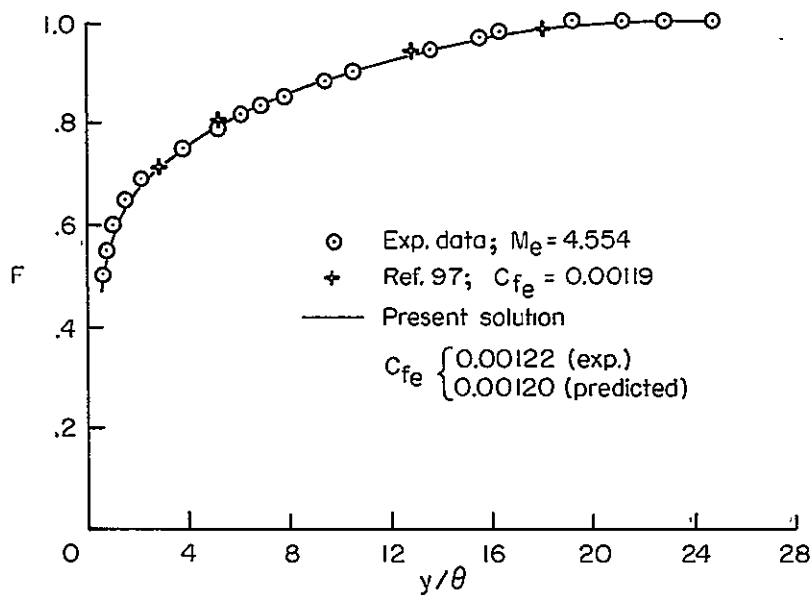
(c) Velocity profile and skin friction coefficient for $M_\infty = 3.701$.

Figure 11.- Continued.



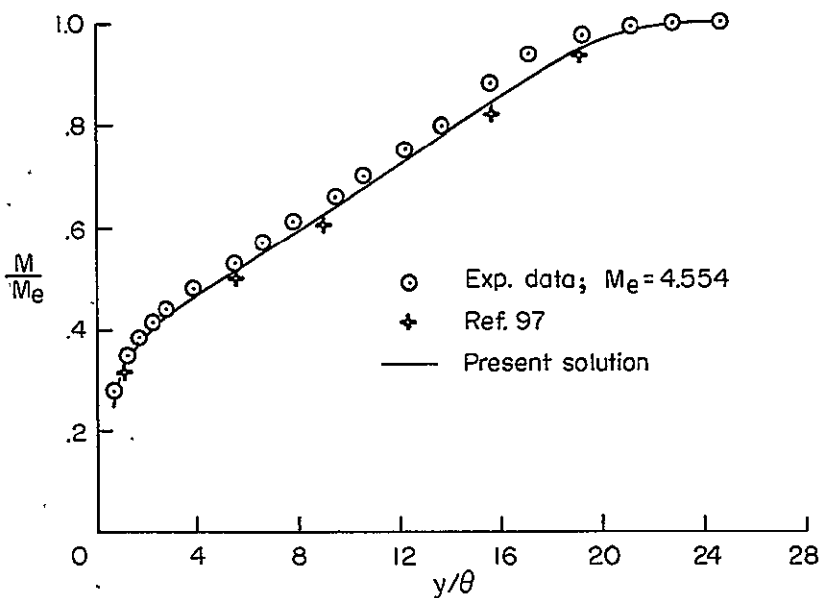
(d) Mach number profile for $M_\infty = 3.701$.

Figure 11.- Continued.



(e) Velocity profile and skin friction coefficient for $M_\infty = 4.554$.

Figure 11.- Continued.



(f) Mach number profile for $M_\infty = 4.554$.

Figure 11.- Concluded.

9.3 Laminar Flow With Mass Injection

In some instances it may become necessary to protect high-performance vehicles by transpiration cooling (mass injection at the wall). An example of laminar data that may be used for comparison is presented by Marvin and Akin (ref. 100). The data were obtained over a range of injection rates for a sharp-tipped 5° cone. The cone was solid for $x^* < 3.75$ inches; the remaining portion of the cone was porous. The test conditions were as follows:

$$M_\infty = 7.4$$

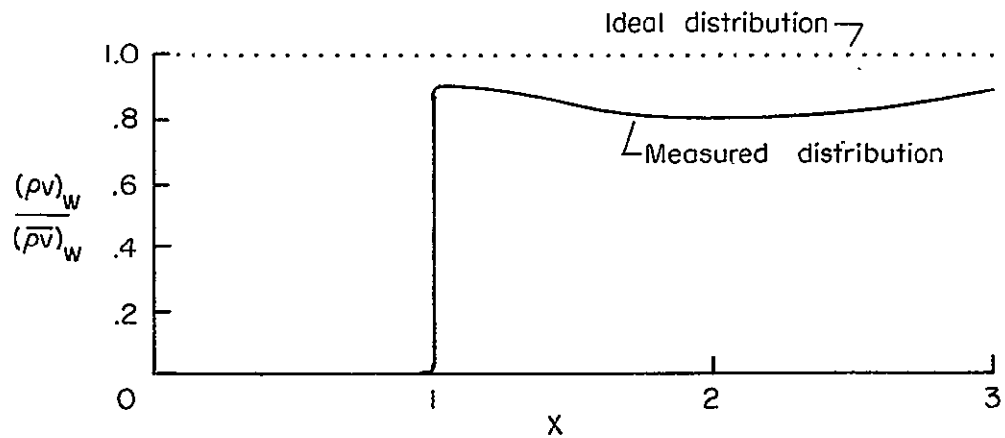
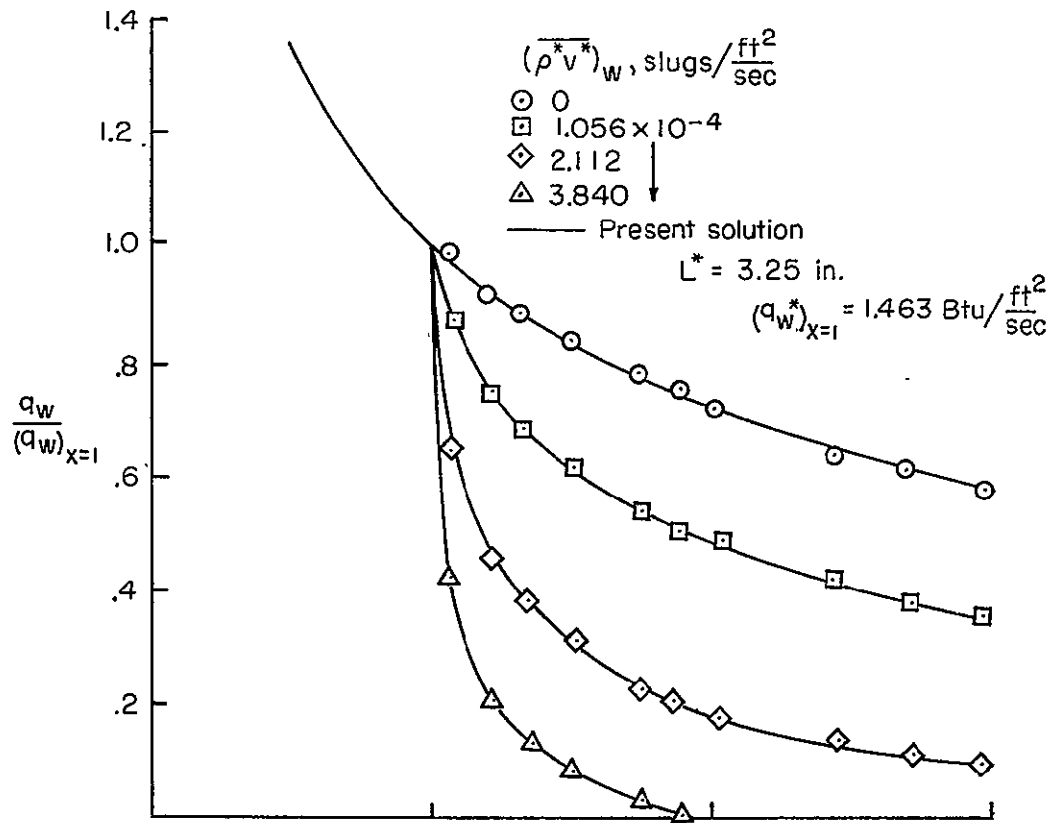
$$P_{t,\infty}^* = 8.64 \times 10^4 \text{ lb/ft}^2$$

$$T_{t,\infty}^* = 1.5 \times 10^3 \text{ }^\circ\text{R}$$

$$\frac{T_w^*}{T_{t,\infty}^*} = 3.8 \times 10^{-1}$$

The air injection rate ranged from 1.056×10^{-4} slugs/(ft²-sec) to a maximum value of 3.84×10^{-4} slugs/(ft²-sec).

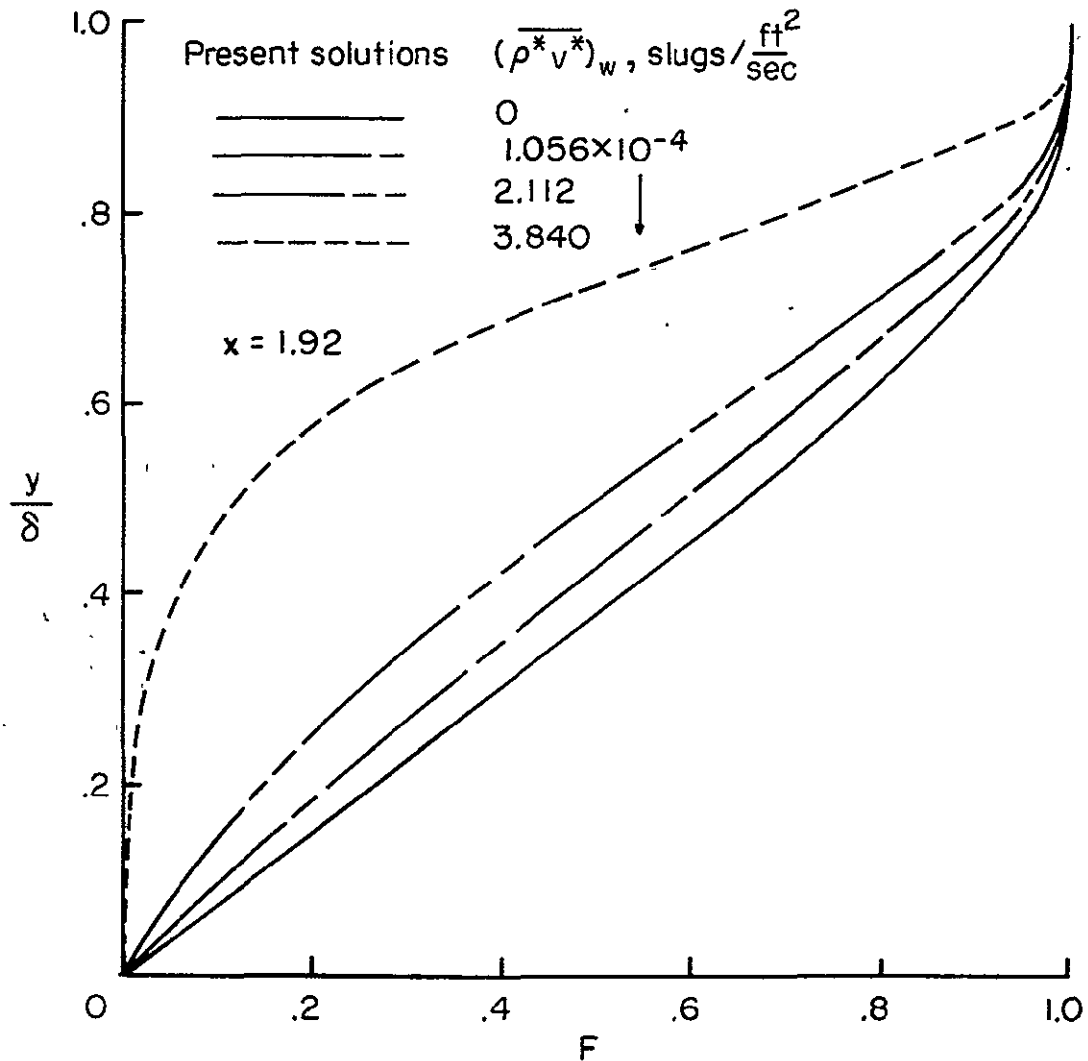
A comparison of the heating rate at the wall normalized by the heating rate at the wall just prior to the ramp injection ($x = 1$) is presented in figure 12(a). The mass injection distribution was not uniform, as can be seen from the plot of the actual injection distribution normalized by the ideal injection rate. The non-uniform distribution of mass injection was utilized in the numerical solutions. The agreement between the numerical results and the experimental heat transfer data is excellent over the entire injection range.



(a) Comparisons to heat-transfer data.

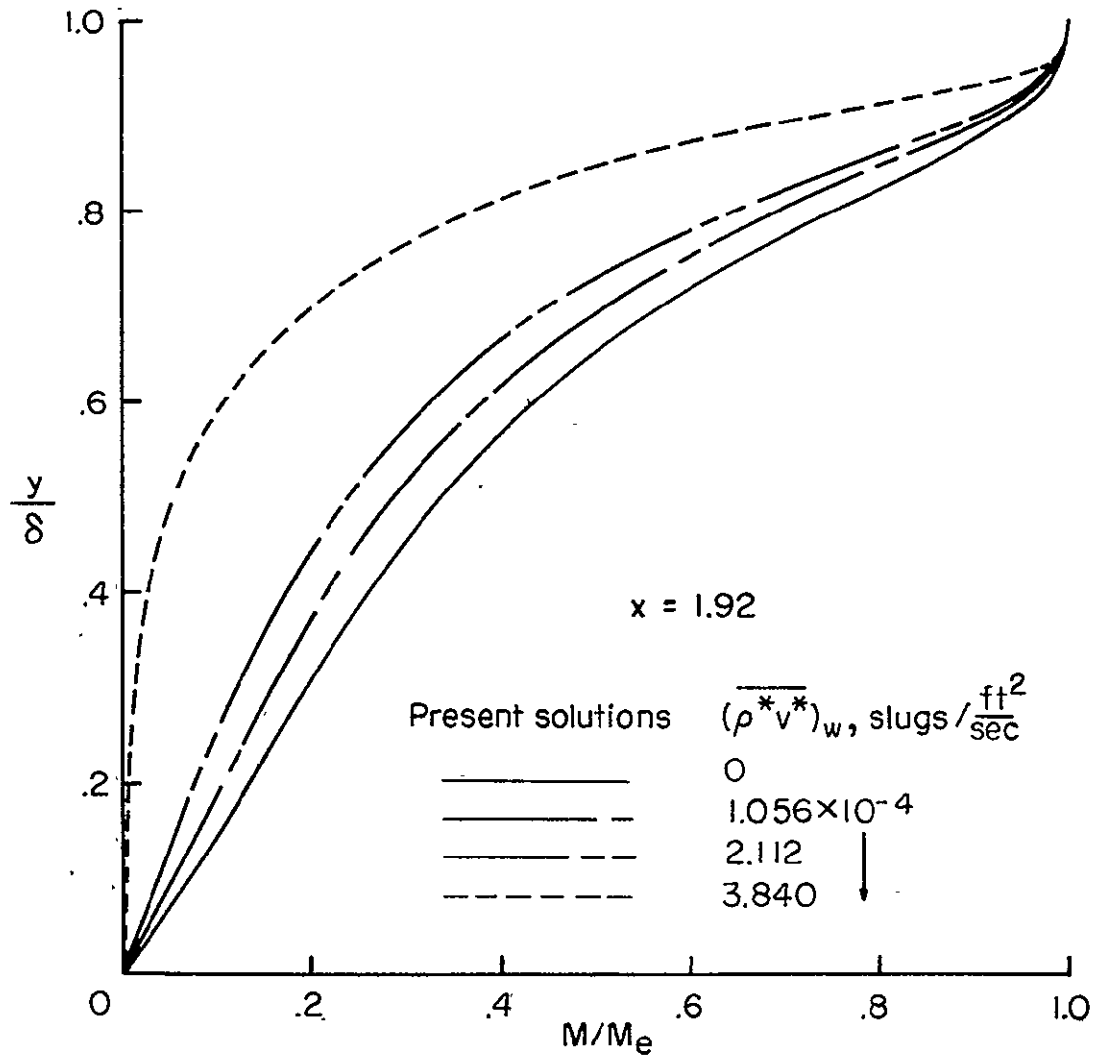
Figure 12.- Hypersonic laminar boundary layer flow with mass injection.

For the maximum injection rate $(\overline{\rho^* v^*})_w = 3.84 \text{ slugs/ft}^2/\text{sec}$, the boundary layer separated from the cone surface at $x = 1.92$. The calculated velocity and Mach number profiles at $x = 1.92$ are presented for the four test cases in figures 12(b) and 12(c), respectively.



(b) Velocity profiles.

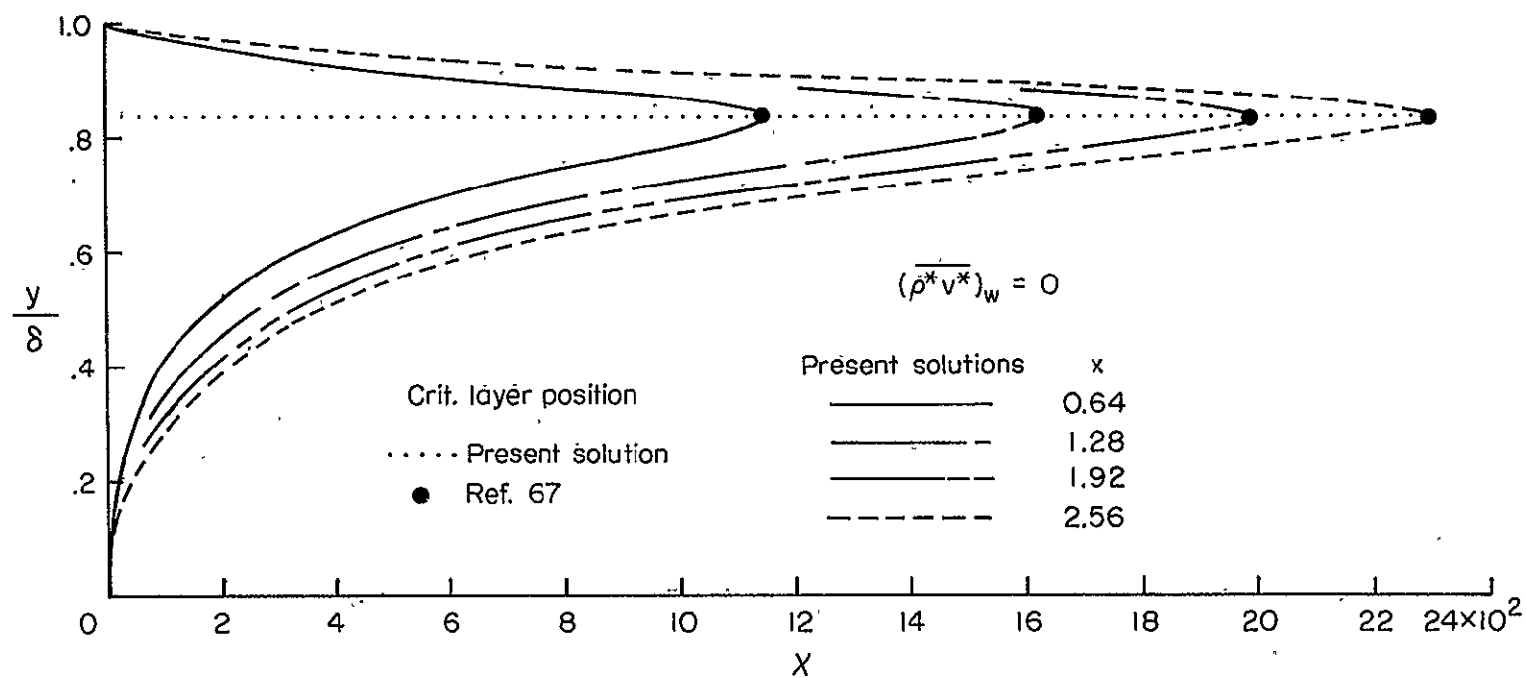
Figure 12.- Continued.



(c) Mach number profiles.

Figure 12.- Continued.

The vorticity Reynolds number distribution for $(\rho^* v^*)_w = 0$ is presented in figure 12(d). The maximum value of the vorticity Reynolds number, χ_{max} , is seen to increase with increasing x . In particular, the y/δ value at which χ_{max} occurred is in excellent agreement with the location of the critical layer position (see ref. 67). The effect



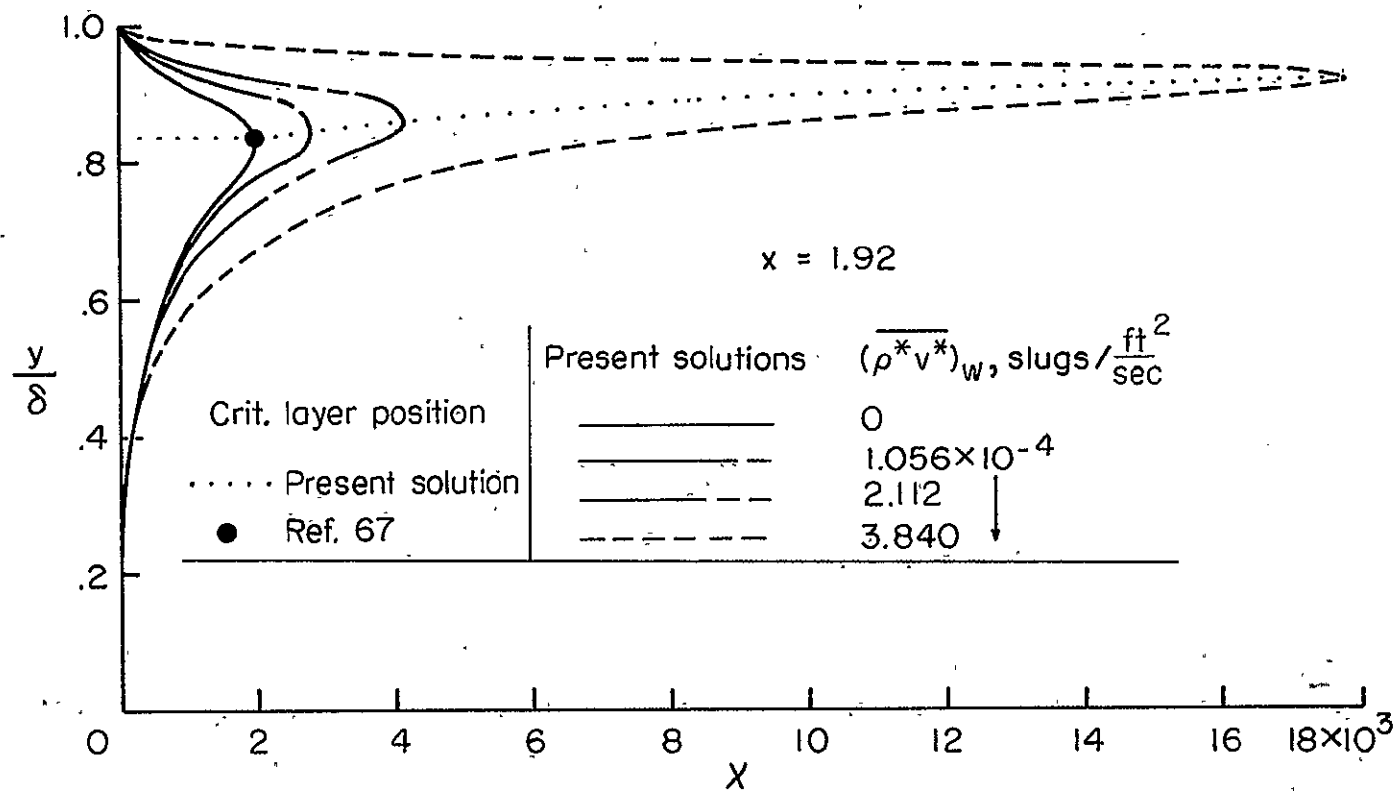
(d) Vorticity Reynolds number distribution for zero mass injection.

Figure 12.- Continued.

of mass injection on the vorticity Reynolds number distribution is presented in figure 12(e). Increasing mass injection is seen to increase the value of x_{\max} at a given x-station as well as move the location at which the maximum occurs, $(y/\delta)_{x_{\max}}$ toward the outer edge of the boundary layer. To the author's knowledge no data are currently available for the critical layer position with mass injection at the wall.

This particular example is a case where variable step size must be utilized in the region of the ramp injection ($x = 1.0$). For this test case, the Δx values (grid-point spacing in x-direction) were constant and equal to 0.01 up to $x = 0.99$ at which point the step size was decreased to a value of 0.001 through the ramp injection region. The step size was then progressively increased up to a value of 0.01 at $x = 1.5$. The flow was laminar; consequently, K was set to unity and 101 equally spaced grid points were utilized in the η -direction. The digital computer processing time per test case was approximately 2 minutes.

It should be noted that the test conditions as listed in references 100 and 101 are not correct. The conditions given herein are correct and were obtained by the author from Mr. Joseph Marvin at the Ames Research Center.



(e) Vorticity Reynolds number distribution for variable mass injection.

Figure 12.- Concluded.

9.4 Blunt Body Flow

The numerical procedure as presented in the present paper has been applied to a number of blunt body supersonic and hypersonic flows. A typical case is presented in figure 13 for hypersonic flow. The pressure distribution was obtained by the author at the Langley Research Center (ref. 80). The test conditions were as follows:

$$M_{\infty} = 10.4$$

$$T_{t,\infty}^* = 2.2 \times 10^3 \text{ } ^\circ\text{R}$$

$$P_{t,\infty}^* = 2.249 \times 10^5 \text{ lb/ft}^2$$

$$\frac{T_w^*}{T_{t,\infty}^*} = 2.5 \times 10^{-1}$$

Solutions for this particular example have been obtained by Marvin and Sheaffer (ref. 101) and Clutter and Smith (ref. 102). The distributions of the heating rate at the wall referenced to the value at the stagnation point ($x = 0$) and the shear stress at the wall are compared to the results presented in references 101 and 102 and are presented in figure 13.

Equally spaced grid points were used in the ξ -direction. Solutions for Δx values of 0.001 to 0.02 were obtained to check for convergence. Oscillations in the q_w due to the starting procedure approached zero after approximately 10 to 15 steps along the surface. The data shown in figure 13 were obtained using $\Delta x = 0.005$, although much larger steps could be used for engineering calculations, say, $\Delta x = 0.01$. The grid-point spacing in the η -direction was constant ($K = 1$) with a value of 0.01. The computation time per body station was about 3 seconds as compared to 42 seconds in reference 102.

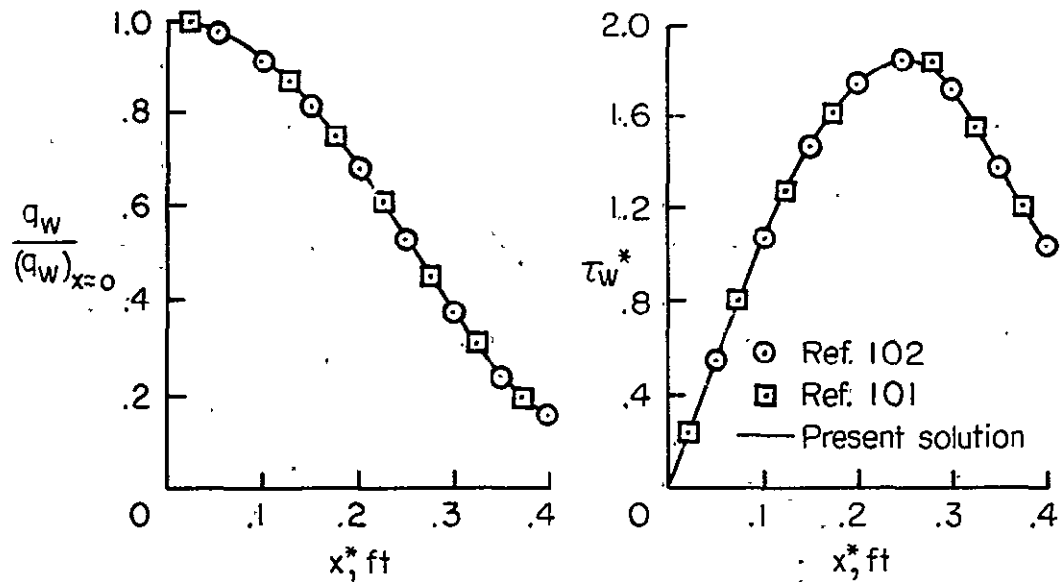
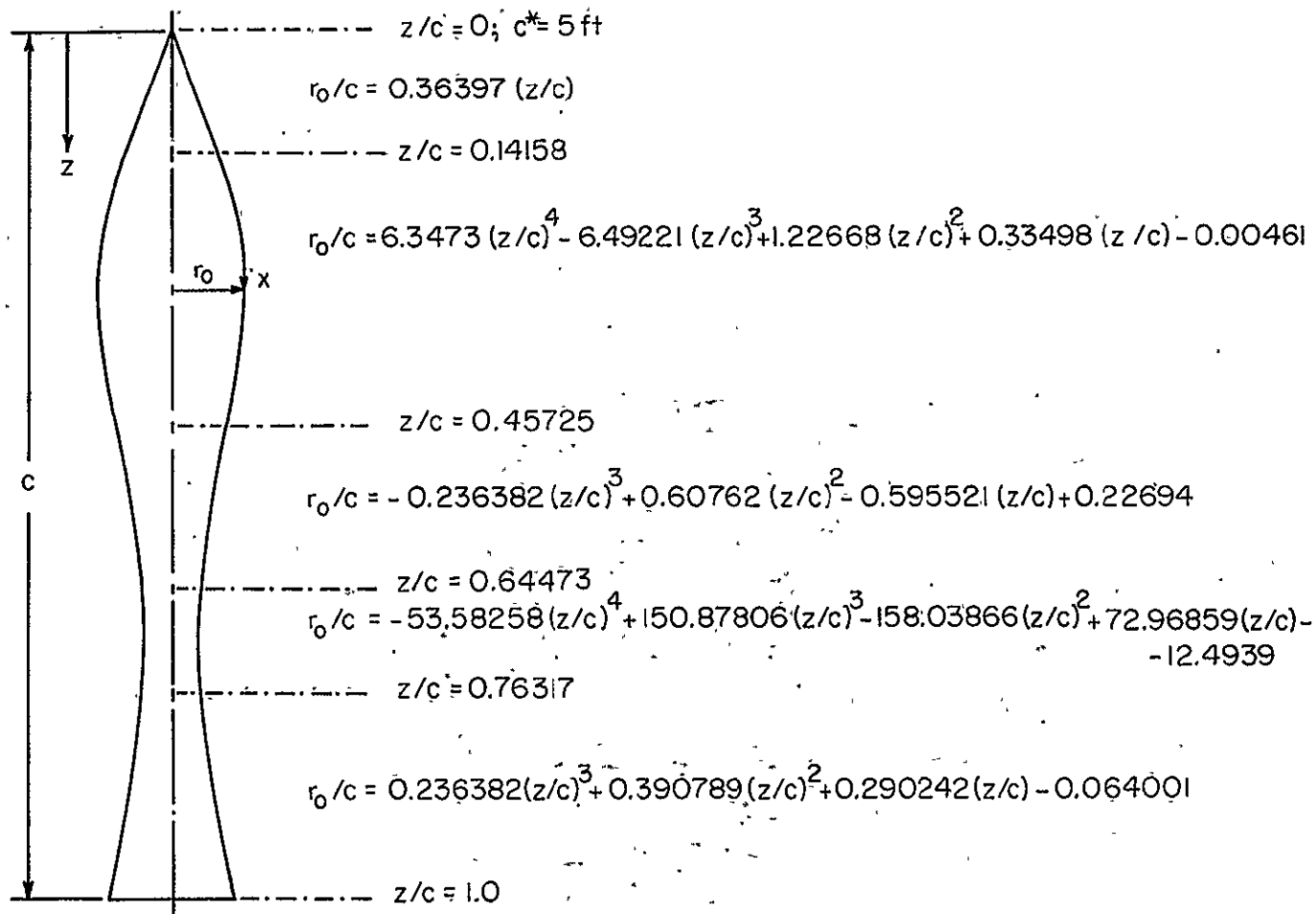


Figure 13.- Hypersonic blunt body flow.

9.5 Highly Nonsimilar Flow With Transverse Curvature

Turbulent boundary layer data for flows where variable pressure gradients exist are few in number. A good example of a case where both favorable and adverse pressure gradients occur as well as where transverse curvature effects are important is the data of Winter, Rotta, and Smith (ref. 103). The model used in the study was an axisymmetric piecewise continuous configuration and is presented in figure 14(a).

Experimental data are presented in reference 103 only for the region where the boundary layer is turbulent; however, the solutions presented herein were obtained by starting the calculations at the tip of the sharp cone forebody ($x = 0$). This particular configuration has received considerable attention over the past 2-year period.



(a) Geometry of configuration.

Figure 14.-- Comparisons with data for highly nonsimilar supersonic flow with transverse curvature effects.

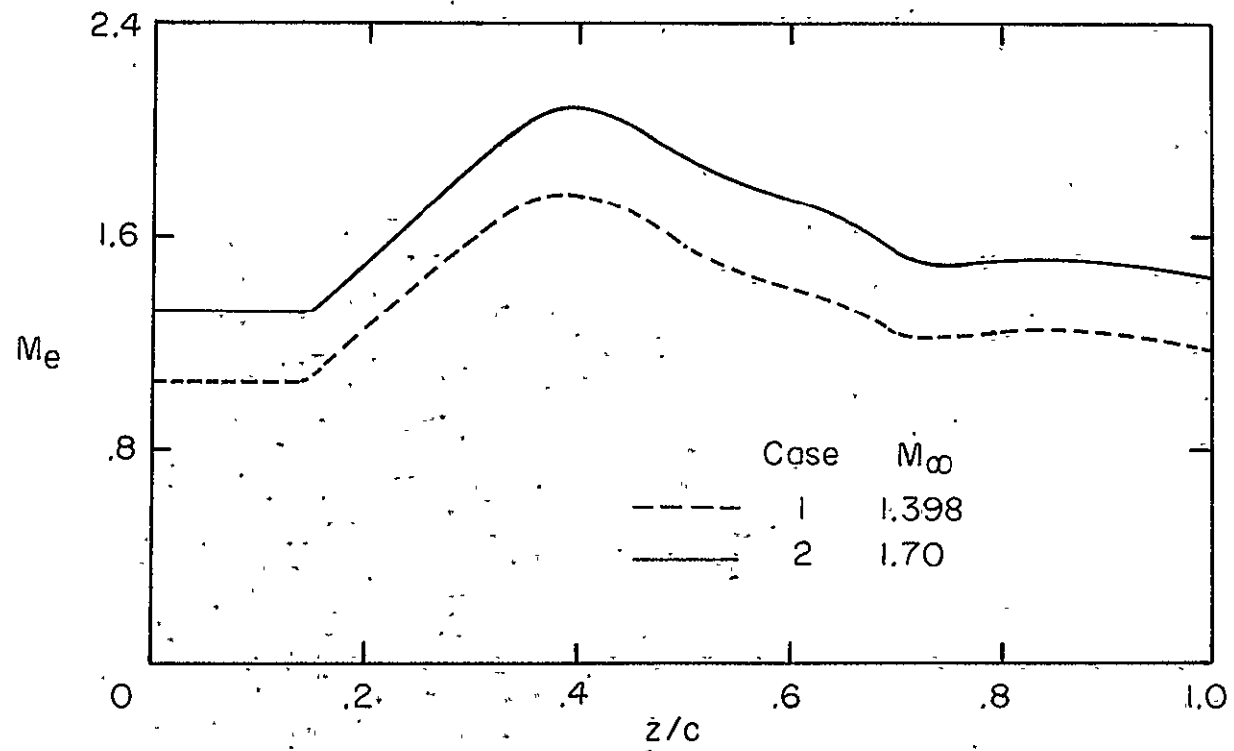
Calculations have been made by Herring and Mellor (ref. 104), Cebeci, Smith, and Mosinskis (ref. 78), and Bushnell and Beckwith (ref. 31). However, the above-mentioned solutions were all started by utilizing the experimentally measured profiles at station $z = 2$. To the author's knowledge the solutions presented in the present paper are the first to be obtained without any dependence whatsoever on experimental profile or skin friction data.

The test conditions for the two cases considered are as follows:

<u>Case 1</u>	<u>Case 2</u>
$M_\infty = 1.398$	$M_\infty = 1.70$
$P_{t,\infty}^* = 9.21 \times 10^2 \text{ lb/ft}^2$	$P_{t,\infty}^* = 9.92 \times 10^2 \text{ lb/ft}^2$
$T_{t,\infty}^* = 5.36 \times 10^2 \text{ }^\circ\text{R}$	$T_{t,\infty}^* = 5.36 \times 10^2 \text{ }^\circ\text{R}$
$\frac{T_w^*}{T_{t,\infty}^*} = 9.76 \times 10^{-1}$	$\frac{T_w^*}{T_{t,\infty}^*} = 9.71 \times 10^{-1}$

The experimental Mach number distributions are presented in figure 14(b). The edge Mach number distribution was used as an input to the digital computer program instead of P_e^* . Equations (7.131) to (7.134) and (7.31) were used to calculate the required edge conditions from the specified edge Mach number distribution. The initial conditions behind the conical shock wave were obtained from reference 105.

The initial profiles required to start the finite difference solution were obtained by an exact solution of the similar boundary-layer equations (eqs. (A-47) to (A-49)) at $x = 0$. Transition was



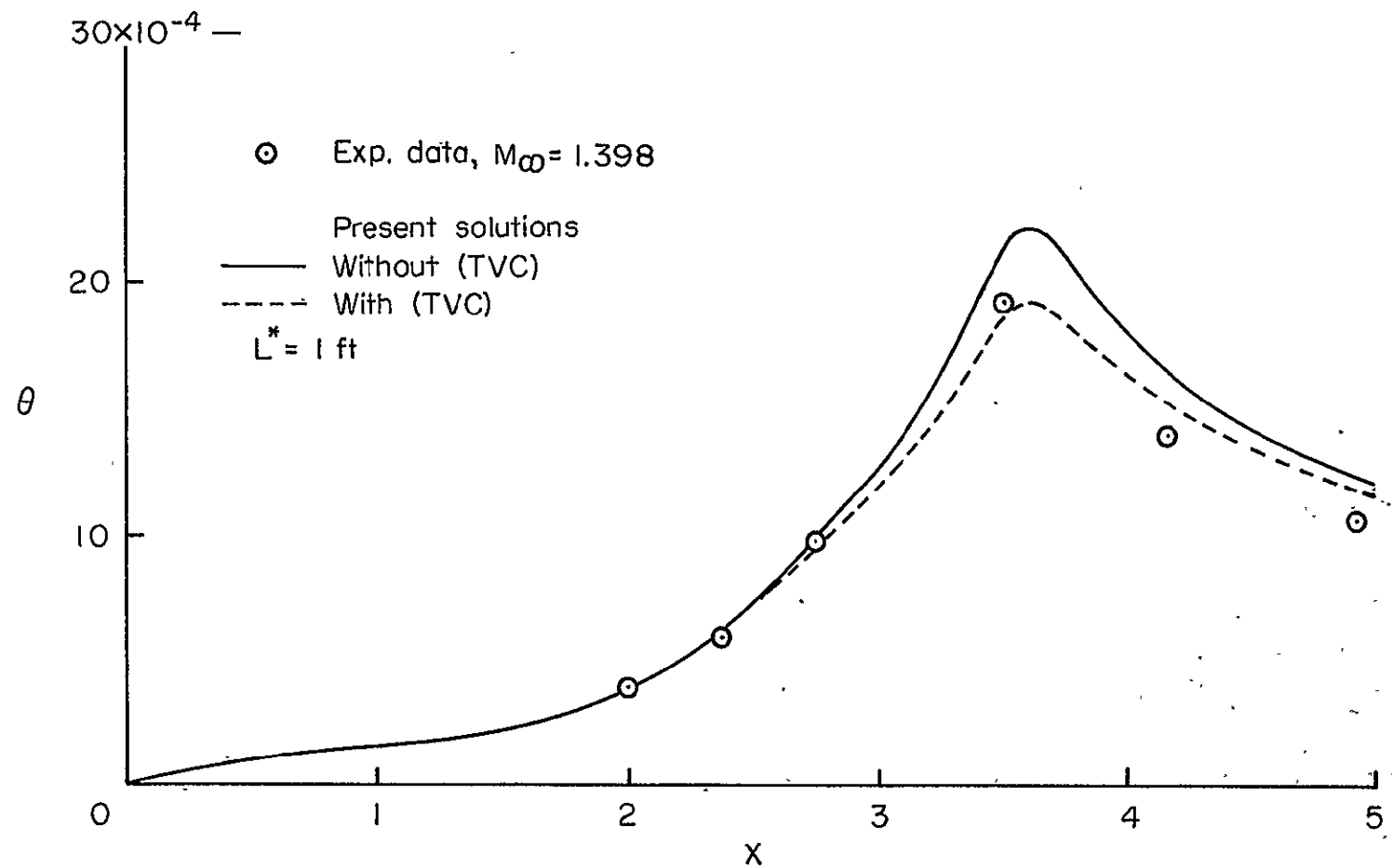
(b) Experimental edge Mach number distribution.

Figure 14.- Continued.

initiated at the solution station, $x_{t,i}$, where x'_{max} achieved a value of 2,500. The transition extent was then automatically computed from equation (7.87). The grid-point spacing in the ξ -direction varied from a maximum Δx value of 0.01 to a minimum value of 0.001 in the regions of large pressure gradients. Variable grid-point spacing in the η -direction was required with a K value of 1.04. Calculations were made for K values of 1.03 and 1.05 to insure convergence. The computer processing time per test case was approximately 4 minutes.

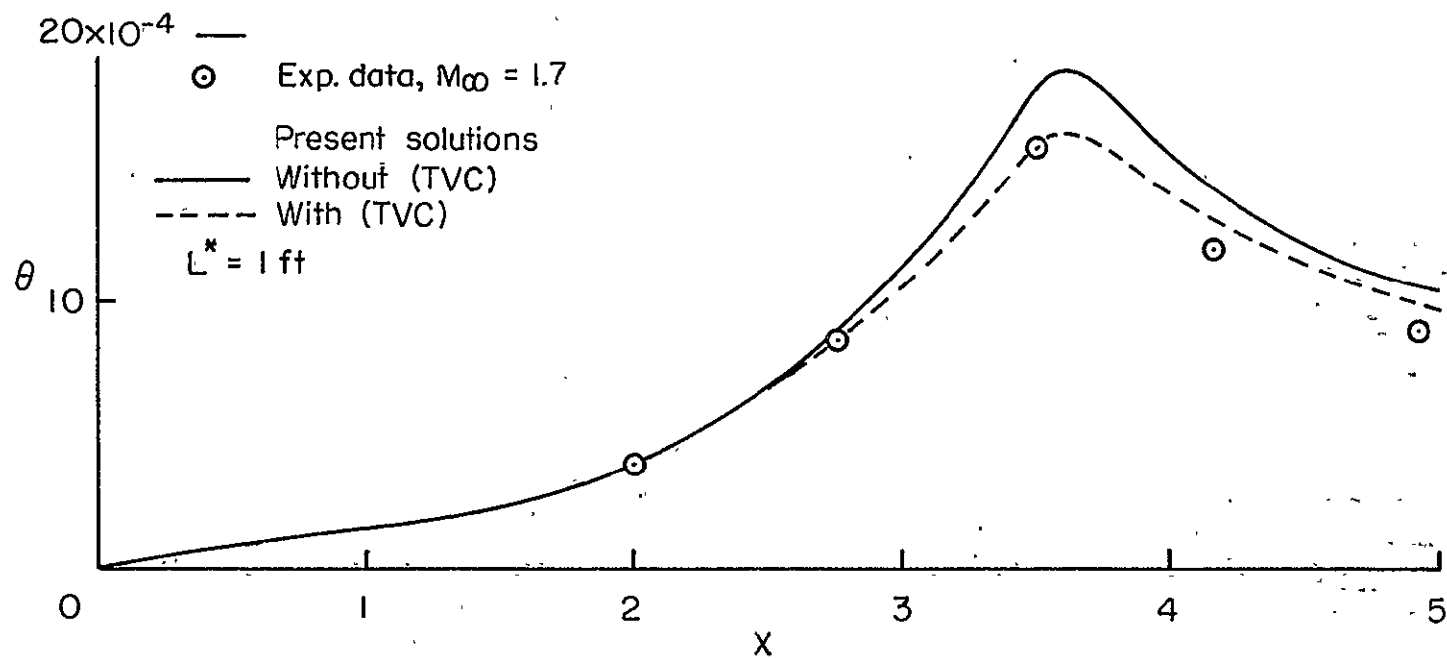
The numerical results are compared with the experimental data for momentum thickness and skin friction coefficient distributions in figures 14(c) to 14(f).

The agreement between the numerical and experimental momentum thickness and skin friction coefficient distributions is very good for both test cases. In particular, note the agreement with the minimum C_{f_e} data point in transition (fig. 14(f)) and the erratic behavior of the data in the region $x \leq 1$ (figs. 14(e) and 14(f)). It is also of interest to note that while the solutions with transverse curvature were in closest agreement with the θ values for $x < 3.5$, the solutions without transverse curvature agreed best with the C_{f_e} values in the same region. A similar trend is presented in reference 78.



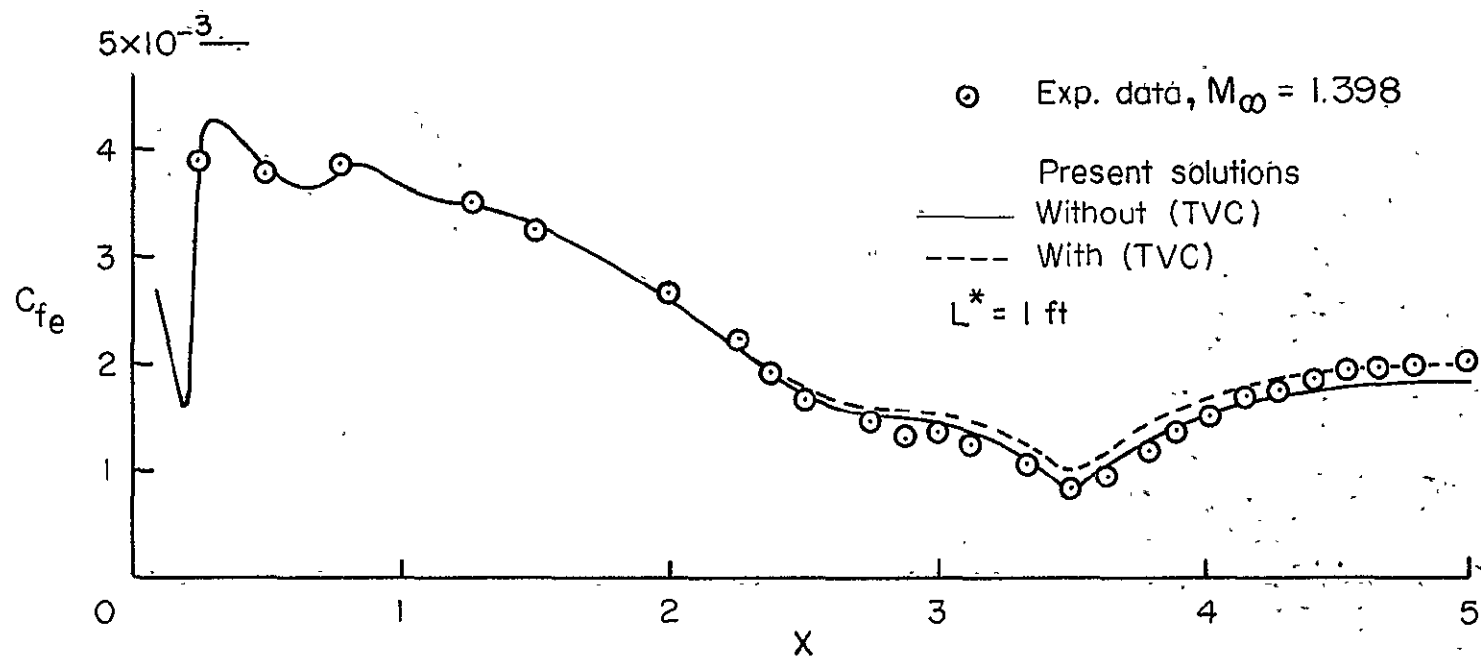
(c) Momentum thickness for $M_\infty = 1.398$.

Figure 14.- Continued.



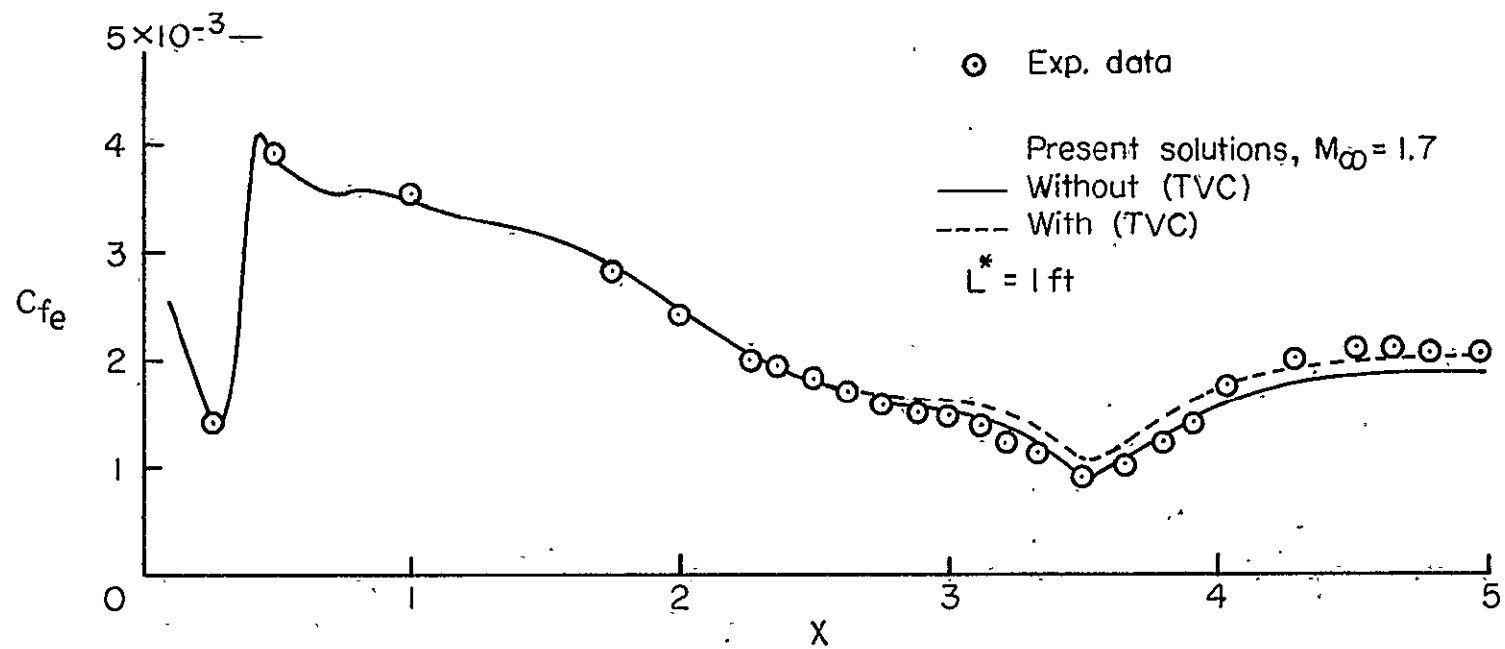
(d) Momentum thickness for $M_\infty = 1.7$.

Figure 14.- Continued.



(e) Skin friction coefficient for $M_\infty = 1.398$.

Figure 14.- Continued.



(f) Skin friction coefficient for $M_{\infty} = 1.7$.

Figure 14.- Concluded.

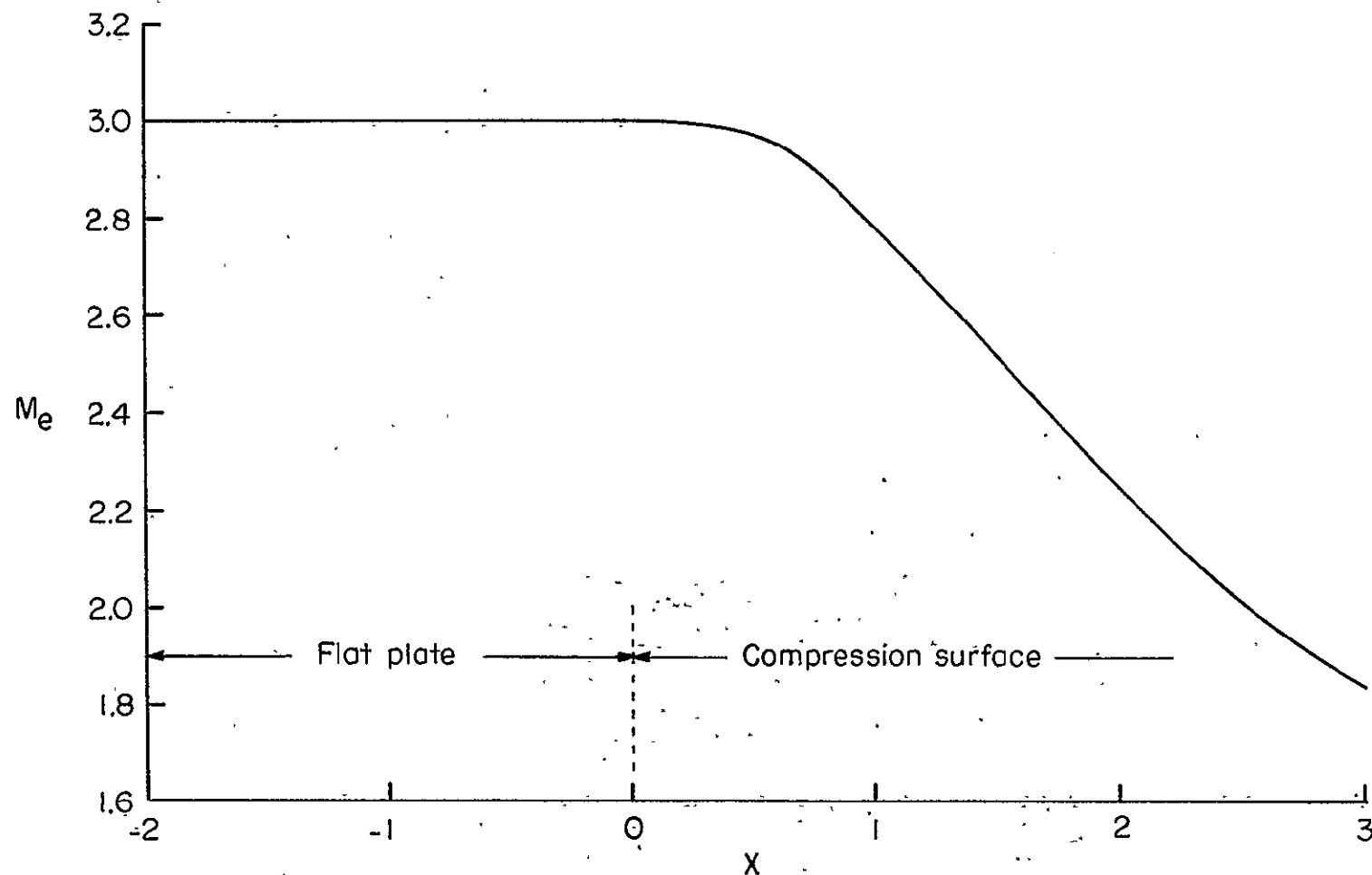
9.6 Adverse Pressure Gradient Turbulent Flow

The design engineer is often required to make estimates of the skin friction, heating rate, and other boundary-layer characteristics for turbulent boundary-layer flows in adverse pressure gradient regions. Good examples of such flows would be the boundary layer over a deflected control surface (compression surface) and over the centerbody of a supersonic engine inlet. An example of turbulent data obtained in an adverse pressure gradient is presented by McLafferty and Barber (ref. 106). One of the test configurations was a flat plate with a single-radius curvature compression surface at the rear of the plate. The test conditions were as follows:

$$\begin{aligned} M_{\infty} &= 3.0 & T_{t,\infty}^* &= 6.10 \times 10^2 \text{ } ^\circ\text{R} \\ P_{t,\infty}^* &= 2.116 \times 10^3 \text{ lb/ft}^2 & \frac{T_w^*}{T_{t,\infty}^*} &= 9.28 \times 10^{-1} \end{aligned}$$

For this particular example the pressure gradient across the boundary layer was significant. However, for the present numerical calculations, this factor was neglected since the system of equations as used herein does not contain the y-momentum equation. The experimental Mach number at the edge of the boundary layer was used to obtain the required edge conditions. This distribution is presented in figure 15(a). The station $x = 0$ marks the beginning of the compression surface. No experimental measurements of the skin friction were made.

For the present solution the calculated momentum thickness Reynolds number at the beginning of the compression, $x = 0$, was

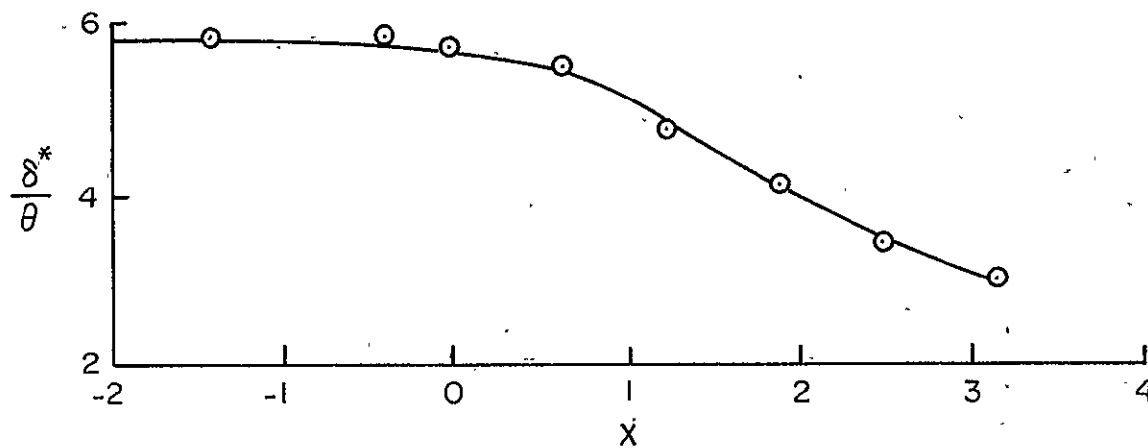
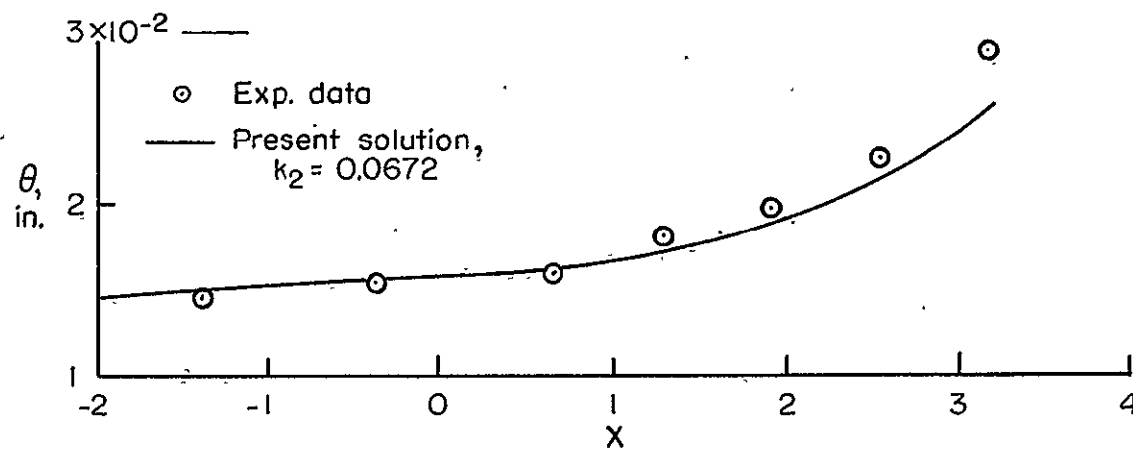


(a) Experimental Mach number distribution.

Figure 15.- Comparisons to experimental data for adverse pressure gradient supersonic turbulent flow.

matched to the experimental value of $Re_\theta = 2,540$. Equally spaced x-solution stations were used; $\Delta x = 0.001$. The total number of grid points in the η -direction and the grid-point spacing parameter K were assigned values of 201 and 1.04, respectively. The computer processing time was approximately 2 minutes. For this particular test case it was necessary to increase the value of K_2 from 0.0168 to 0.0672 in the outer region eddy viscosity model. This increase in K_2 was necessary in order to obtain attached flow throughout the compression. It should be noted that this particular example is the only case in the present paper where the value of K_2 is different from that given in Section 7.4.1; that is, $K_2 = 0.0168$. The numerical solution results for momentum thickness and form factor are presented in figure 15(b). The calculated momentum thickness distribution agrees well with the experimental data for $-2 \leq x \leq 0.5$; however, the numerical results fall somewhat below the data throughout the remaining compression. The agreement between the solution and the experimental form factor distribution is good throughout the compression.

The eddy viscosity model as used herein (see Section 7.4) was developed from data obtained in zero pressure gradient flows. The effect of streamline curvature has been studied by Bradshaw (ref. 107). Bradshaw found that streamline curvature (centrifugal effects) had a strong effect on the turbulence structure for flow geometries where the ratio of the boundary-layer thickness to the radius of curvature of the body surface was on the order of $1/300$. For concave streamlines, such



(b) Comparisons to experimental momentum thickness and form factor distributions.

Figure 15.- Concluded.

as in the present case, it was shown (ref. 107) that the mixing length should be increased in order to account for the effect of curvature on the turbulence structure.

This particular test case has also been studied by Beckwith (ref. 14). Beckwith avoided separation in his solutions by computing the velocity gradient, du_e/dx , from the static pressure distribution at the edge of the boundary layer, P_e , rather than P_w , as used in the present solution; however, u_e and ρ_e were calculated from P_w as in the present solution. It should be recalled that separation was avoided in the present solution by increasing the eddy viscosity in the outer region. It was suggested in reference 14 that the premature separation problem should be corrected by the inclusion of the y-momentum equation and that more data should be obtained in adverse pressure gradient flows in order to develop appropriate mixing length or eddy viscosity models.

9.7 Flow Over Sharp-Tipped Cones

Fisher (ref. 56) studied the effect of the unit Reynolds number, R_e^* , on transition for a 10° half-angle cone at a free-stream Mach number of 7. These data provide an excellent case for comparison as well as to exhibit the flexibility of the digital computer program. The test conditions were as follows:

$$M_{\infty} = 7$$

$$P_{t,\infty}^* = 2.89 \times 10^4 \text{ to } 8.77 \times 10^4 \text{ lb/ft}^2$$

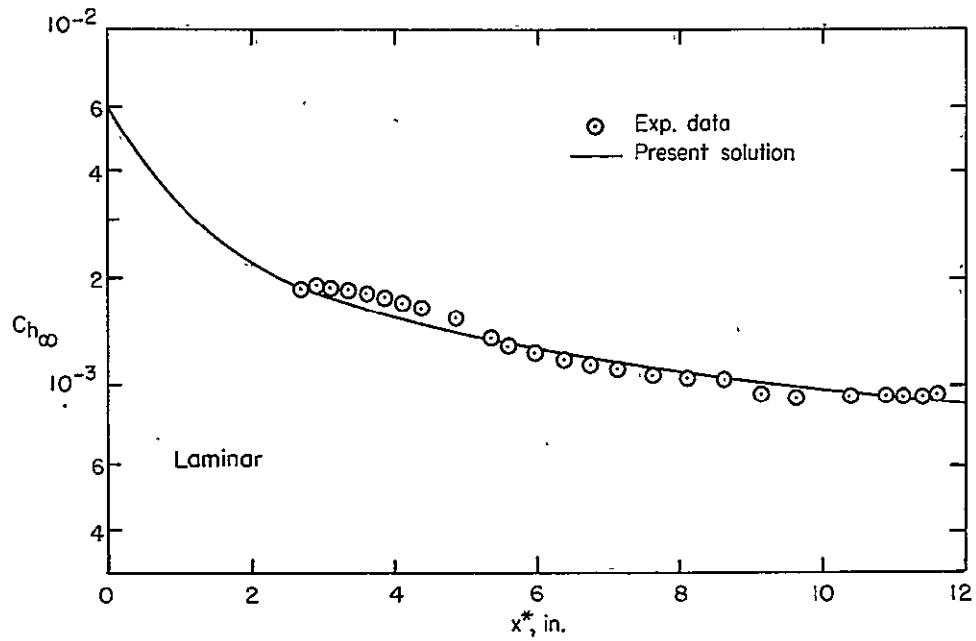
$$T_{t,\infty}^* \cong 1.03 \times 10^3 \text{ } ^\circ\text{R}$$

$$\frac{T_w^*}{T_{t,\infty}^*} \cong 5.2 \times 10^{-1}$$

The boundary-layer edge values were obtained from reference 105. The experimental location of transition and the extent of transition were used in the numerical calculations. The computer processing time per test case was approximately 2 minutes.

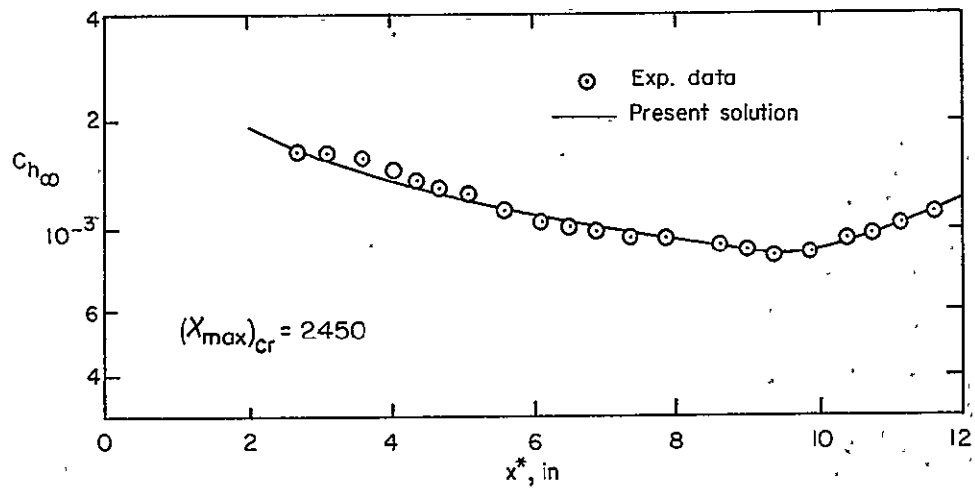
Comparisons of the numerical results to the experimental Stanton number distributions are presented in figures 16(a) through 16(f). The value of $(X_{\max})_{cr}$ is noted on each figure. The agreement between the numerical results and the experimental data is very good for all six test cases. In particular, note that the numerical solution predicted the correct peak heating and overshoot characteristics of the two highest unit Reynolds number cases (see figs. 16(e) and 16(f)).

Two cases similar to the above ones are presented in figures 16(g) and 16(h). These data were obtained by P. Calvin Stainback (unpublished) at the Langley Research Center on a 10° sharp cone model. The test conditions for these data were as follows:



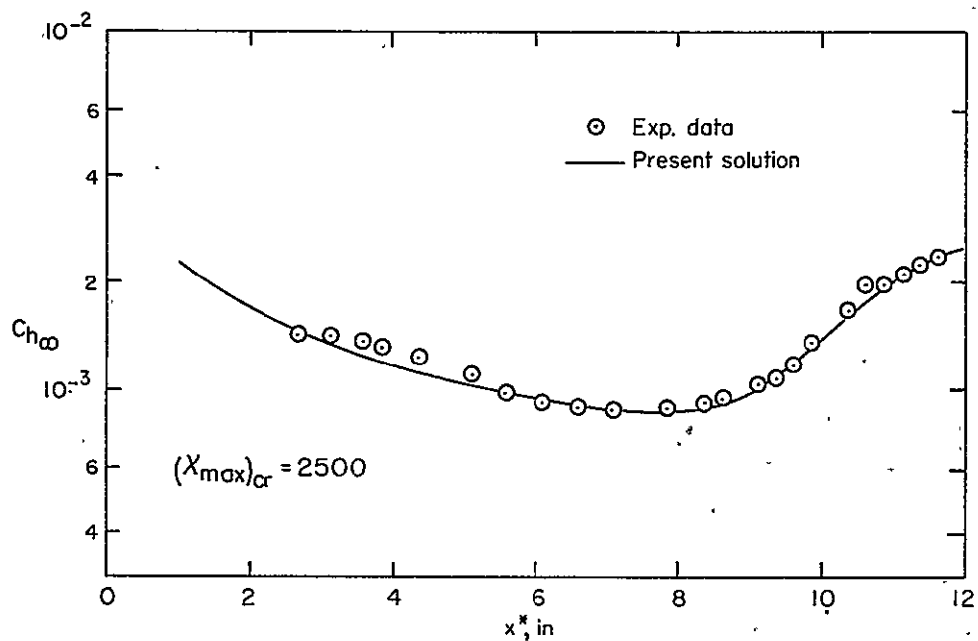
$$(a) \quad M_\infty = 7, \quad R_e^* = 3.00 \times 10^6.$$

Figure 16.- Comparisons with experimental Stanton number distributions for hypersonic flow over sharp-tipped cones.



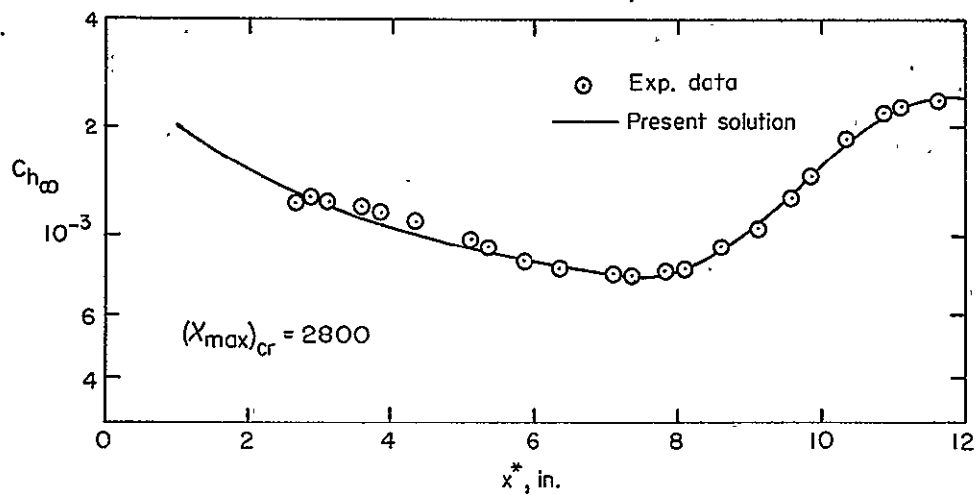
$$(b) \quad M_\infty = 7, \quad R_e^* = 3.94 \times 10^6.$$

Figure 16.- Continued.



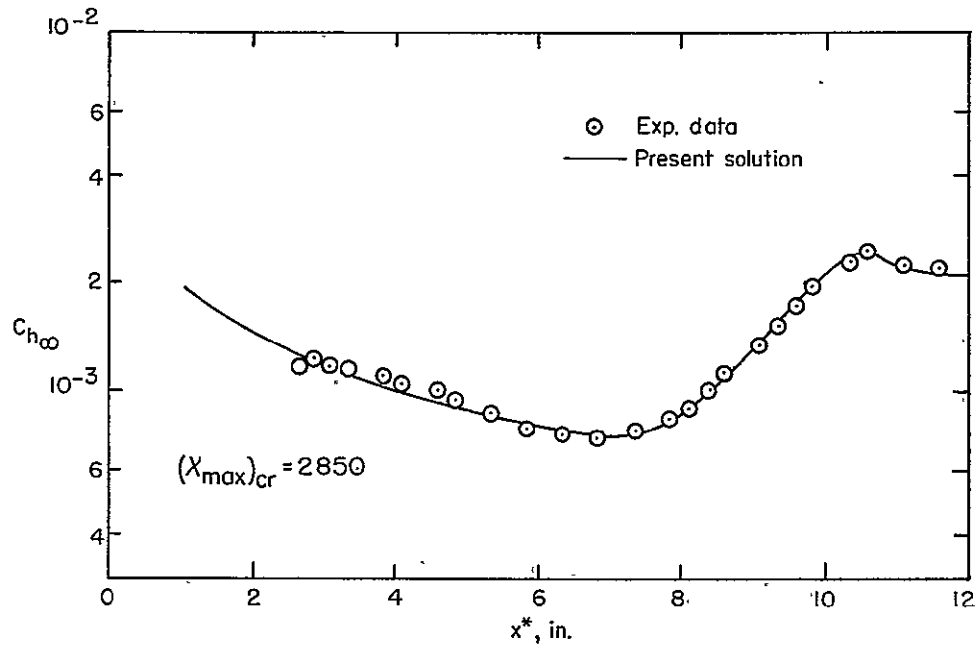
(c) $M_w = 7$, $R_e^* = 5.30 \times 10^6$.

Figure 16.- Continued.



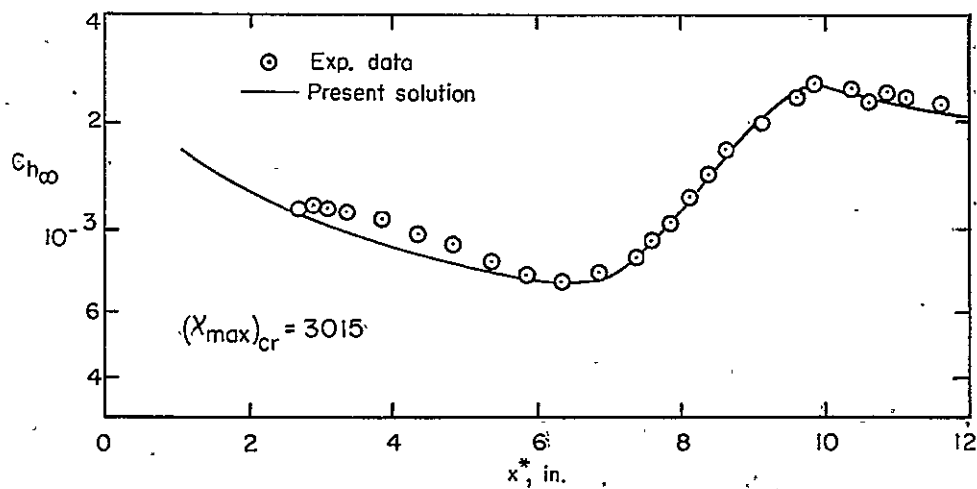
(d) $M_w = 7$, $R_e^* = 6.69 \times 10^6$.

Figure 16.- Continued.



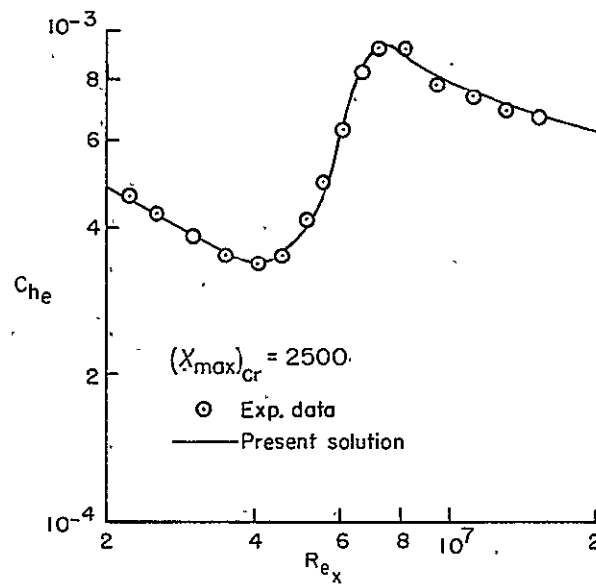
(e) $M_{\infty} = 7$, $Re^* = 7.48 \times 10^6$.

Figure 16.- Continued.



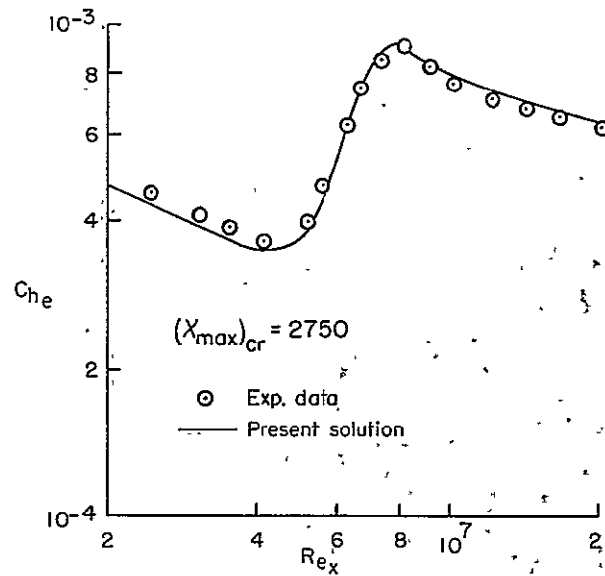
(f) $M_{\infty} = 7$, $Re^* = 9.18 \times 10^6$.

Figure 16.- Continued.



(g) $M_{\infty} = 8$, $R_e^* = 12.50 \times 10^6$.

Figure 16.- Continued.



(h) $M_{\infty} = 8$, $R_e^* = 17.20 \times 10^6$.

Figure 16.- Concluded.

Case 1

$$M_{\infty} = 8$$

$$P_{t,\infty}^* = 2.91 \times 10^5 \text{ lb/ft}^2$$

$$T_{t,\infty}^* = 1.458 \times 10^3 \text{ } ^\circ\text{R}$$

$$\frac{T_w^*}{T_{t,\infty}^*} = 4.0 \times 10^{-1}$$

Case 2

$$M_{\infty} = 8$$

$$P_{t,\infty}^* = 3.63 \times 10^5 \text{ lb/ft}^2$$

$$T_{t,\infty}^* = 1.367 \times 10^3 \text{ } ^\circ\text{R}$$

$$\frac{T_w^*}{T_{t,\infty}^*} = 4.2 \times 10^{-1}$$

These two cases are typical of approximately 15 cases calculated by the author from the same source. Results from these remaining cases will be presented in a future publication. They are presented herein because of the length of turbulent flow in relation to that obtained by Fisher (ref. 56). The $(x_{\max})_{cr}$ value is indicated on the figures. The agreement in the peak heating region is excellent; in particular, note the overshoot characteristic and its agreement with the data.

9.8 Flow Over Planar Surfaces

O'Donnel (ref. 108) studied laminar, transitional, and turbulent boundary-layer flows over a hollow cylinder. Velocity profiles were measured at various stations along the cylinder. The test conditions were as follows:

$$M_{\infty} = 2.41$$

$$P_{t,\infty}^* = 4.95 \times 10^2 \text{ to } 8.49 \times 10^3 \text{ lb/ft}^2$$

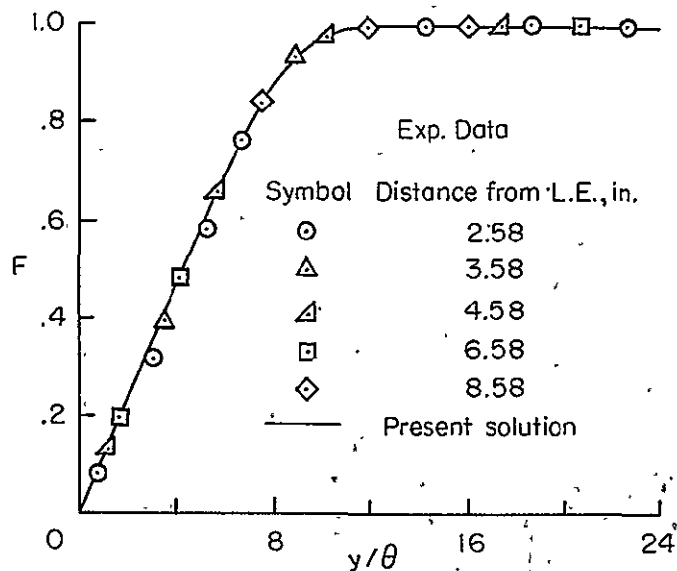
$$T_{t,\infty}^* = 5.60 \times 10^2 \text{ } ^\circ\text{R}$$

$$\frac{T_w^*}{T_{t,\infty}^*} = 9. \times 10^{-1}$$

For this particular set of calculations, the experimental transition location was utilized; however, the extent of transition was calculated from equation (7.85). Consequently, the only variable inputs to the computer program were the specific values of the total pressure, $P_{t,\infty}^*$, and the transition location, $x_{t,i}$.

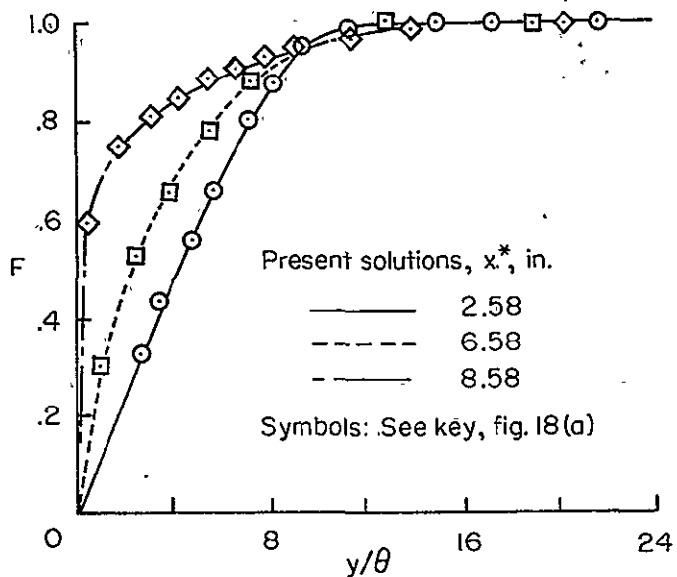
The velocity profile comparisons are presented in figures 17(a) through 17(e). For a unit Reynolds number of 0.672×10^6 , the boundary layer was laminar throughout the measured area. The velocity profiles are similar and the agreement between the numerical results and experimental data is very good (see fig. 17(a)). For a unit Reynolds number of 2.88×10^6 , laminar, transitional, and turbulent flow occurred (see fig. 17(b)). Similar results were obtained for a unit Reynolds number of 5.76×10^6 (see fig. 17(c)). For unit Reynolds numbers of 8.64×10^6 and 11.5×10^6 , the flow was turbulent as presented in figure 17(d) and 17(e), respectively. The profiles are seen to be similar for the turbulent region. Comparisons with the experimental momentum thicknesses are presented in figure 17(f). The agreement is seen to be excellent over the entire unit Reynolds number range.

A further example of laminar and transitional boundary-layer flow for hypersonic test conditions is presented in figure 18.



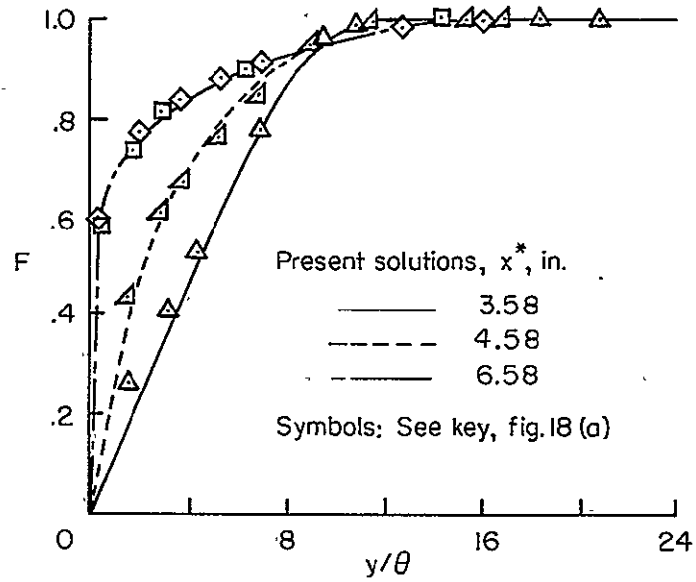
(a) $R_e^* = 0.672 \times 10^6$.

Figure 17.- Comparisons with velocity profile data and momentum thickness for laminar, transitional, and turbulent flow over a hollow cylinder at $M_\infty = 2.41$.



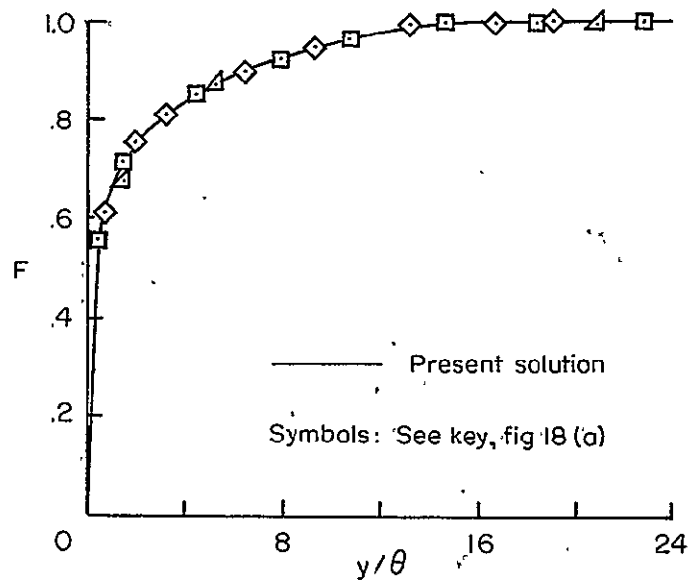
(b) $R_e^* = 2.88 \times 10^6$.

Figure 17.- Continued.



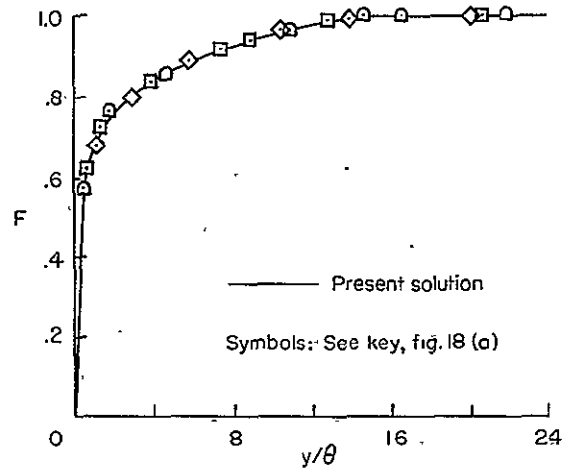
(c) $R_e^* = 5.76 \times 10^6$.

Figure 17.- Continued.



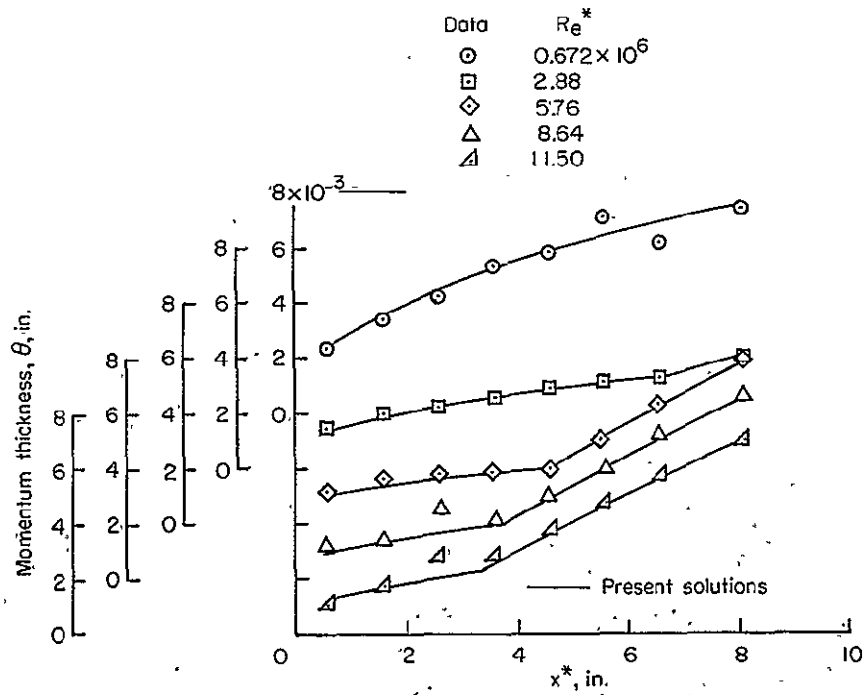
(d) $R_e^* = 8.64 \times 10^6$.

Figure 17.- Continued.



(e) $Re^* = 11.50 \times 10^6$.

Figure 17.- Continued.



(f) Momentum thickness.

Figure 17.- Concluded.

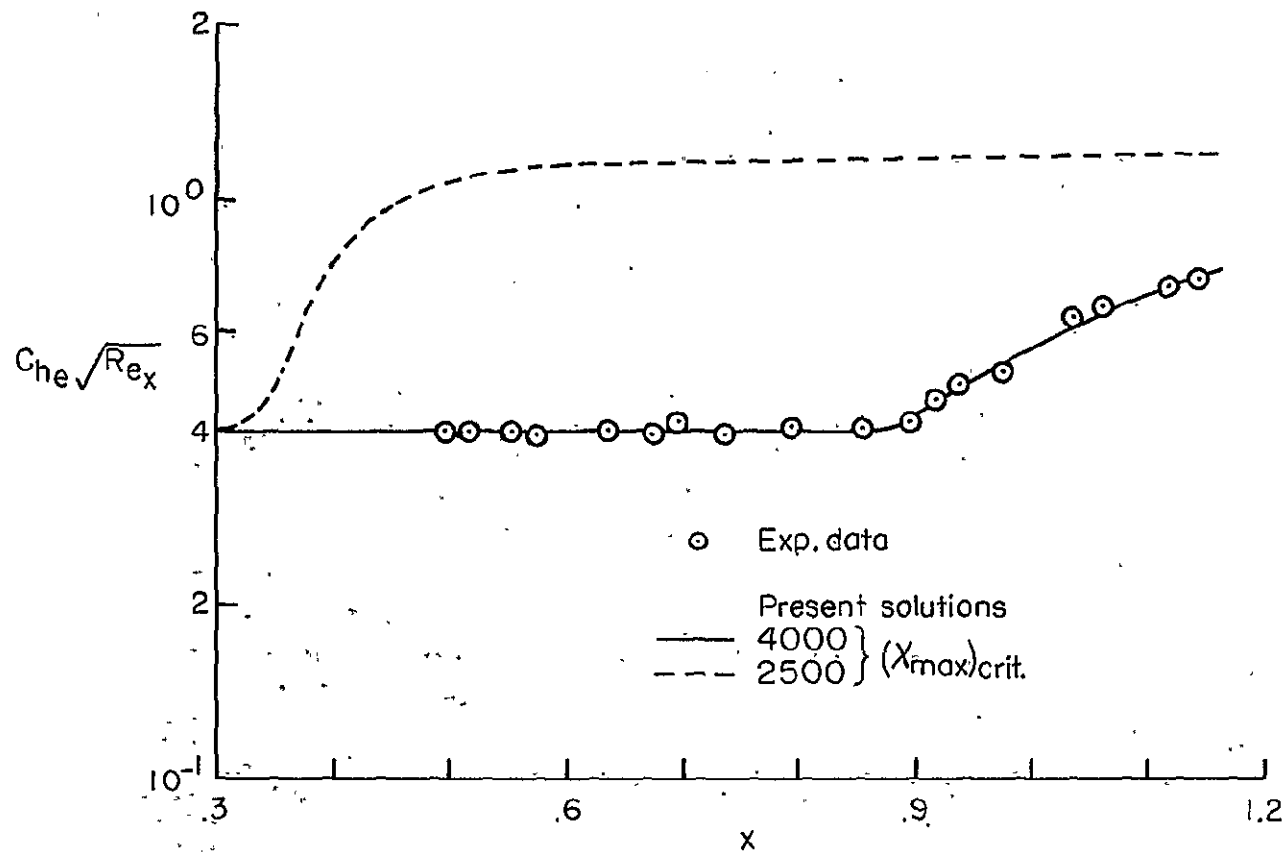


Figure 18.- Comparison with experimental data for laminar and transitional flat plate flow at $M_\infty = 7.8$.

These data were obtained by Johnson (ref. 109) on a sharp leading-edge flat plate model. The experimental test conditions were as follows:

$$M_{\infty} = 7.8$$

$$P_{t,\infty}^* = 8.827 \times 10^4 \text{ lb/ft}^2$$

$$T_{t,\infty}^* = 1.43 \times 10^3 \text{ } ^\circ\text{R}$$

$$\frac{T_w^*}{T_{t,\infty}^*} = 3.88 \times 10^{-1}$$

The agreement between the numerical results and the experimental Stanton number distribution is very good.

The experimental transition location, $x_{t,i}^*$, was used in the calculation; however, the transition extent was calculated from equation (7.87). (Note that the transition from laminar to turbulent flow was not completed; that is, $x_{t,f}^*$ was not reached.) The total number of grid points in the η -direction and the grid-point spacing parameter, K , were assigned values of 201 and 1.04, respectively. The computer processing time was approximately 2 minutes.

This particular test case is presented to emphasize that the stability index, $(X_{\max})_{cr}$ is not an invariant as suggested by Rouse (ref. 64) but is, in fact, a strong function of the unit Reynolds number, R_e^* . For all of the previous test cases, $(X_{\max})_{cr}$ has varied over a relatively small range $2,500 \leq (X_{\max})_{cr} \leq 3,000$ which might lead one to assume that, while not invariant, $(X_{\max})_{cr}$ varies only slightly. However, the present test case value of 4,000

considerably extends this range from 2,500 to 4,000. The numerical results obtained by assuming that transition would occur at the x-station where X_{\max} was equal to 2,500 is shown on figure 18. This calculation clearly indicates that no assumptions concerning the location of experimental transition should be made on the basis of the magnitude of the stability index as being an invariant or a near constant.

The stability index is presented as a function of unit Reynolds number for a number of experimental studies in figure 19. These values were generated by obtaining the boundary-layer solutions corresponding to the experimental test conditions and plotting the value of X_{\max} at the experimental transition location as a function of the unit Reynolds number of the experiment. Some of these cases have been presented as test cases in the present paper (refs. 109, 56, 108, and two Stainback cases). A number of points of interest concerning the stability index are apparent in figure 19. For example, these data can be represented by the general equation

$$(X_{\max})_{cr} = \Omega_4 \log_{10} R_e^* + \Omega_5 \quad (9.1)$$

where Ω_4 and Ω_5 represent functional relations of the transition parameter phase space. It should be noted at this point that all of the data presented on figure 19 represent similar boundary-layer flows and that nonsimilar effects such as pressure gradients might considerably alter these trends.

Symbol	Geometry	Me	T_w/T_t	Ref.
\odot	Flat plate	4.9	0.3 to 0.6	62
\square	↓	6.0	0.2 to 0.6	62
\triangle		7.8	0.39	109
\diamond	5° cone	10.7	0.17	110
—	10° cone	6.0	0.39	Stainback
---	10° cone	5.5	0.4	56
- - -	Cylinder	2.4	0.9	108

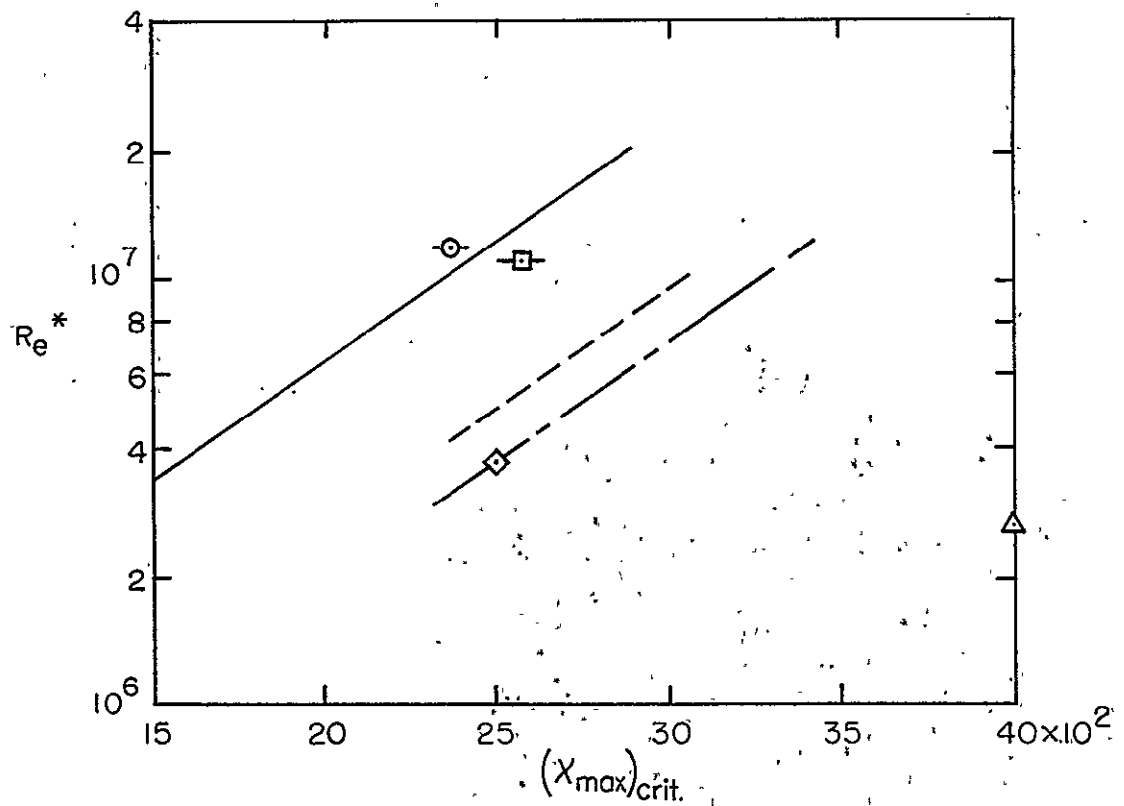


Figure 19.- Stability index as function of unit Reynolds number.

The limited experimental data presented on figure 19 indicate that Ω_4 is invariant, at least, for similar flows since the slopes of the curves for the data from references 56, 108, and the data from Stainback are identical. However, the coefficient Ω_5 is definitely not an invariant for these data. The data from reference 56 and Stainback (unpublished) were obtained at nearly equal edge and wall boundary conditions; however, the value of Ω_5 is considerably different. This suggests that Ω_5 is a strong function of the test environment since the data were obtained in different wind-tunnel test facilities; that is, perhaps the acoustic environment would appear in Ω_5 . The data presented for the adiabatic cylinder (ref. 108) exhibits the same dependence on Ω_4 as that of reference 56 and Stainback (unpublished); however, since these data were obtained for adiabatic wall conditions and at a much lower Mach number than that for the 10° sharp cone, Ω_5 would appear to be a function of at least M_e , T_w/T_e , and the test environment. The test environment would include the effect of acoustic radiation, free-stream turbulence, and temperature spottiness of the flow.

The author is currently studying transition data obtained over a broad range of test conditions for both similar and highly nonsimilar flows. The basic approach being followed is simple in concept; that is, obtain highly accurate boundary-layer solutions using the present solution technique for the test conditions under which the experimental data were obtained. However, while simple in concept, the process is quite lengthy since care must be exercised in the selection of the

test cases. It is important that only well-documented data be studied in which the local test conditions as well as the test environment are carefully reported. This represents a problem in itself since in much of the currently existing transition data no attempt was made by the experimenter to measure the basic characteristics of the test facility in which the data were obtained (test environment). The eventual goal of this study is to obtain not only more transition correlations but also more insight into the actual transition process.

X. DISCUSSION AND CONCLUSIONS

A system of equations which describe the laminar, transitional, and turbulent compressible boundary layers for either planar or axisymmetric flows as well as a numerical method by which the system can be accurately solved has been presented.

The transitional boundary layer structure was developed from the point of view of the statistical production and growth of turbulent spots. The passage of these spots over points on the surface results in an alteration of laminar and fully developed turbulent flow. These alternations are described by an intermittency factor which represents the fraction of time any point spends in turbulent flow, or the probability at any given instant of time that a specific point will be engulfed in a turbulent spot. The intermittency factor was used to modify the turbulent transport models developed for fully turbulent flow.

Stability theory and its relation to experimental transition has been briefly reviewed. Experimental transition data were discussed and methods were suggested that should allow reasonable estimates to be made for the most probable location of transition and the extent of the transitional flow region. The primary objective of the present paper was to present a system of equations and a solution technique with which the boundary-layer characteristics could be obtained regardless of whether the flow was laminar, transitional, or turbulent. Consequently, it was necessary to discuss, in some detail, the

transition problem since the location of transition for a particular flow geometry must be either specified from experimental data or calculated from some correlation equation. A complete treatment of the transition problem would be a study in itself that would require many years to complete. The treatment of the transitional flow structure, as used in the analysis, is not exact in the sense of obtaining a system of time-dependent equations from the full Navier-Stokes system, but is instead based upon existing experimental data. A thorough treatment of the transition location and the transitional flow structure still remains as one of the major unsolved problem areas in fluid mechanics. However, the method as presented herein does provide accurate predictions of the mean flow profiles and wall values of heat transfer and skin friction in the transition region. To the best of the author's knowledge, this represents the first time this procedure has been incorporated into a solution technique for the complete non-similar boundary-layer equations.

The turbulent boundary layer was treated by a two-layer concept with appropriate eddy viscosity models being developed for each layer to replace the Reynolds stress terms in the mean turbulent boundary-layer equations. A specifiable static turbulent Prandtl number was used to replace the turbulent heat flux term. A constant turbulent static Prandtl number was utilized. However, any model could be directly employed once developed from experimental data.

The numerical method used to solve the generalized system of equations is a three-point implicit difference scheme for variable

grid-point spacing in both spatial coordinates. The method is self-starting; that is, it requires no experimental data input. The method has been found to be highly efficient with regard to flexibility, digital computer processing time, and accuracy. The method is inherently stable; that is, no constraint is placed on the grid-point spacing by a step size stability parameter such as in the case of explicit finite difference schemes. However, the grid-point spacing is restricted by the maximum truncation error that can be accepted for a given test case. To the best of the author's knowledge, this represents the first time this particular solution technique has been applied to transitional and turbulent boundary-layer flows.

A number of test cases have been presented and compared with experimental data for supersonic and hypersonic flows over planar and axisymmetric geometries. These test cases have included laminar, transitional, and turbulent boundary-layer flows with both favorable and mild adverse pressure gradient histories as well as a case of highly adverse pressure gradient flow. Mass injection at the wall and transverse curvature effects were also considered. The agreement between the numerical results and the experimental data was very good for all of the test cases considered with the exception of the case for high adverse pressure gradient turbulent flow. The agreement for this particular case was fair; however, much more work needs to be done in this particular area. In particular, for adverse pressure gradient flows approaching separation, the normal momentum equation must be included in the governing system of equations. There is also a current

need for well-documented experimental data for transitional and turbulent boundary-layer flows with pressure gradient histories. These data are needed to develop mixing length and eddy viscosity models for pressure gradient flows. One of the more important parameters that should be measured is the intermittency as a function of both spatial coordinates. One of the main advantages of the present numerical method is the conceptual simplicity that can be utilized in the formulation of the turbulent flux terms. (This advantage would be true for all implicit finite difference techniques.) This advantage allows the use of "numerical experimentation" through which mixing length and eddy viscosity models may be efficiently studied in relation to experimental data. Through this "numerical experimentation" procedure the knowledge of basic turbulent mechanisms could ultimately be improved. However, well-documented data must be available for this process to be successful.

In concluding, it has been shown that the system of equations presented herein and the solution technique by which they are solved can be used to obtain accurate solutions for laminar, transitional, and turbulent compressible boundary-layer flows.

XI. REFERENCES

1. Prandtl, L.: Über Flüssigkeitsbewegung bei sehr Kleiner reibung. Verhandlgndes III. Internat. Math-Kongr., Heidelberg, 1904.
2. Schlichting, Hermann: Boundary-Layer Theory. McGraw-Hill Book Company, Inc., 1968.
3. Moore, F. K., ed.: Theory of Laminar Flows. Vol. IV, High Speed Aerodynamics and Jet Propulsion. Princeton University Press, 1964.
4. Rosenhead, L., ed.: Laminar Boundary Layers. Oxford at the Clarendon Press, 1963.
5. Dewey, Forbes C., Jr.; and Gross, Joseph F.: Exact Similar Solutions of the Laminar Boundary-Layer Equations. Memorandum RM-5089-ARPA, The Rand Corporation, July 1967.
6. Blottner, F. G.: Finite Difference Methods of Solution of the Boundary-Layer Equations. AIAA Journal, vol. 8, no. 2, Feb. 1970, pp. 193-205.
7. Reynolds, O.: An Experimental Investigation of the Circumstances Which Determine Whether The Motion of Water Shall be Direct or Senuous, and of the Law of Resistance in Parallel Channels. Phil. Trans. Roy. Soc. 174, 935-982 (1883), Scientific Papers 2, 51.
8. Săvulescu, St. N.: Tranzitia de la scurgerea laminara turbulenta. Academy Press of the Socialist Republic Romania, Bucarest, 1968.
9. Morkovin, Mark V.: Critical Evaluation of Transition From Laminar to Turbulent Shear Layers With Emphasis on Hypersonically Traveling Bodies. Air Force Flight Dynamics Laboratory, TR-68-149, 1969.
10. James, C. S.: Observations of Turbulent-Burst Geometry and Growth in Supersonic Flow. NACA TN 4235, 1958.
11. Kline, S. J.; Morkovin, M. V.; Sorran, G.; and Cockrell, D. J., eds.: Computation of Turbulent Boundary Layers. 1968 AFOSR-IFP-Stanford Conference. Vol. I - Methods, Predictions, Evaluation and Flow Structure, August 1968.

12. Coles, D. E.; and Hirst, E. A., eds.: Proceedings - Computations of Turbulent Boundary Layers. 1968 AFOSR-IFP-Stanford Conference. Vol. II, Compiled Data, August 1968.
13. Bertram, Mitchel H.; ed.: Compressible Turbulent Boundary Layers. A Symposium held at the Langley Research Center, Hampton, Virginia, Dec. 10-11, 1968. NASA SP-216.
14. Beckwith, Ivan E.: Recent Advances in Research on Compressible Turbulent Boundary Layers. Paper No. 18 in Analytic Methods in Aircraft Aerodynamics. NASA SP-228, 1970.
15. Flügge-Lotz, I.; and Blottner, F. G.: Computation of the Compressible Laminar Boundary-Layer Flow Including Displacement-Thickness Interaction Using Finite-Difference Methods. Tech. Rep. No. 131, Div. of Eng. Mech., Stanford University, Stanford, California, 1962.
16. Davis, R. T.; and Flügge-Lotz, I.: Laminar Compressible Flow Past Axisymmetric Blunt Bodies (Results of a Second-Order Theory). Tech. Rep. No. 143, Div. of Eng. Mech., Stanford University, Stanford, California, 1963.
17. Lewis, Clark Houston: Comparison of A First-Order Treatment of Higher-Order Boundary-Layer Effects With Second-Order Theory and Experimental Data. AEDC-TR-68-148, 1968.
18. Reynolds, O.: On the Dynamic Theory of Incompressible Viscous Fluids and the Determination of the Criterion. Phil. Trans. Roy. Soc. T. 186 A 123, or Sci. Paper I, 355.
19. Van Driest, E. R.: Turbulent Boundary Layer in Compressible Fluids. J.A.S., vol. 18, no. 3, March 1951.
20. Probststein, R. F.; and Elliott, D.: The Transverse Curvature Effect in Compressible Axially Symmetric Laminar Boundary Layer Flow. J. Aero. Sci., March 1956.
21. Hayes, W. D.; and Probststein, R. F.: Hypersonic Flow Theory. Academic Press, New York and London, 1959, p. 290.
22. Bradshaw, P.: Turbulent Boundary Layers. The Aero. Jour. of Roy. Aero. Soc., vol. 72, May 1968, pp. 451-458.
23. Prandtl, L.: Recent Results of Turbulence Research. NACA TM 720, 1933.

24. Lin, C. C., ed.: Turbulent Flows and Heat Transfer. Vol. 5, High Speed Aerodynamics and Jet Propulsion, Princeton University Press, Princeton, New Jersey, 1959.
25. Prandtl, L.: Über die ausgebildete Turbulenz. ZAMM 5, 136-139 (1925) and Proc. 2nd Intern. Congr. Appl. Mech., Zürich, 1926, 62-75; also Coll. Works.
26. Van Driest, E. R.: On Turbulent Flow Near a Wall. J. of Aero. Sci., vol. 23, no. 11, Nov. 1956.
27. Stokes, G. G.: On the Effect of the Internal Friction of Fluids on the Motion of Pendulums. Cambr. Phil. Trans. IX, 8 (1851); Math. and Phys. Papers, III, 1-141, Cambridge, 1901.
28. Rayleigh, Lord: On the Motion of Solid Bodies Through Viscous Liquid. Phil. Mag. 21, 697-711, 1911; also Sci. Papers, VI, 29.
29. Cebeci, Tuncer: The Behavior of Turbulent Flow Near a Porous Wall With Pressure Gradient. McDonnell Douglas, Rep. No. DAC 70014, 1969.
30. Patankar, S. V.; and Spalding, D. B.: Heat and Mass Transfer in Boundary Layers. C.R.C. Press, Cleveland, 1968.
31. Bushnell, D. M.; and Beckwith, I. E.: Calculation of Nonequilibrium Hypersonic Turbulent Boundary Layers and Comparisons With Experimental Data. AIAA Paper No. 69-684, AIAA Fluid and Plasma Dynamics Conference, San Francisco, California, June 16-18, 1969.
32. Clauser, F. H.: The Turbulent Boundary Layer. Advances in Applied Mechanics, Vol. IV, Academic Press, Inc., 1956.
33. Maise, George; and McDonald, Henry: Mixing Length and Kinematic Eddy Viscosity in a Compressible Boundary Layer. AIAA Journal, vol. 6, no. 1, Jan. 1968, pp. 73-80.
34. Morkovin, M. V.: Effects of Compressibility on Turbulent Flows. International Symposium on the Mecanique de la Turbulence, Centre National de la Recherche Scientifique, Paris, 1962, pp. 367-380.
35. Matsui, T.: Mean Velocity Distribution in the Outer Layer of a Turbulent Boundary Layer. Research Rep. 42, Aerophysics Dept., Mississippi State, Conducted under Contract No. 978(03), Jan. 1963.

36. Klebanoff, P. S.: Characteristics of Turbulence in a Boundary Layer With Zero Pressure Gradient. NACA TN 3178, July 1954.
37. Kestin, J.; and Richardson, P. D.: Heat Transfer Across Turbulent Incompressible Boundary Layers. The Mechanics of Turbulence, Gordon and Breach, 1964, pp. 409-418.
38. Johnson, Donald S.: Turbulent Heat Transfer in a Boundary Layer With Discontinuous Wall Temperature. OSR Tech. Note 55-289, Dept. of Aeronautics, The Johns Hopkins University, August 1955.
39. Rochelle, William C.: Prandtl Number Distribution in a Turbulent Boundary Layer With Heat Transfer at Supersonic Speeds. DRL-508, Defense Research Laboratory, The University of Texas, Oct. 1963.
40. Rotta, J. C.: Heat Transfer and Temperature Distribution in Turbulent Boundary Layers at Supersonic and Hypersonic Flows. AGARDograph 97, Recent Developments in Boundary Layer Research, Part I, May 1965, pp. 41-63.
41. Taylor, G. I.: Statistical Theory of Turbulence, V - Effect of Turbulence on Boundary Layer. Proc. Roy. Soc. (London), Series A, vol. 156, 1936, p. 307.
42. Schubauer, G. B.; and Skramstad, H. K.: Laminar-Boundary-Layer Oscillations and Transition on a Flat Plate. NACA Adv. Conf. Rept., April 1943, later published as Rept. No. 909.
43. Lin, C. C.: On the Stability of Two-Dimensional Parallel Flows. Parts I, II, and III. Quart. Appl. Math. 3, 1945, pp. 117-142; 218-234; 277-301.
44. Lin, C. C.: Theory of Hydrodynamic Stability. Cambridge Univ. Press, London, 1955.
45. Klebanoff, P. S.; Tidstrom, K. D.; and Sargent, L. M.: The Three-Dimensional Nature of Boundary-Layer Instability. Jour. Fluid Mech. 12, Pt. 1, 1962, pp. 1-34.
46. Emmons, H. W.: The Laminar-Turbulent Transition in a Boundary Layer. Part I., Jour. Aero. Sci., vol. 18, July 1951, p. 490.
47. Emmons, H. W.; and Mitchner, M.: Transition from Laminar to Turbulent Flow in a Thin Film of Water Flowing Down an Inclined Glass Plate. Motion picture, available as item E-2 from Engineering Societies Library, 345 East 47th Street, New York, New York 1952.

48. Klebanoff, P. S.; and Schubauer, G. B.: Contributions on the Mechanics of Boundary-Layer Transition. NACA Report 1289, 1956.
49. Sovran, Gino, ed.: Fluid Mechanics of Internal Flow. Proceedings of the Symposium on the Fluid Mechanics of Internal Flow, General Motors Research Laboratories, Warren, Michigan, 1965. Elsevier Publishing Company, Amsterdam-London-New York, 1967.
50. Tollmien, W.: Über die Entstehung der Turbulenz. Gesellschaft der Wissenschaften. Göttingen, Mathematisch-Naturwissenschaftliche Klasse, Nachrichten, 21-24, 1929.
51. Jaffe, N. A.; Okamura, T. T.; and Smith, A. M. O.: Determination of Spatial Amplification Factors and Their Application to Predicting Transition. AIAA Jour., vol. 8, no. 2, Feb. 1970, pp. 301-308.
52. Shen, S. F.: Stability of Laminar Flows. Theory of Laminar Flows, High Speed Aerodynamics and Jet Propulsion, vol. 4, Section G., Princeton Univ. Press, Princeton, New Jersey, 1954.
53. Reid, W. H.: The Stability of Parallel Flows. Basic Developments in Fluid Dynamics (M. Holt, ed.), vol. I, Academic Press, New York, 1965, pp. 249-307.
54. Drazin, P. G.; and Howard, L. N.: Hydrodynamic Stability of Parallel Flow of Inviscid Fluid. Advances in Applied Mechanics, vol. 9 (G. Kuerti, ed.), Academic Press, New York and London, 1966, pp. 1-89.
55. Mack, Leslie M.: Boundary Layer Stability Theory. Notes prepared for the AIAA Professional Study Series, High-Speed Boundary Layer Stability and Transition, San Francisco, California, June 14-15, 1969.
56. Fischer, Carlton Michael: An Experimental Investigation on Unit Reynolds Number and Bluntness Effects on Boundary-Layer Transition for a 10° Half-Angle Cone at $M_\infty = 7$. M. S. Thesis, Dept. of Mech. Engr., Virginia Polytechnic Institute, Blacksburg, Virginia, 1969.
57. Pate, S. R.; and Schueler, C. J.: Effects of Radiated Aerodynamic Noise on Model Boundary-Layer Transition in Supersonic and Hypersonic Wind Tunnels. AEDC TR 67-236, March 1968.
58. Softley, E. J.; Graber, B. C.; and Zempel, R. E.: Transition of the Hypersonic Boundary Layer on a Cone. General Electric, Missile and Space Division, R67SD39, November 1967.

59. Richards, Bryan E.: Transitional and Turbulent Boundary Layers on a Cold Flat Plate in Hypersonic Flow. The Aeronautical Quarterly, vol. XVIII, Part 3, August 1967, pp. 237-257.
60. Potter, J. L. and Whitfield, J. D.: Boundary Layer Transition Under Hypersonic Conditions. AGARDograph 97, Part 3, 1965.
61. Deem, Ralph E.; and Murphy, James S.: Flat Plate Boundary Layer Transition at Hypersonic Speeds. AIAA Paper No. 65-128, AIAA 2nd Aerospace Sciences Meeting, January 25-27, 1965, New York, New York.
62. Cary, Aubrey M., Jr.: Turbulent Boundary Layer Heat Transfer and Transition Measurements With Extreme Surface Cooling in Hypersonic Flow. M. S. Thesis, Aerospace Engr. Dept., University of Virginia, Charlottesville, Virginia, August 1969.
63. Potter, J. Leith; and Whitfield, Jack D.: Effects of Slight Nose Bluntness and Roughness on Boundary Layer Transition in Supersonic Flows. J. Of Fluid Mech., vol. 12, Part 4, April 1962, pp. 501-535.
64. Rouse, Hunter: A General Stability Index for Flow Near Plane Boundaries. J. Aero. Sci., vol. 12, no. 4, October 1945, pp. 429-431.
65. Van Driest, D. R.; and Blumer, C. B.: Boundary Layer Transition. Freestream Turbulence and Pressure Gradient Effects. AIAA Journal, vol. 1. no. 6, June 1963, pp. 1303-1306.
66. Iverson, H. W.; and Hsu, T. T.: A Local Reynolds Number to Predict Transition from Laminar to Turbulent Flow. Heat Transfer Thermodynamics and Education, McGraw-Hill, New York, pp. 207-212.
67. Stainback, P. Calvin: Use of Rouse's Stability Parameter in Determining the Critical Layer Height of a Laminar Boundary Layer. AIAA Journal, vol. 8, no. 1, January 1970, pp. 173-174.
68. Murphy, J. D.; and Rubesin, M. W.: A Reevaluation of Heat-Transfer Data Obtained in Flight Tests of Heat-Sink Shielded Re-entry Vehicles. Jour. Spacecraft and Rockets, vol. 3, Jan. 1966, p. 53.
69. McCauley, William D., ed.: Boundary Layer Transition Study Group Meeting, Vol. III - Session on Ground Test Transition Data and Correlations. Air Force Report No. BSD-TR-67-213, vol. III, 1967.

70. McCauley, William D., ed.: Boundary Layer Transition Study Group Meeting, Volume I - Opening Remarks, Keynote Address, Session on Flight Test Transition Data and Correlations. Air Force Report No. BSD-TR-67-213, vol. I, 1967.
71. McCauley, William D., ed.: Boundary Layer Transition Study Group Meeting, Volume II - Session on Boundary Layer Stability. Air Force Report No. BSD-TR-67-213, vol. II, 1967.
72. McCauley William D., ed.: Boundary Layer Transition Study Group Meeting, Volume IV - Session on Boundary Layer Transition Control and Panel Session. Air Force Report No. BSD-TR-67-213, vol. IV, 1967.
73. Schubauer, G. B.; and Klebanoff, P. S.: Contribution on the Mechanics of Boundary-Layer Transition. NACA Tech. Rept. No. 1289, 1956.
74. Charters A.: Transition Between Laminar and Turbulent Flow by Transverse Contamination. NACA TN 891, 1943.
75. Dhwan, S.; and Narasimha, R.: Some Properties of Boundary Layer Flow During the Transition from Laminar to Turbulent Motion. J. of Fluid Mech. 3, 418, 1958.
76. Corrsin, S.; and Kistler, A. L.: Free Stream Boundaries of Turbulent Flow. NASA TR R-1244 (supersedes NACA TN 3133, 1954).
77. Fiedler, H.: Intermittency Distributions In Turbulent Wall Boundary Layers With And Without Pressure Gradients. NASA TT F-11, 326, 1967.
78. Cebeci, Tuncer; Smith, A. M. O.; and Mosinkis, G.: Calculation of Compressible Adiabatic Turbulent Boundary Layers. AIAA Paper No. 69-687, presented at the AIAA Fluid and Plasma Dynamics Conference, San Francisco, California, June 16-18, 1969.
79. Ames Research Staff: Equations, Tables, and Charts for Compressible Flow. NACA Rept. 1135, 1953.
80. Lomax, Harvard; and Inouye, Mamoru: Numerical Analysis of Flow Properties About Blunt Bodies Moving at Supersonic Speeds In An Equilibrium Gas. NASA TR R-204, 1964.
81. Smith, A. M. O.; and Clutter, D. W.: Solution of the Incompressible Laminar Boundary-Layer Equations. AIAA Journal, vol. 1, no. 9, Sept. 1963.

82. Smith, A. M. O.; and Clutter, D. W.: Solution of Prandtl's Boundary Layer Equations. Douglas Aircraft Company Engineering Paper 1530, 1963.
83. Richtmyer, R. D.: Difference Methods for Initial-Value Problems. Interscience Publishers, Inc. New York, 1957.
84. Hilderbrand, F. B.: Introduction to Numerical Analysis. McGraw-Hill Book Company, Inc., 1956.
85. Scarborough, James B.: Numerical Mathematical Analysis. The Johns Hopkins Press, Baltimore, 1962.
86. Beckwith, Ivan E.; and Bushnell, Dennis M.: Detailed Description and Results of a Method for Computing Mean and Fluctuating Quantities in Turbulent Boundary Layers. NASA TN D-4815, 1968.
87. Flügge-Lotz, I.; and Baxter, D. C.: The Solution of Compressible Laminar Boundary Layer Problems by a Finite Difference Method. Tech. Rept. No. 103, Div. of Eng. Mech., Stanford Univ., Stanford, Calif., 1956.
88. Baxter, D. C.; and Flügge-Lotz, I.: The Solution of Compressible Laminar Boundary Layer Problems by a Finite Difference Method, Part II. Further Discussion of the Method and Computation of Examples. Tech. Rept. No. 110, Division of Eng. Mech., Stanford Univ., Stanford, Calif., 1957.
89. Flügge-Lotz, I.; and Yu, E. Y.: Development of a Finite-Difference Method for Computing a Compressible Laminar Boundary Layer With Interaction. Division of Engr. Mech., Stanford Univ., Stanford, Calif., Rept. No. 127, 1960.
90. Wu, J. C.: The Solutions of Laminar Boundary Layer Equations by the Finite-Difference Method. Douglas Aircraft Co., Inc. Report No. SM-37484, 1960.
91. Raetz, G. S.: A Method of Calculating Three-Dimensional Laminar Boundary Layers of Steady Compressible Flows. Northrop Aircraft, Inc., Rept. No. NAI-58-73, 1957.
92. Spalding, D. B.; and Chi, S. W.: The Drag of a Compressible Turbulent Boundary Layer on a Smooth Flat Plate With and Without Heat Transfer. J. Fluid Mech., vol. 18, pt. 1, Jan. 1964, pp. 117-143.

93. Harris, Julius E.: Force-Coefficient and Moment-Coefficient Correlations and Air-Helium Simulation for Spherically Blunted Cones. NASA TN D-2184, 1964.
94. Love, E. S.; Woods, W. C.; Rainey, R. W.; and Ashby, G. C., Jr.: Some Topics In Hypersonic Body Shaping. AIAA Paper No. 69-181, presented at the AIAA Seventh Aerospace Sciences Meeting, New York, New York, Jan. 20-22, 1969.
95. Moore, D. R.; and Harkness, J.: Experimental Investigation of the Compressible Turbulent Boundary Layer at Very High Reynolds Numbers. Ling-Temco-Vaught Research Center Rept. O-7100/4R-9, April 1964.
96. Coles, Donald: Measurements in the Boundary Layer on a Smooth Flat Plate in Supersonic Flow. III. Measurements in a Flat-Plate Boundary Layer at the Jet Propulsion Laboratory. JPL Report No. 20-71, June 1953.
97. Pletcher, Richard H.: On a Solution for Turbulent Boundary Layer Flows With Heat Transfer, Pressure Gradients, and Wall Blowing or Suction. Paper ERI-54100, Project 636, submitted to the Fourth International Heat Transfer Conference, November 1969.
98. Pletcher, R. H.: On a Finite-Difference Solution for the Constant Property Turbulent Boundary Layer. AIAA Journal, vol. 7, no. 2, 1969, pp. 305-311.
99. DuFort, E. C.; and Frankel, S. P.: Stability Conditions in the Numerical Treatment of Parabolic Differential Equations. Math Tables Aids Comput, vol. 7, 1953, pp. 135-152.
100. Marvin, Joseph G.; and Akin, Clifford M.: Combined Effects of Mass Addition and Nose Bluntness of Boundary-Layer Transition. AIAA Paper No. 69-706, presented at the AIAA Fluid and Plasma Dynamics Conference, San Francisco, California, June 16-18, 1969.
101. Marvin, Joseph G.; and Sheaffer, Yvonne S.: A Method for Solving the Nonsimilar Laminar Boundary Layer Equations Including Foreign Gas Injection. NASA TN D-5516, 1969.
102. Clutter, Darwin W.; and Smith, A. M. O.: Solution of the General Boundary Layer Equations for Compressible Laminar Flow, Including Transverse Curvature. Douglas Aircraft Co. Rep. L. B. 31088, Feb. 15, 1963.

103. Winter, K. G.; Rotta, J. C.; and Smith, K. G.: Untersuchungen der turbulenten Grenzschicht an einetaillierten Drehkörper bei Unter- und Überschallströmung. Aerodynamische Versuchsanstalt Göttingen, DLR FR 65-52, November 1965.
104. Herring, James H.; and Mellor, George L.: A Method of Calculating Compressible Turbulent Boundary Layers. NASA CR-1144, 1968.
105. Sims, Joseph L.: Tables for Supersonic Flow Around Right Circular Cones at Zero Angle of Attack. NASA SP-3004, 1964.
106. McLafferty, George H.; and Barber, Robert E.: Turbulent Boundary Layer Characteristics in Supersonic Streams Having Adverse Pressure Gradients. Rep. R-1285-11 (Contract No. N0a(5)55-133-C), Res. Dept. United Aircraft Corp., Sept. 1959.
107. Bradshaw, P.: The Analogy Between Streamline Curvature and Buoyancy in Turbulent Shear Flow. J. Fluid Mech., vol. 36, part 1, March 1969, pp. 177-191.
108. O'Donnell, Robert M.: Experimental Investigation at a Mach Number of 2.41 of Average Skin-Friction Coefficients and Velocity Profiles for Laminar and Turbulent Boundary Layers and an Assessment of Probe Effects. NACA TN 3122, 1954.
109. Johnson, Charles B.: Pressure and Flow-Field Study at Mach Number 8 of Flow Separation on a Flat Plate With Deflected Trailing-Edge Flaps. NASA TN D-4308, 1968.
110. Whitfield, Jack D.; and Iannuzzi, F. A.: Experiments on Roughness Effects on Boundary-Layer Transition up to Mach 16. AEDC TR 68-261, Jan. 1969.

XII. VITA

The author was born in [REDACTED], on [REDACTED]. He was graduated from York High School in Yorktown, Virginia, in 1956. He enrolled in 1956 as a freshman at the Virginia Polytechnic Institute under the Cooperative Engineering Program with the National Advisory Committee for Aeronautics at the Langley Research Center, Hampton, Virginia. He was awarded the 1961 Undergraduate National Minta Martin Award for a technical paper completed during his senior year at the Virginia Polytechnic Institute. In 1961 he received the degree of Bachelor of Science in Aerospace Engineering. He enrolled as a graduate student at the Virginia Polytechnic Institute in 1962 and received the degree of Master of Science in Aerospace Engineering in 1964.

The author has been continuously employed at the Langley Research Center, Hampton, Virginia, since his graduation from high school in 1956.

Julius E. Harris

XIII. APPENDIX

Equations (8.29) and (8.30) are the difference equations used to represent the partial differential equations for the conservation of momentum and energy, respectively. These equations are repeated for convenience as follows:

$$\begin{aligned} A1_n F_{m+1,n-1} + B1_n F_{m+1,n} + C1_n F_{m+1,n+1} + D1_n \Theta_{m+1,n-1} \\ + E1_n \Theta_{m+1,n} + F1_n \Theta_{m+1,n+1} = G1_n \end{aligned} \quad (A-1)$$

$$\begin{aligned} A2_n F_{m+1,n-1} + B2_n F_{m+1,n} + C2_n F_{m+1,n+1} + D2_n \Theta_{m+1,n-1} \\ + E2_n \Theta_{m+1,n} + F2_n \Theta_{m+1,n+1} = G2_n \end{aligned} \quad (A-2)$$

These equations are obtained from equations (7.39) and (7.40) and the difference quotients presented in Section 8.1.2. The coefficients $A1_n$, $B1_n$, etc., in equations (A-1) and (A-2) are functions of quantities evaluated at stations m and $m-1$ (see fig. 9) and are therefore known. These coefficients are as follows:

$$A1_n = Y_3 H_3 - Y_6 H_{11} \quad (A-3)$$

$$B1_n = X_1 H_1 - Y_2 H_3 - Y_5 H_{11} + H_5 \quad (A-4)$$

$$C1_n = Y_1 H_3 + Y_4 H_{11} \quad (A-5)$$

$$D1_n = -Y_6 H_4 F_Y \quad (A-6)$$

$$E1_n = \frac{Y_5}{Y_6} D1_n + H_6 \quad (A-7)$$

$$F1_n = -\frac{Y_4}{Y_6} D1_n \quad (A-8)$$

$$G1_n = H_1 F_{m2} + H_4 T_Y F_Y \quad (A-9)$$

$$A2_n = -2Y_6 H_8 F_Y \quad (A-10)$$

$$B2_n = \frac{Y_5}{Y_6} A2_n \quad (A-11)$$

$$C2_n = -\frac{Y_4}{Y_6} A2_n \quad (A-12)$$

$$D2_n = Y_3 H_{10} - Y_6 H_{12} \quad (A-13)$$

$$E2_n = X_1 H_1 - Y_2 H_{10} - Y_5 H_{12} \quad (A-14)$$

$$F2_n = Y_1 H_{10} + Y_4 H_{12} \quad (A-15)$$

and

$$G^2_n = H_1 T_{m2} + H_8 (F_Y)^2 + H_9 (T_Y)^2 \quad (A-16)$$

The coefficients $Y_1, Y_2, \dots, Y_6, X_1, \dots, X_5$, etc., are functions of the grid-point spacing and are defined in equations (8.15) to (8.20) and (8.7) to (8.11), respectively. The coefficients H_1, H_2 , etc., are defined as follows:

$$H_1 = \xi_{m+1} F_{ml} \frac{(FT)}{\Delta \xi_2} \quad (A-17)$$

$$H_2 = V_{ml} - L_{ml} (\bar{E}_{ml} C'_{ml} + \bar{E}'_{ml} C_{ml}) \quad (A-18)$$

$$H_3 = -\bar{E}_{ml} L_{ml} C_{ml} \quad (A-19)$$

$$H_4 = H_3 \frac{L'_{ml}}{L_{ml}} \quad (A-20)$$

$$H_5 = \beta_{m+1} F_{ml} \quad (A-21)$$

$$H_6 = -\beta_{m+1} \quad (A-22)$$

$$H_7 = V_{ml} - L_{ml} (\hat{E}_{ml} C'_{ml} + \hat{E}'_{ml} C_{ml}) \quad (A-23)$$

$$H_8 = -\alpha_{m+1} L_{ml} \bar{E}_{ml} C_{ml} \quad (A-24)$$

$$H_9 = -\hat{E}_{ml} L'_{ml} C_{ml} \quad (A-25)$$

$$H_{10} = H_9 \frac{L_{ml}}{L'_{ml}} \quad (A-26)$$

$$H_{11} = H_2 + H_4 T_Y \quad (A-27)$$

and

$$H_{12} = H_7 + 2H_9 T_Y \quad (A-28)$$

The undefined quantities appearing in equations (A-17) to (A-28) are defined as follows:

$$F_{ml} = X_4 F_{m,n} - X_5 F_{m-1,n} \quad (A-29)$$

$$T_{ml} = X_4 \Theta_{m,n} - X_5 \Theta_{m-1,n} \quad (A-30)$$

$$V_{ml} = X_4 V_{m,n} - X_5 V_{m-1,n} \quad (A-31)$$

$$F_{m2} = X_2 F_{m,n} - X_3 F_{m-1,n} \quad (A-32)$$

$$T_{m2} = X_2^{\ominus}{}_{m,n} - X_3^{\ominus}{}_{m-1,n} \quad (A-33)$$

$$L_{m1} = \sqrt{T_{m1}} \frac{1 + \left(\frac{S}{T_e}\right)_{m+1}}{T_{m1} + \left(\frac{S}{T_e}\right)_{m+1}} \quad (\text{Air only}) \quad (A-34)$$

$$L'_{m1} = \frac{L_{m1}}{2T_{m1}} \left[\frac{\left(\frac{S}{T_e}\right)_{m+1} - T_{m1}}{\left(\frac{S}{T_e}\right)_{m+1} + T_{m1}} \right] \quad (\text{Air only}) \quad (A-35)$$

$$\bar{E}_{m1} = (\bar{\epsilon}_{av})_{m+1,n} \quad (\text{See Section 8.1.7, eq. (8.37)}) \quad (A-36)$$

$$\hat{E}_{m1} = \frac{(\hat{\epsilon}_{av})_{m+1,n}}{\sigma} \quad (A-37)$$

$$\bar{E}_Y = Y_4 \bar{\epsilon}_{m,n+1} - Y_5 \bar{\epsilon}_{m,n} - Y_6 \bar{\epsilon}_{m,n-1} \quad (\text{See eq. (8.14)}) \quad (A-38)$$

$$\hat{E}_Y = Y_4 \hat{\epsilon}_{m,n+1} - Y_5 \hat{\epsilon}_{m,n} - Y_6 \hat{\epsilon}_{m,n-1} \quad (A-39)$$

$$F_Y = Y_4 F_{m,n+1} - Y_5 F_{m,n} - Y_6 F_{m,n-1} \quad (A-40)$$

$$T_Y = Y_4^{\ominus}{}_{m,n+1} - Y_5^{\ominus}{}_{m,n} - Y_6^{\ominus}{}_{m,n-1} \quad (A-41)$$

$$\beta_{m+1} = \left(\frac{2\xi}{u_e} \frac{du_e}{d\xi} \right)_{m+1} \quad (\text{See eqs. (7.41)}) \quad (\text{A-42})$$

and

$$\alpha_{m+1} = \left(\frac{u_e^2}{T_e} \right)_{m+1} \quad (\text{A-43})$$

The transverse curvature terms are contained in the quantities C_{ml} and C'_{ml} which appear explicitly in the H_2 , H_3 , H_7 , H_8 , and H_9 coefficients. The transverse curvature term in the transformed plane (see eq. (7.43)) may be written as follows:

$$t^{2j} = 1 + \frac{2\omega j(W) \sqrt{2\xi} \cos \phi}{\rho_e u_e} \int_0^\eta \Theta d\eta \quad (\text{A-44})$$

where t represents the ratio r/r_0 and is a known quantity for the $N-1$ grid points at station $m-1$ and m . Then, the extrapolated values at $m+1, n$ are obtained as follows where the parameter C is used to represent t^{2j} :

$$C_{ml} = X_4 C_{m,n} - X_5 C_{m-1,n} \quad (\text{A-45})$$

$$C'_{ml} = Y_4 C_{m,n+1} - Y_5 C_{m,n} - Y_6 C_{m,n-1} \quad (\text{A-46})$$

Two quantities (symbols) as of now remain undefined. These are FT and W which appear in equations (A-17) and (A-44), respectively. These are code symbols used in the digital program. The code symbol W

appearing in equation (A-44) is used to either retain or neglect the transverse curvature terms for axisymmetric flows; that is, $W = 1$ or 0 , respectively. For planar flows, the transverse curvature term does not appear since j equals 0 .

The code symbol FT (flow type) appearing in equation (A-17) is used to either retain or neglect the nonsimilar terms in the governing differential equations; that is, $FT = 1$ or 0 , respectively. If FT is assigned a value of unity, the solution to the nonsimilar equations (eqs. (7.38) to (7.40)) is obtained. If FT is assigned a value of zero, the locally similar solution is obtained; that is, the following system of equations are solved.

Continuity

$$\frac{\partial V}{\partial \eta} + F = 0 \quad (A-47)$$

Momentum

$$V \frac{\partial F}{\partial \eta} - \frac{\partial}{\partial \eta} \left(t^{2j} \frac{\partial F}{\partial \eta} \right) + \beta (F^2 - \Theta) = 0 \quad (A-48)$$

Energy

$$V \frac{\partial \Theta}{\partial \eta} - \frac{\partial}{\partial \eta} \left(t^{2j} \frac{\partial \Theta}{\partial \eta} \right) - \alpha t^{2j} \frac{\partial}{\partial \eta} \left(\frac{\partial F}{\partial \eta} \right)^2 = 0 \quad (A-49)$$

The governing equations for the locally similar system are obtained from equations (7.38) to (7.40) by neglecting derivatives of the dependent variables F , Θ , and V with respect to the streamwise

coordinate, ξ . The capability of obtaining locally similar solutions is desirable in that for a given test case the locally similar and complete nonsimilar solutions can be obtained for the identical program inputs and numerical procedures. Consequently, the effects of the nonsimilar terms on the boundary layer characteristics can be determined by direct comparison of the results.